Abstract

Generation of Pseudo-CT using Two Sets of MRI Scans for MRI-only Radiation Therapy

By

Samuel Chen Leu

July 2019

Dissertation Directors: Zi-Wei Lin and Zhibin Huang

With increasing interests in magnetic resonance imaging (MRI)-only radiation therapy (RT) and the emergence of MRI system integrated with the linear accelerator, a method substituting the computed tomography (CT) in radiation therapy is required. The method to substitute the CT is by generating a pseudo-CT (pCT). A CT is necessary to provide the electron density information and to calculate the simulated dose distribution in treatment plans.

In this thesis, a voxel-based method is developed to generate the pCT image using two sets of MRI data. The method is trained with the CT data and two different sets of MRI data of multiple patients, where the anatomical structures in the images are segmented into several regions. A regression analysis is used to determine the two-variable polynomial function for each region to relate a voxel's two MRI intensity values to its CT number. This method is validated by applying a leave-one-out-cross-validation (LOOCV) and the accuracy of the pCT is evaluated by determining the mean absolute error (MAE) comparing the pseudo-CT to the reference-CT.

The average MAE across all patients is 40.3 $\pm$ 3.0 Hounsfield Unit (HU). Our proposed method shows promising results in using a multi-variable polynomial prediction model to predict CT numbers from MRI images. The generated pCT images closely match the reference-CT image and the MAE results are comparable to other studies using more complicated methods.

Generation of Pseudo-CT using Two Sets of MRI Scans for MRI-only Radiation Therapy

A Dissertation Presented to the Faculty of the Department of Physics

In Partial Fullfillment of the Requirements for the Degree of

Ph.D. in Biomedical Physics

by

Samuel C. Leu

July 2019

Generation of Pseudo-CT using Two Sets of MRI Scans for MRI-only Radiation Therapy

by

Samuel Chen Leu

APPROVED BY:

DIRECTOR OF
DISSERTATION: _____

Zi-Wei Lin, PhD

DIRECTOR OF
DISSERTATION: _____

Zhibin Huang, PhD

COMMITTEE MEMBER: _____

Yuanming Feng, PhD

COMMITTEE MEMBER: _____

Michael Dingfelder, PhD

COMMITTEE MEMBER: _____

Jefferson Shinpaugh, PhD

CHAIR OF THE DEPARTMENT
OF (Physics): _____

Jefferson Shinpaugh, PhD

DEAN OF THE
GRADUATE SCHOOL: _____

Paul J. Gemperline, PhD

ACKNOWLEDGEMENTS

I would like to thank my family for their continued support and encouragement throughout my academic career.

I would like to thank my advisor, Dr. Zi-Wei Lin, (July 2016 - present) for stepping up and guiding me in the right directions, for being patient with me and working hard to help me understand the equations, concepts, and ideas that led to this work.

I would also like to thank my other dissertation advisor Dr. Zhibin Huang (August 2014 - June 2016) for initiating this work and providing the data necessary for this work.

Additionally, I would like to thank my committee members Dr. Yuanming Feng, Dr. Michael Dingfelder, and Dr. Jefferson Shinpaugh for their help and input on this Dissertation.

Finally, I would like to thank the staff and faculty of the East Carolina University Department of Physics for their help and the use of their facilities.

Contents

List of Tables

List of Figures

List of Abbreviations

2D Two-Dimensional

3D Three-Dimensional

^{60}Co Cobalt-60

CT Computed Tomography

HU Hounsfield unit

IGRT Image-Guided Radiation Therapy

LOOCV Leave-one-out-cross-validation

MAE Mean Absolute Error

MR Magnetic Resonance

MR_1 MR images acquired from T1 Flash

MR_2 MR images acquired from T2 TSER

MRI Magnetic Resonance Imaging

MR-Linac Magnetic Resonance System integrated with Linear Accelerator

Nbin number of MR intensity bins

pCT pseudo - Computed Tomography

PDF Probability Density Functions

PET Positron Emission Tomography

PTV Planned Target Volume

rCT reference - Computed Tomography

RMS Root-Mean-Squared

ROI Region of Interest

RT Radiation Therapy

SD Standard Deviation

T1 Spin-lattice process

T2 Spin-spin process

TPS Treatment Planning System

1 Introduction

With a growing interest in magnetic resonance imaging (MRI)-only radiotherapy therapy (RT) and the emergence of magnetic resonance system integrated with a linear accelerator (MR-Linac), a substitute for determining the attenuation coefficient data is necessary for accurate dose calculations.

The typical workflow in today's radiation therapy clinic is to use computed tomography (CT) to simulate the radiation treatment, to acquire images for creating treatment plans, and to position the patient at treatment. Other imaging modalities, like MR, are used as a support to improve accuracy and delineation in radiation treatment planning. Use of multiple modalities necessitates an additional step in acquiring and registering the images between the modalities: CT and MRI. This step introduces a systematic registration error. Thus, it would be beneficial to eliminate this step and use MRI-only RT.

In theory, a MRI-only RT has the benefit of improving workflow and completely removing the systematic registration errors introduced when registering images between MRI and CT data [1, 2], since no image registration will be necessary. MRI-only RT will also benefit from the precise treatment target delineation due to MRI's superior soft tissue contrast [3], which can be obtained without any additional radiation dose to the patient.

However, a MRI-only RT workflow has a problem in creating treatment plans with the magnetic resonance (MR) images due to a lack of attenuation coefficient data. Attenuation coefficient data can provide electron density information from the interaction of biological tissue with ionizing radiation. The electron density information is critical for calculating a simulated dose distribution within the irradiated volume. The MR images are acquired by the nuclear magnetic resonance property of biological tissues,

a different physical phenomenon from attenuation coefficient. A relation between MR signal intensity and the attenuation correction data needs to be established, which is difficult because MRI signal is not directly related to these coefficients.

Previous methods to address this problem and generate CT images called pseudo-CT (pCT) use either an atlas-based [4] or voxel-based method [5]. Pseudo-CT images are generated because of the direct relation between CT number or Hounsfield unit (HU) scale to electron density. In this thesis project, a voxel-based method is investigated that uses two set of MRI scans acquired using different MRI sequence parameters to create the pCT images. This method is evaluated with leave-one-out-cross-validation (LOOCV) applied to a sample of six patients comparing the generated target pCT and the reference-CT (rCT). Our method is also validated by comparing the dose distributions between the RT plans created on the pCT and the rCT images.

1.1 Radiotherapy

Radiation therapy or radiotherapy (RT) is a treatment method using ionizing radiation to control or kill disease cells, usually cancer. Radiation therapy may be curative or used as part of adjuvant therapy to prevent tumor recurrence after surgery removing malignant tumor.

Radiotherapy is applied to cancer treatment due to the effect of ionizing radiation to damage the DNA of cancerous tissue leading to cellular death. To spare normal tissues, the radiation beams are shaped to the contour of tumor and multiple beams are aimed from different angles to reduce dose to surrounding tissues, which is within the radiation path to the tumor. Delivery of dose can be fractionated into several occasions. The fractionations allow the tumor and healthy tissue to recover between occasions. The healthy tissue will recover to a greater extent between fractions, while the tumor will

accumulate more damage and eventually lead to cellular death.

In order to deliver the dose to a target accurately, typically medical imaging is used to form a simulation of the patient to aide in designing treatment plans. Furthermore, the simulation of the patient requires information about the radiation interaction properties of the tissues that the beam passes through to determine absorbed dose. This information is given by electron density or CT number that can be obtained by a CT scan [6].

The highest probability of cure with the least morbidity could be achieved in theory by increasing the radiation to encompass all cancer cells with sufficient dose while simultaneously sparing surrounding normal tissues [7]. Advances in image modalities and computers can accomplish this with modern treatment planning system (TPS) providing tools for multimodality image co-registration or fusion. The CT is often the primary imaging modality used for treatment planning and to determine dose distribution within the body contour. CT images are also used for diagnosis, target definition, and patient positioning before irradiation. The MRI is a secondary imaging modality for soft tissue contouring. Another imaging modality, positron emission tomography (PET), is used less often and usually where it can enhance the planning target volume delineation.

Improvements in imaging techniques and technologies combined with RT have lead to the idea of image-guided RT. Image-guided RT (IGRT) is a process where during a course of radiation treatment, two or three-dimensional imaging is used to direct RT by utilizing the imaging coordinates of the actual radiation treatment plan. Imaging technologies used include computed tomography, magnetic resonance imaging, optical tracking, ultrasound, and electromagnetic transponders. The goal of the IGRT is to improve the accuracy of the radiation field placement and reduce the exposure of healthy tissue during radiation treatments, thus it requires a more frequent monitoring and adapting to changes that may occur during the course of radiation treatment.

1.2 Electron Density in Radiotherapy

Radiotherapy relies on electron density information that is acquired through experimental data or measurements from helical keV x-ray scan with a CT machine. The electron density used in treatment planning is related to MeV photon attenuation used in radiotherapy. Equation (1) approximates the dose to electron density relationship

$$\begin{aligned} D &\overset{\text{CPE}}{\approx} K_{col} = \Psi * (\frac{\mu_{en}}{\rho}) \\ \frac{\mu_{en}}{\rho} &\overset{\text{MV}}{\approx} \frac{Z}{A} * \frac{N_A}{M_C} * \sigma_{inc} = \rho_e * \sigma_{inc} \\ D &\propto \rho_e \ , \end{aligned} \tag{1}$$

where D is dose, CPE is charged particle equilibrium, K_{col} is the collision kerma, Ψ is the photon energy fluence, $\frac{\mu_{en}}{\rho}$ is the mass energy-absorption coefficient averaged over the photon energy-fluence spectrum, Z is the atomic number, A is the atomic mass number, N_A is Avogadros constant, σ_{inc} is Compton scattering cross section, and ρ_e is electron density.

MeV photons interact with matter mainly via incoherent Compton scattering. The collision kerma, K_{col}, is the photon energy per unit mass that gets converted into electron in the region of interest as dose, D. The dose can be approximated as collision kerma under the assumption that the volume is in charged-particle equilibrium, meaning for every particle entering the volume an identical particle of the same energy leave the volume, thus the dose is proportional to electron density.

The CT machine usually operates in the 30 to 130 keV range of electromagnetic spectrum, where interaction is by Compton scattering, photoelectric effect, and Rayleigh scattering. The CT number is proportional to the scattering attenuation coefficient, $\hat{\mu}_s$, which is directly proportional to the electron density per volume, ρ_e^V. The scattering

attenuation coefficient of kV photons, $\hat{\mu}$, is related to ρ_e by equation (2) as a function of atomic number, Z,

$$\begin{aligned} \hat{\mu} &\overset{\text{kV}}{\propto} \rho_e^V * [\sigma_{coh} + \tau + \sigma_{inc}] \\ &= \rho_e^V * f(Z) = \rho * \rho_e * f(Z) \end{aligned} \tag{2}$$

where $\hat{\mu}_s$ is the scattering attenuation coefficient, ρ_e^V is the electron density per volume, σ_{coh} is the Rayleigh scattering cross section, τ is the photoelectric effect cross section, ρ is the mass density, and ρ_e is the electron density. The CT number is proportional to the scattering attenuation coefficient, which is related to electron density, ρ_{e}, by a function of atomic number, Z. [8].

1.3 Magnetic Resonance Imaging

Magnetic resonance imaging is a widely used non-ionizing radiation medical imaging technique for medical diagnosis, staging of disease, and follow-up. MRI scanner uses a strong magnetic field, magnetic field gradients and radio-frequency wave to form images by measuring the spatial distribution and magnetic properties of specific nuclear spins in the body. Hydrogen, having the largest magnetic moment and greatest abundance in the human body, is the element of choice for clinical utility. [9]

The major components of a clinical MRI scanner are the main magnet, gradient system, and the radio-frequency system. The main magnet creates a strong magnetic field around the imaged area, the magnetic moment of the protons align with the direction of the field. A radio-frequency pulse at the appropriate resonance frequency is applied exciting the spin orientation of protons from parallel to anti-parallel alignment to the external magnetic field. The excited protons emit electric signals when returning to its equilibrium state, which are measured by the radio-frequency system receiving coil. Spatial information for the signal is determined by varying the magnetic field through

the gradient system. Through Fourier transform computation, the received signals can be reconstructed into an image corresponding to the signal at a location within the body.

The protons in tissues after excitation return to its equilibrium state by independent relaxation processes of spin-lattice (T1) and spin-spin (T2), also known as the T1 and T2 relaxation time. The relaxation times are important tissue characteristics for imaging and affect the contrast of tissues in images. Utilizing differences in T1 and T2 relaxation time of tissues, different pulse sequences of repetition time, and spin echo time can be used to design and to create weighted images that demonstrate the different anatomical structures and thus create images with different tissue contrast properties [10]. The contrast in an image is proportional to the difference in signal intensity due to these parameters and can be expressed generally as

$$S(x,y) = k \cdot \rho(x,y) \cdot (1 - e^{\frac{-TR}{T1(x,y)}}) \cdot e^{\frac{-TE}{T2(x,y)}}, \tag{3}$$

where k is a scaling factor, $\rho(x,y)$ is the spin (proton) density, TR is the repetition time of the pulse sequence, TE is the spin echo time, T1(x,y) and T2(x,y) are relaxation time of the tissue at voxel position (x,y) within the body. The TR and TE are the basic pulse sequence parameters: repetition time is the length of time between two successive excitations (usually applications of the 90° radio-frequency pulse), and echo time represents the time between excitation pulse (radio-frequency pulse) and the peak of the measurement signal (echo) [11].

The general MR tissue signal can be characterized by the molecular sizes, molecular motions, and molecular interactions that have an impact on the T1 and T2 relaxation time: small molecules or aqueous materials exhibit long T1 and long T2; intermediate-sized molecules or proteinate materials have short T1 and short T2; and large slowly moving or bound molecules have long T1 and short T2 relaxation time. A T1-weighted

image can be created by allowing magnetization to recover before measuring MR signal by changing the repetition time, thus producing contrast chiefly based on the T1 characteristics of tissues, with de-emphasis of T2 and proton density contributions to signal. A T2-weighted image can be created by allowing magnetization to decay before measuring the MR signal by changing the echo time, thus producing images with high tissue contrast and emphasizing the T2 differences, however this is at the expense of less signal and greater image noise [9].

Furthermore, MRI produces several artifacts that needs to be taken into consideration: motion artifact, similar to other modalities, caused by voluntary, involuntary, and physiologic motions produce ghosts and blurring on MR images; flow artifact caused by motion of liquids within the human body, usually blood or cerebrospinal fluid; chemical shift artifact usually at the boundary between tissues high in fat and high in water, caused by slight inhomogeneities of main magnetic field; gibbs ring artifacts appear in MR images as alternating dark and bright lines; and nonuniform intensity artifact usually caused by sensitivity problems with use of surface coils [12].

1.4 Computed Tomography

Computed tomography is the most commonly used medical imaging technique usually referring to as X-ray CT. A computer processes the many combinations of X-ray measurements from different angles and positions to form scans that are projections of the imaged area. The scan data are used to determine transmission data and thus distribution of attenuation coefficient data within the imaged subject. A reconstruction of this data produces three-dimensional (3D) cross-sectional images of the imaged subject.

The main components of a conventional CT scanner is the X-ray generator (source) operating on a circular rotatable gantry with X-ray detectors on the opposite side of the

circle. Typically, the gantry rotates while the imaged subject on a couch is moved into the bore of the scanner. As X-ray photons pass through the imaged subject, the photons interact in three main ways: photon absorption, Compton scattering, and Rayleigh scattering. The X-ray detector on the opposite side of the circle records the attenuation of the X-ray beam by the imaged subject, also considered as the projection data of the subject.

The scanned data are processed using tomographic reconstruction methods that uses the projection data based on the angles and the positions of the CT source to determine a distribution of attenuation coefficient within the imaged space. The distributions of attenuation coefficient measurements is further normalized to a quantitative scale for describing radiodensity, the Hounsfield unit (HU) scale. The HU scale is a linear transformation of the attenuation coefficient into one in which distilled water at standard pressure and temperature is defined as 0 HU, while air at standard pressure and temperature is defined as -1000 HU. In a voxel, for the attenuation coefficient, μ, a corresponding HU value is give by:

$$HU = 1000 \times \frac{\mu - \mu_{water}}{\mu_{water} - \mu_{air}}, \tag{4}$$

where μ_{water} and μ_{air} are the linear attenuation coefficients of water and air, respectively. The HU scale within the human body with no foreign body (e.g. metallic objects) ranges from -1000 HU for air to +2000 HU for cortical bone.

The HU value or CT number has a close relation to attenuation coefficient used in treatment-planning system to convert to electron density by means of predefined relationship between the two quantities or by measurements of known tissue-equivalent phantoms. The electron density information is critical to calculation of dose distribution within the irradiated volume. Although CT provides the radiological characteristics of

tissue, the tissue heterogeneity correction data, and the electron density information, it is lacking in soft tissue delineation and its ionizing radiation carries a possible risk of radiation-induced cancer.

Furthermore, similar to other imaging modalities, CT has several artifacts that needs to be taken into consideration: motion artifact caused by voluntary, involuntary, and physiologic motions that produce blurring, shading, and streaking in the reconstructed image; dark 'streak' artifact behind high density objects (such as bone or metallic materials); and ring artifact by mis-calibrated or defective detector element.

1.5 Combined MRI - Radiotherapy System

The interest in using MRI in radiation therapy has lead to several designs by different groups to integrate a MRI system with a radiotherapy treatment system for simultaneous image acquisition and radiation treatment: a 0.25 T MR scanner combined with a ^{60}Co unit with a helical irradiation technique similar to the tomotherapy system [13], an accelerator mounted on a 0.2 T MR scanner with the MR scanner rotating along with the linac [14], a 0.35 T MR scanner integrated with a linear accelerator avoiding mutual disturbance by magnetic fields [15], and a 0.35 T MR scanner with three ^{60}Co head [16].

Lagendijk et al. [15] described designing a prototype magnetic resonance system integrated with a linear particle accelerator. The MR-Linac system is developed for online and real time MRI image guidance in radiotherapy. The designed prototype had a 1.5 T Phillips Achieva MRI scanner with a Magnex closed bore magnet surrounded by a single energy (6 MV) Elekta accelerator. The design had a magnetic shielding to create a zero magnetic field at location of the gun of the accelerator and a minimal magnetic field at the location of the accelerator tube. In a later related paper, Raaymakers et al. [17] presented a proof of concept with the constructed MR-Linac prototype. Initially, the

performance of the two systems was separately evaluated. The accelerator was evaluated with a GafChromic film, merely to show radiation can be delivered to the isocenter of the bore. The MRI was evaluated by acquiring a few standard imaging sequences for prostate, brain, and kidney with accelerator switched off. Last, a piece of pork chop was simultaneously irradiated and imaged using a T2 weighted sequence. The authors reported that the images with and without radiation beam were identical. The authors, Raaymakers et al. in a later paper [18], reported that the first patients treated with the MR-Linac for lumbar spine bone metastases. Pre-treatment CT was non-rigidly registered to the online MRI to obtain Hounsfield values. Dosimetric accuracy was assessed post-treatment from phantom measurements with ionization chamber and film. The author reported high accuracy with errors ranging from 0.0% - 1.7% in the isocenter.

The first commercially available integrated MRI system and radiotherapy system is the MRIdian developed by ViewRay (Oakwood Village, OH). The MRIdian system solved the problem of interaction between the MR scanner and radiation generator by substituting the linear acceleration with a ^{60}Co teletherapy head. Mutic et al. [16] provided an overview of the MR guided radiation therapy system. The system consisted of a split 0.35-T MR scanner with 3 ^{60}Co heads mounted on a ring gantry with independent multileaf collimators to provide simultaneous and continuous MR during RT delivery. Dose was calculated via Monte Carlo computation using a bulk density correction or deformation of electron density maps from a particular patient or a template one. Although the lower 0.35 T field strength of the MRI scanner had an affect on acquired images, the author reported that the lower field strength prevented magnetic susceptibility artifacts and allowed for continuous imaging without distorting the dose distributions. Furthermore, the author reported that the ^{60}Co head with multileaf collimators using a IMRT optimization mitigated the issue of ^{60}Co lower penetration and large penumbra radiation beam characteristic.

The design, construction, and commercial availability of integrated MR guided radiation therapy systems validate the development of Hounsfield unit (or CT) substitution model to provide accurate dose distribution.

1.6 Overview of CT Substitution

The development of CT substitute images, also known as pCT images, derived from MRI has applications in MRI-only RT workflow and in the field of positron emission tomography (PET).

The application of MRI takes advantage of the superb soft tissue contrast that varies by changing MR sequence parameters, probing physiological differences, and using different biochemical agent. This application has clinical potential in the field of molecular imaging due to complementary anatomic and biological information obtained from MRI and PET modalities [19]. A review of the potential competitive advantages of PET/MRI over a PET/CT system is provided by Jadvar et al. [20] stating that its unparalleled structural, metabolic, and functional information can impact diagnostic evaluation, clinical decision-making, patient management, and potential patient outcome for disease-specific, or organ-specific clinical situations. It may also enhance patient convenience by providing a "one-stop shop" for diagnostic imaging, which will reduce the patient anxiety, the total scan time, and the potential recall for repeated scanning.

In radiotherapy, the superior soft tissue contrast of MRI means an increasing role in contouring the gross tumor volume and organs at risk in radiotherapy treatment planning system (TPS) [21]. The benefits in improved delineation of the gross tumor volume and the organs at risk have the potential of allowing an increase in dose to the target volume, improving the coverage of the target volume, and sparing of the organs at risk [22, 23]. Furthermore, the potential of precise and increased dose to target while

sparing surrounding normal tissue has the benefit of improving local tumor control and minimizing normal tissue complications. In addition, the non-ionizing properties of MRI make it very suitable in IGRT for multiple imaging acquisitions.

The use of MRI for PET attenuation correction has a few primary considerations: the poor imaging of bone and lack of electron density information for dosimetric calculations, the presence of intrinsic system related and object induced image distortions, and a computer software that can accurately and reliably integrate and manipulate images with existing RT planning systems [24]. Over the last decade, the developments in computer software have addressed and mostly solved the issues in RT planning and the presence of intrinsic image distortions. The issue with the lack of electron density information and attenuation correction is addressed by the developments in generating pCT and the specific aim of this thesis.

The methods for CT substitute generation have been reviewed by Hofmann et al. [25], Bezrukov et al. [26], and Visvikis et al. [27] for PET/MR attenuation correction and by Nyholm et al. [28], Edmund et al. [29], and Wafa et al. [30] for MR-only radiotherapy workflow.

The generation of pCT can be grouped into three main categories: voxel based method, atlas based method, and hybrid method. The voxel based method can be further divided into segmentation and direct conversion methods utilizing the intensity value of voxels in images.

1.6.1 Atlas-Based Method

The atlas-based method essentially focuses on aligning pre-existing templates or an atlas derived from rCT images to target patient MR images through registration. The conversion attempts to match similar shape structures in MR images. The atlas contains pre-determined correlations to CT number that can be assigned to the patient's MRI

images and thus convert to pCT.

One of the earlier uses of the atlas-based method was for reconstruction of PET images. Montano et al. [31] created attenuation maps and emission templates by averaging transmission and PET scans for eleven patients. A nonlinear warping for anatomic standardization was used to match the images of the emission templates to the patient. The spatial transformation matrix was recorded and applied to the attenuation map template to generate a patient specific attenuation map. This method only used PET emission and transmission images, therefore no MRI or CT was involved. The images were compared to those obtained from measured attenuation correction serving as the gold standard for assessment. The author reported that the evaluation of images showed no significant differences between atlas-guided and measured transmission-based attenuation correction. However, quantitative differences were noted in several regions of the brain.

In a study on developing PET/MRI scanners for brain images, Hoffmann et al. [32] presented the approach of combining local pattern recognition and atlas registration method by using atlas registration as prior knowledge. The pattern recognition looks at patches of voxels to determine information from not only the intensity of one voxel but also the neighboring voxels and their corresponding CT values. This is a typical regression problem that is solved by using a gaussian process. The combined method described in this study first registered all atlas MR images to the patient MR image, and applied the same transformations to the corresponding atlas CT images. Then, the pattern recognition method was implemented on the transformed atlas images generating the pCT images. The pCT images were used for attenuation correction in reconstruction of the PET images. The average LOOCV mean absolute error (MAE) of the predicted pCT images was 100.7 HU. The author reported that the pCT reconstructed PET quantification had a mean error of 3.2% $\pm$ 2.5% and was not clinically significant. In a later

study on the whole body, Hoffmann et al. [33] compares the combined atlas pattern recognition method to a segmentation based method. The study concluded that the combined atlas pattern recognition method had better overall PET quantification accuracy with mean error of 14.1% ± 10.2% and 7.7% ± 8.4% for the segmentation method and the combined atlas pattern recognition methods, respectively.

Dowling et al. [34] used an atlas based method to map MR images to electron densities for dose calculation and digitally reconstructed radiograph for prostate patients. The atlas method used by this author is similar to method presented by Klein et al. [35], where the method is based on nonrigid registration of a set of pre-labeled atlas images and use of a probabilistic atlas approach. An average MR atlas was generated by multiple (five) iterations of nonrigid registration transformation matrix of all training subject with the new atlas generated used in a subsequent iteration. A probabilistic atlas for each organ of interest was generated by propagating manual segmentations for each training case. The same transformation matrix used was applied to corresponding CTs to generate a pCT average atlas. For a new patient, the MRI atlas was nonrigidly registered to the patient MRI and the same transformation applied to the to pCT atlas. In evaluating this method, the dose difference was found to be less than 2%. In a later study, Dowling et al. [4] using the same method reported that no significant difference was found between HU values for rectum, bladder, bone, and prostate of each patient's pCT and corresponding rCT.

Another atlas based method that was referred to as the patch-based approach was developed by Andreasen et al. [36] to create pCT of the brain. First, patches were extracted from the MR image of patient. A patch was defined as a cube with a side length of a given number of voxel centered on a spatial location in the patient MR image. A database of spatially close patches stored with their corresponding CT value was matched to the extracted patch through an intensity-based nearest neighbor search.

An affine alignment of each database MRI and the patient MRI was performed initially to constrain the search in the patch database. A structural similarity measure was used to discard highly dissimilar patches and each patch in the database was given a similarity weight. The eight most similar database patches and their CT values were used, with a final pCT value assigned based on the combined CT values and their similarity weight. The patch-based approach had an average MAE of 85 ± 14 HU and in term of dosimetric accuracy had an average deviation less than 0.5% in measures related to target coverage. In a later study, Andreasen et al. [37] applied the patch-based approach to the pelvis. The author reported that an average MAE of 54 HU, a mean deviation of less than 0.4% in relevant dose-volume histogram, and a gamma-index pass rate of 97% using a 1%/1mm criterion.

Additionally, other atlas-based methods [38–42] have been developed by other groups with similar methods described above for other anatomic areas. The advantages of atlas-based method are the fact that pre-existing template is produced from rCTs and less sensitive to low intensity value. A limitation to the atlas based method is that without pre-existing templates, such as tumors, operation scars, other anatomic area, or atypical anatomy, this method will be unable to extrapolate a possible pCT image.

1.6.2 Voxel-Based Method

The voxel-based method primarily uses information about the voxel intensities (contrast) in the MR images for conversion to a pCT image volume. Unlike the atlas-based method, none or limited information about the voxel locations is used. The voxel methods mainly utilize concepts of machine-learning to train (optimize) a model, to apply the model to MRI data, and to predict the CT number. The voxel based methods can be divided into bulk or continuous density assignment, threshold-base segmentation, and statistical regression [43].

Lee et al. [44] described a simple example of the voxel-based method commonly known as the bulk-density method to evaluate dosimetric differences between radiotherapy treatment plans created using MRI alone and using CT alone. First, all voxels in the body contour were assigned the CT number of water, 0 HU. Next, the bone was outlined manually and the average bone CT number from four patients, found to be 320 HU, was assigned to all voxels in the bone outlines. The assigned HU image for water and bone was the converted pCT image volume. Evaluation of the method was by creation of a conformal RT treatment plan on the pCT image and the comparison with the treatment plan created on the original CT image volume. For all treatment plans, all the planning target volume received between 93 and 107 percent of prescribed dose, which was considered to be acceptable.

Johansson et al. [45] used a Gaussian mixture regression model to establish a link between the voxel values in CT images to the voxel values in images from three MR sequences: one T2 weighted 3D spin echo based sequence and two dual echo ultrashort echo time MR sequences. A Gaussian mixture model for the intensity distribution of the images was created using expectation maximization. Besides the MR voxel intensity and the CT number, the model utilized mean value and standard deviation of the voxels in the 27 neighboring voxels around each target voxel. This model made the assumption that the images show a discrete number of tissues or clusters, where each cluster was characterized by a MR intensity value that corresponded to the tissue coordinates in a multidimensional intensity space. The intensity from a particular tissue fell in a distribution around the tissue type coordinate. The author evaluated this method through LOOCV procedure with the average MAE for the patients determined to be 137 HU with MAE varied from 117 - 176 HU for individual patients. The largest error reported in the study was from air-tissue and bone-tissue interfaces. In a later study, Johansson et al. [46] applied the Gaussian mixture regression model with spatial information to

generate a pCT for both attenuation correction of PET data and for dose calculations in an MR-only radiotherapy workflow. The author reported that the overall MAE for all patients was 130 ± 18 HU. Furthermore, the author concluded that with spatial information the model could possibly be used to create a general model for conversion applicable to the whole body.

Rank et al. [47] applied a voxel-wise tissue classification to derive pCT numbers from MR images. The MRI images were segmented into 128 classes representing tissues with different CT numbers using a high dimensional discriminant analysis based on a Gaussian mixture model framework. The MR images were acquired using different sequence parameters including 3D ultrashort echo time sequence (UTE), 2D turbo spin echo sequence with proton density, T2-weighting, and a 3D ultrafast gradient echo sequence. Additionally features, such as local intensity standard deviation and voxel coordinates, were used to augment information included in the high dimensional discriminant analysis model. The model was evaluated on three biological phantoms and the pCT images were compared to the matching real CT images. The MAE varied between 81 HU and 95 HU. The most significant deviations were observed at borders between air and different tissue classes. The method was further evaluated by using a stoichiometric Hounsfield look-up table to convert CT numbers to water equivalent path length values for ions and used in an ion radiotherapy treatment plan. Comparing the optimized treatment plans revealed that doses were 1.4 - 3.1% higher in the pCT based plans compared to real CT based plans. In a later study, Rank et el [48] evaluated the method in the brain region for three patients. The author reported that the MAE had a range of 141 - 165 HU. The soft tissue was in good agreement with rCT, with large deviations at air cavities and bones as well as different tissue types. The simulated ion treatment plans showed doses in planning target volume (PTV) to be 0.4 - 2.0% lower in comparison to rCT, whereas, photon treatment plans differed by no more than 0.2% in PTV.

Hsu et al. [49] used a probabilistic tissue classification to segment MR images into bone, fat, fluid, white matter, grey matter, and air. The following MR images were used in the study: T1-weighted, T2-weighted, two echoes from ultra-short echo sequence, and a calculated fat and water image using a Dixon method for the head and neck region. The classification was achieved via fuzzy c-means clustering with a spatial constraint. The fuzzy c-means algorithm assigned an attenuation properties with weights based on the probability of individual tissue class presented in the voxel. The pCT image volume is generated by multiplying the probability of each voxel represented in each class by the attenuation value of the class and summing the result of all classes. An analysis of this study showed that one MRI image volume was not sufficient to separate tissue types, the T2-weighted images were more sensitive to bone density variation, and the short echo UTE image showed improvement in contrasting air versus bone.

Korhonen et al. [50] constructed pCT by using a dual model HU conversion technique. The images were segmented into bone and soft tissues. A second-order polynomial model is applied to the MRI voxel intensity values within the bone tissue segment to convert to HUs. This model was further tuned for each patient by two patient-specific adjustments: MR signal normalization and an application cutoff for low density bony tissue. A threshold-based segmentation model was used with no patient-specific adjustments for converting soft tissue (such as fat and muscle) to HUs. The range of MR intensity values was divided into segments to represent signals for urine, muscle, and fat. The author reported that the average HU differences between constructed pCT and rCT ranged from -2 to 5 HU and from 22 to 78 HU in soft and bony tissues, respectively. The average local absolute value differences were reported to be 11 HU in soft tissues and 99 HU in bones.

Kim et al. [51] developed a voxel-based weighted summation approach to generate synthetic CT (or pCT) images. Three sequence parameters were acquired: 3D T1

weighted fast field echo sequence, 3D T2-weighted turbo spin echo sequence, and a 3D balanced turbo field echo sequence. Inverse intensity images were derived from the acquired images to have high-intensity values in the bone region. Image voxels were sorted into 5 classifications: air, bone, fat, soft tissue, and fluid. Bone classification was determined using manually drawn contours, and very low intensity voxels not within bone contours were classified as air. A truth table was constructed based on voxel intensity levels in the acquired MR images to determine what classification to assign to the remaining voxels. Only air voxels were assigned a bulk value, all other voxel synthetic CT values were calculated by using a weighted sum of the acquired and derived MR images. The weights were initialized with random values to determine a synthetic CT and optimized by minimizing the Euclidean distance of calculated voxel value differences between synthetic CT and real CT over 100 iterations. This was repeated for the optimization set of patient data with weights initialized with values from the previous set. The study reported that the average MAE for all patients comparing synthetic CT and real CT was 74.3 ± 10.9 HU with the greatest deviations seen around bone contour borders due to changes in position or contouring of the bone.

Han [52] described a method building on developments of deep learning and convolution neural networks in the computer vision literature. The deep convolutional neural network (DCNN) model had 27 convolution layers interleaved with pooling and unpooling layers and 35 million free parameters, which was trained to learn a direct mapping from MR images to their corresponding CTs. Training data consisted of eighteen brain tumor patients with both CT and T1-weighted MR images. The author reported that the DCNN model was trained by collecting all 2D MR slices with corresponding 2D CT slices. The author also reported that directly training a full-3D DCNN model was infeasible due to GPU memory limitations and the limited training data in the study. The 27 convolution layers were divided into two parts: the first 13 convolution layers

were the encoding part and the next 13 convolution layers were the decoding part. The encoding part extracted a classification of increasingly complex features from an input MR image. The decoding part transformed the features and gradually reconstructed the pCT prediction from low to high resolution. The final layer produced an image with the same size as the input image. The DCNN method produced an overall average MAE of 84.8 $\pm$ 17.3 HU for all subjects. The author reported that although training a DCNN model was slow, the training only needed to be done once and the model applied to a target patient MR to generate a pCT image volume took only 9 seconds.

Additionally, other voxel based methods [53–57] have been developed by other groups utilizing similar methods as described above or new methods. The voxel method is based on the assumption that a relationship exists or can be formulated between a voxel's CT number and MRI intensity value, at least for voxels of the same tissue type.

The advantages of using a voxel-based method are its tolerance of patients with atypical anatomy. In theory, the voxel-based method is not restricted to the existing training database and can be applied to any body part and possibly the whole-body. The disadvantages of using a voxel-based method are the scan time needed, field of view, contrast to noise ratio, and wide spread of CT number for identical MRI intensity value.

1.6.3 Hybrid Method

In some other works, the approach to generating pCT is through combining elements of the voxel based and atlas based methods.

One such combined approach was proposed by Gudur et al. [58] to combine both intensity and geometric information into a unifying probabilistic Bayesian framework for electron density mapping. For a certain voxel, the Bayesian framework was used to derive the probability distribution function. The distribution function of the unknown electron density was on a continuous scale conditional on relevant information, such

as the MRI intensity and the voxel geometry in a reference anatomy. The conditional probability density functions (PDF), geometry PDF and intensity PDF, were computed from template MRI and template CT: the intensity PDF was computed from using the intensity map of the MRI intensity to the corresponding CT intensity; and the geometry PDF was computed from all voxels within a $6\times6\times6$ mm^3 volume around a given voxel with the corresponding deformed template CT with Gaussian function as its kernel density weighting function. The author assumed that there was statistical independence of the MRI intensity and the MRI geometry. The Bayesian theorem was applied to obtain the probability distribution function for the electron density value of a voxel by multiplying the two conditional probability distribution functions. The author reported a MAE of 126 ± 25 HU from comparing the pCT and rCT.

Siversson et al. [59] used the statistical decomposition algorithm integrated in a MriPlanner software (Spectronic Medical AB, Helsingborg, Sweden) to generate pCT for ten prostate cancer patients. The statistical decomposition algorithm estimated the most probable CT representation for a patient MRI based on templates in a database. The database consisted of 15 MRI and CT image pairs acquired from the same individuals and nonrigidly registered with the prostate, bladder, colon, bones, and subcutaneous fat structures delineated. The statistical decomposition algorithm operated by identifying and segmenting visual features of the patient MR images. Each template MR image was registered to patient MR images by a transformation matrix using a nonrigid-block-matching method. The transformation matrix was applied to the associated template segmentations and a weight was calculated for each. A nonlinear warping procedure deformed their segmented structures with the segments of the patient MRI. A linear deformation was applied to tissue within and between segmented structures. The deformation matrix was used to constrain the nonrigid registration algorithm to further align structures of each deformed template MRI to the patient MRI. The resulting deforma-

tion matrix was applied to the corresponding template CT, thereby generating a set of candidate pCTs corresponding to the patient MRI. The voxels of each candidate pCT had a weight calculated using a proprietary machine learning method that promoted the HU values of the candidate pCTs that most accurately resembled the patient MRI. A final pCT representing the patient MRI was determined by fusing all candidate weighted pCTs. The author reported that the MAE within the body contour was 36.5 ± 3.1 HU between pCT and registered-CT. The mean absorbed dose difference to target was 0.0% ± 0.2% between pCT and registered-CT with an average 99.9% gamma pass rate.

1.7 Specific Aims

The question in a clinical practice with MRI-only RT is how to generate an accurate CT substitute with MRI data. The most robust and less restrictive method in generating a pseudo-CT for any patient anatomy is the voxel-based method. Inspired by the voxel-based approach of Korhonen et al., a polynomial model is used in this project for the mapping of MRI intensity values into CT number. More specifically, in this study a two-variable polynomial model is used, where the two variables represent the MRI intensity values from each of two MRI scans acquired with different MR sequence parameters.

The objective of this study is to investigate and to develop a method of generating pseudo-CT from two sets of MRI scans. The specific aims of the project can be summarized as follows:

1. Investigate the use of a polynomial prediction model to generate pseudo-CT from two sets of MRI scans, which includes the optimization of the model parameters.

2. Evaluate the pCT accuracy by comparing the generated pCT with rCT.

3. Evaluate the pCT accuracy by quantifying the dose differences between pseudo-CT and reference-CT treatment plans relevant to radiation therapy

2 Materials and Method

This chapter describes our process to determine the prediction model for generating a pCT and utilizing the pCT in a treatment plan. Sections 2.1 and 2.2 describe the acquired patient data and necessary pre-processing. Next, sections 2.3 and 2.4 describe the extracted training data and the process to determine the prediction model utilized in this thesis. Section 2.5 describes how a target pCT is generated from the prediction model. Sections 2.6 and 2.7 describe the conversion of HU to electron density and the radiation treatment plan created for the comparison of pCT to rCT. Section 2.8 describes the software used in calculations and measurements. Finally, section 2.9 describes the verification metrics used in evaluating the target pCT.

2.1 Patient Data

This section describes the acquisition of the training data and the process of the initial data selection.

2.1.1 Data Acquisition

A total of 10 female patients' cervical scans are acquired for a prospective study with serial MRI scans and CT scans during radiation treatment on an IRB-approved imaging protocol. This study has no effect on the treatment for the patients.

Cervical images of MRI scans are acquired on a Siemens Magnetron Espree 1.5T scanner. The MRI scans consist of two cervical scans using the MR sequence protocols for T1 Flash (MR_1) and T2 TSER (MR_2). Whole body CT scans for patients are acquired on a Siemens Biograph CT scanner within a month of MRI acquisition. Each patient image dataset consists of MR_1, MR_2, and CT scans with 30+ images.

The MR sequence protocols, T1 Flash and T2 TSER, are used to acquire the T1-weighted and T2-weighted images with differing tissue contrast property.

2.1.2 Data Selection

A preliminary data selection of the 10 cervical scans is achieved through the information on transformation matrix from a rigid image registration of the MR_1, MR_2, and CT scans for the same patient. The image registration is performed using the Velocity AI's built-in Multi-Modality Registration function with the axial slices of MR_1 being specified as the reference. A rigid registration is accomplished through transformation matrix that has translational changes along the x-, y-, z-axis and rotational changes along the x-, y-, z-axis, with changes occurring in the following order x, y, and then z-axis.

	$MR_2 \Rightarrow MR_1$			$CT \Rightarrow MR_1$		
	Rotation Along (Degree)			Rotation Along (Degree)		
Data	X-Axis	Y-Axis	Z-Axis	X-Axis	Y-Axis	Z-Axis
ID01	-4.30	-0.07	0.00	0.43	-1.56	2.59
ID02	-42.30	-0.22	0.00	1.21	-0.71	2.81
ID03	-32.89	-0.06	1.68	3.65	-3.11	-0.66
ID04	-38.07	-0.28	0.46	1.98	-1.64	4.56
ID05	7.10	0.00	0.00	4.04	3.08	-0.74
ID06	-15.40	0.00	0.00	-1.87	1.43	-0.68
ID07	40.70	-0.00	-0.00	-0.22	0.65	2.01
ID08	40.51	-0.20	-0.23	7.19	-1.81	1.96
ID09	-38.41	-2.64	1.31	7.59	0.61	6.71
ID10	-42.50	0.00	0.00	2.65	-1.00	0.98

Table 1: MR_2 to MR_1 and CT to MR_1 transformation matrix rotation along the fixed axis x, y, or z for registration of MR_2 to MR_1 and CT to MR_1 image.

Table 1 shows the rotational transformation in the image registration. Each image within the scans is inspected for significant visible MR artifacts. After the rotational transformation images have voxels with 'missing' intensity data. The 'missing' intensity

values are interpolated from neighboring voxels values. A lower degree of rotational change from MR_2 to MR_1 and CT to MR_1 is preferred to reduce uncertainty from the interpolated data in aligning the MR_2 and CT images. Eight patients, ID01, ID03, ID04, ID05, ID06, ID07, ID08, ID09 with relatively lower rotational changes for MR_2 to MR_1 and CT to MR_1 are chosen.

Next, a second alignment between the MR_1 and corresponding CT scans is performed and anatomical areas outside the MR_1 scan are cropped out. For this second alignment of MR_1 and CT scans, a deformable image registration on the Velocity AI is selected. The deformable registration reduces differences that result from the large time gap between acquiring the MRI scans and the CT scans.

Finally six patients, ID01, ID03, ID04, ID05, ID07, and ID08 are selected. These data are considered to have 'good' quality images because they have a smaller amount of visible artifacts, alignment error after image registration, and rotational transformation. On the other hand, 'bad' quality images, ID06 and ID09, are ones with misalignment of the bony tissue between MRI and CT scan after the deformable image registration. The misalignment due to organs that exhibit significant daily motion, bladder and bowel, is not taken into consideration when evaluating the image quality for the selection of patient data.

2.2 Data Pre-Processing

This section describes the data pre-processing from which calculations and measurements are performed. The pre-processing steps are registration of images, normalization of the voxel intensity, segmentation of anatomical structures, and grouping the patient data into cycles for LOOCV.

2.2.1 Registration

The spatial information (i.e. voxel geometry) for a patient is usually not consistent between patients especially for different modalities and is dependent on the orientation, coordinate system of the scanner, and patient setup. Furthermore, the MR and the CT imaging modalities have different image resolutions and voxel sizes. Therefore, an image registration is used to align the images and to ensured a 1-to-1 correspondence between voxels of the two imaging modalities.

Deformable image registration of the MR_1, MR_2, and CT scans is performed on Velocity AI (Varian Medical Systems) with the MR_1 assigned as the reference. This ensures that anatomical structures are aligned and each voxel corresponds to the same anatomical structure between the three different scans. The final deformed images are checked to ensure that no significant distortions result from the registration. After registration, the MR_1, MR_2, and CT scans have the same image resolution: axial image dimension = 320×320 voxels and voxel size ≈ 0.81×0.81×5.0 mm^3. The binary masks or the body masks (body contour) to eliminate air voxels, patient couch, and non-tissue voxel elements are created to cover only the contours of the imaged subject to reduce the computational burden [45, 60].

2.2.2 Normalization

The MRI scans are acquired under different imaging conditions and therefore each scan has a different overall image contrast. This difference in contrast is not attributed to different tissue types, but to how the MRI images are reconstructed, specifically, how the MRI intensity values are assigned. The MR intensity distribution varies between patients due to the differences in the MRI scanner (e.g. the transmitter gains, receiver gains, and coil positions) and also due to the differences in tissue compositions in the

scan area.

The lack of standardization in assigning MRI voxel intensity values for the same MRI sequence parameter causes significant noise and correlation error in using the non-normalized voxel intensity values of different patients. Therefore normalization is required, specifically, between MRI scans acquired with the same MRI sequence parameter, e.g. MR_1 or MR_2.

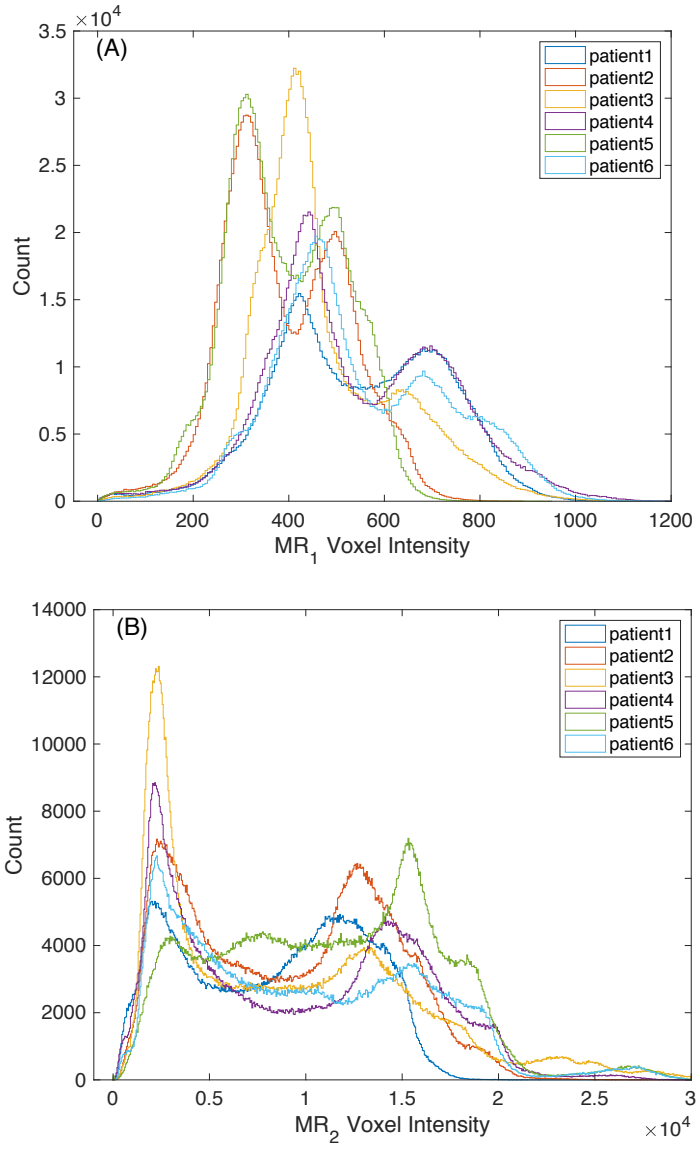

Figure 1: MR_1 (A) and MR_2 (B) histograms before normalization.

Figure 1 shows the histogram (MR intensity distribution) for MR_1 and MR_2 containing all voxel intensity values within the body contour. For each patient, the same cervical area is imaged; therefore, in theory although each image may vary between patients slice-to-slice, the overall tissues within the imaged area remain the same. Thus, the histograms should have similar counts to voxel intensity; more specifically, the overall histogram shapes (peak and range) should be similar between the patients. However, as observed in Fig. 1 this is not the case. Instead, it is observed that the peak to voxel intensity and the range of histogram vary for each patient. Therefore, the normalization of the training data is required.

The process to normalize the MRI voxel intensity is by first finding for each patient an average intensity value of all voxels within the body contour for the same imaged volume. Next, for the MR_1, a patient-specific correction factor is determined to multiply all the voxel intensity values, this ensures that the average intensity values for all MR_1 of each patient are consistent. Last, the same process is used for the MR_2 of each patient. After normalizing the MRI data, Fig. 2 shows that the peak to voxel intensity and the range of MR intensity distributions of different patients are now similar to each other.

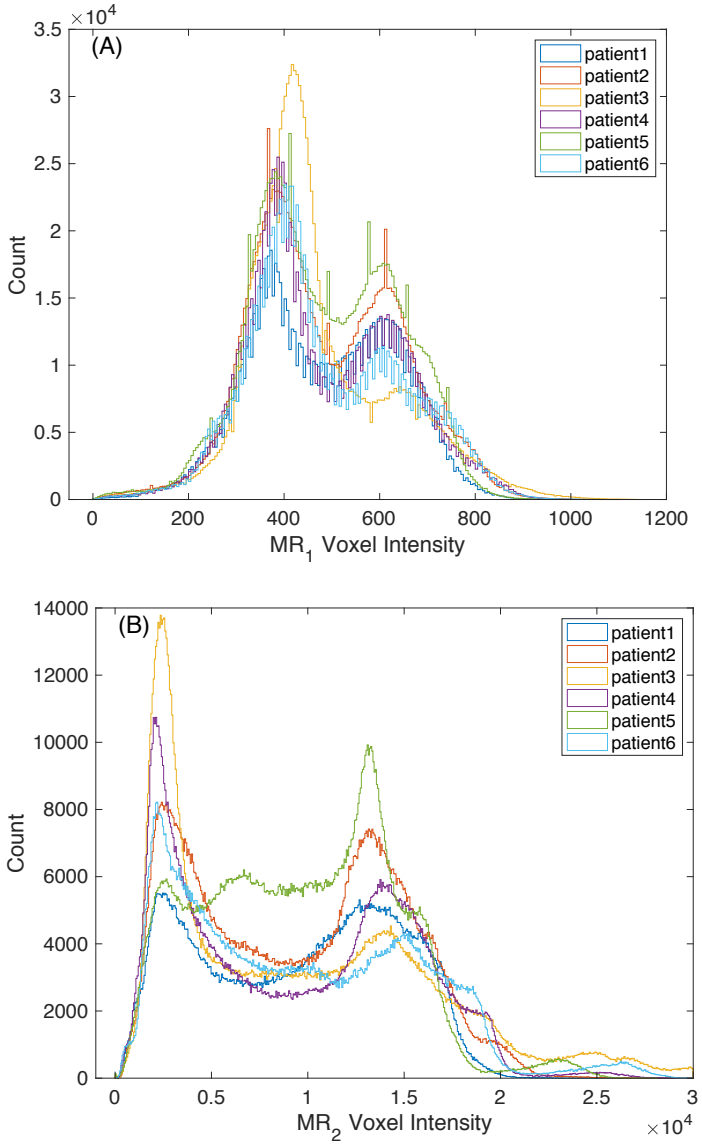

Figure 2: MR_1 (A) and MR_2 (B) histograms after normalization.

For the CT scans, the standard practice for medical-grade CT scanners is to calibrate the CT number with reference to water and air and normalize to the HU scale. Therefore, the process of normalizing described in this section is not performed on the CT data.

2.2.3 Segmentation

The anatomical structure of each patient is segmented with mask into three regions: bony, soft, and mixed regions. Figure 3 shows an example of the three regions superimposed on an MRI image.

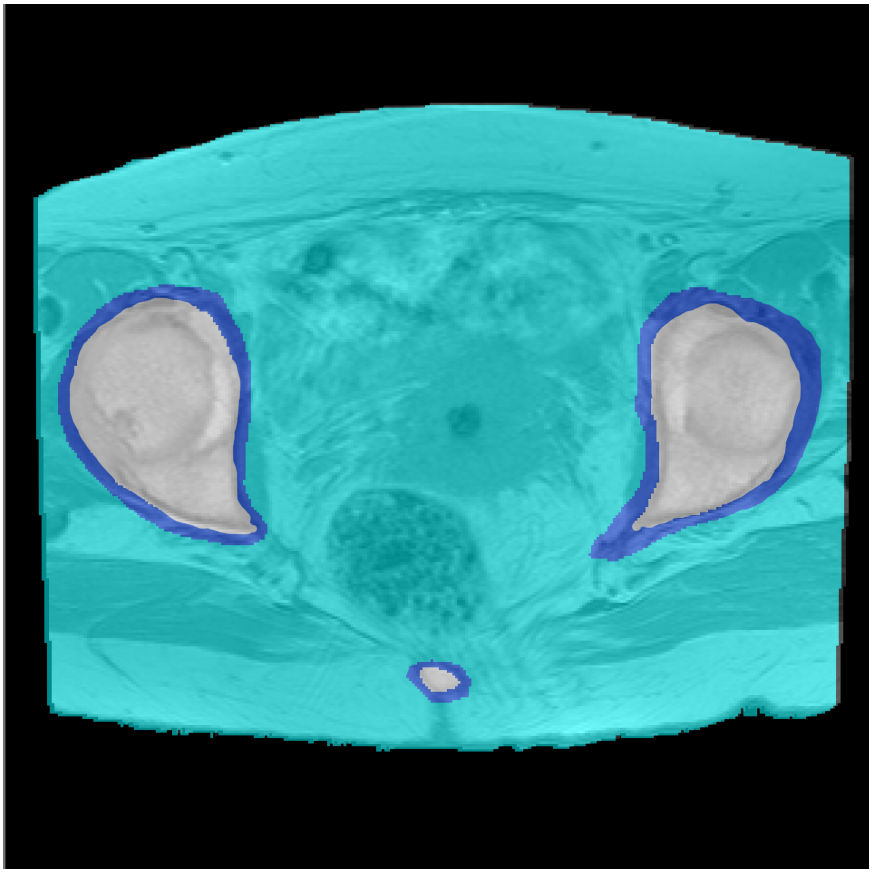

Figure 3: Segmentation of the three regions on an MRI image with the bony region (white), soft region (light blue), and mixed region (dark blue).

Using the 'roipoly' function of Matlab (Mathworks, Natick, MA, United States), the region of interest (ROI) is drawn manually on the anatomical structures of a sequence of fused CT and MR_1 image to define the segmentation masks. The bony region contains only the cortical and cancellous bone tissues; therefore the ROI masks are drawn within the clearly defined edge of the cortical bone with approximately 1 mm margin left out. As

seen from Fig. 3, this corresponds to the white area, where the entire femur head, pelvic bone, and spinal cord are located. The soft region contains all the soft tissue regardless of type. A ROI is drawn around any bony tissues with a margin of approximately $2-3$ mm. The area outside of this ROI and within the body contour are defined as the soft region, as seen from the light blue area in Fig. 3. The mixed region contains uncertain areas that mark the boundary of the bone and the soft tissue. This region also contains minor registration errors between MR and CT as well as volume averaging artifact that is cause by the high and low signal intensity tissues next to each other. The mixed region can be defined by either using the remaining area within the body contour not of bony or soft tissue or using the previously left out margin when defining the bony and soft region, as shown from the dark blue area in Fig. 3.

The red contour in Fig. 4 shows the excluded region that selects misaligned anatomical structures. The misalignments are due in large part to changes in organs with significant daily motion (i.e. cervix, bladder, and bowel) during the elapse time between MRI and CT acquisitions. The voxels within the excluded region are not used as training data to determine the mapping function or to evaluate the accuracy of the generated target pCT.

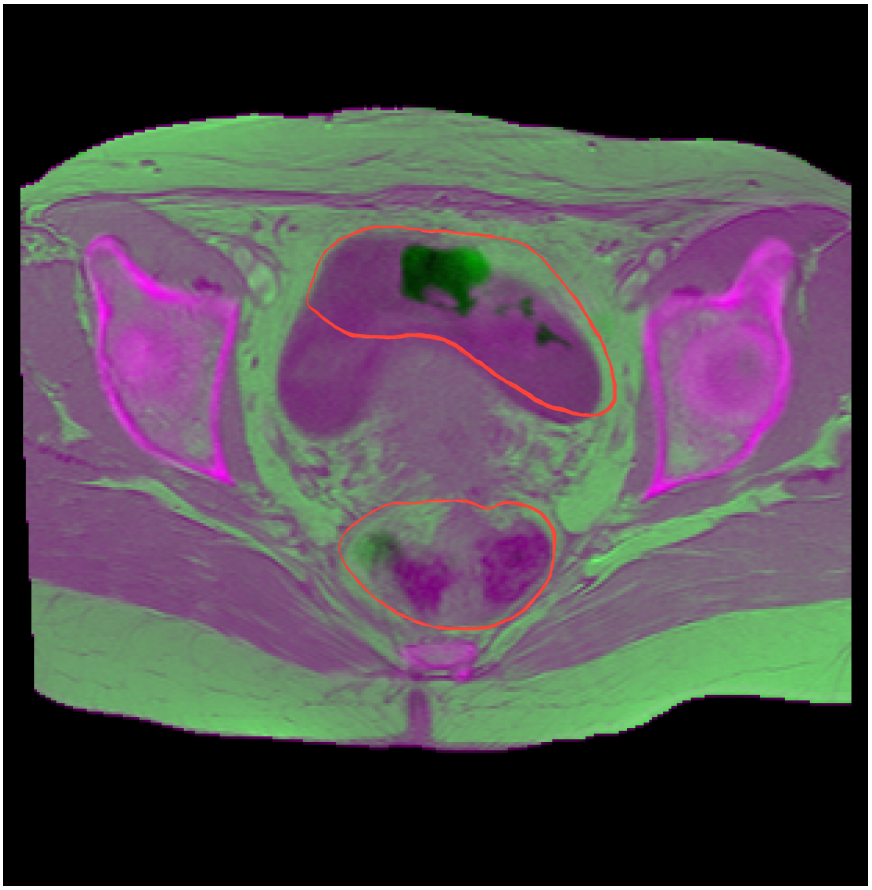

Figure 4: Example of a CT image (magenta) overlayed on the corresponding MRI image (green) with the excluded region shown inside the red contours.

2.2.4 LOOCV

To estimate how accurately a predictive model performs in practice, a leave-one-out cross-validation is applied on the patient data. The performance of the predictive model is trained on n - 1 sample of data, with n being the total number of patients. For cycle1, the data from patient2, patient3, patient4, patient5 and patient6 are designated as the training data to determine the predictive model. The predictive model is then applied to the remaining patient, patient1, as the target patient to generate a pCT image volume. This cycle is repeated with another patient left out as the target patient and

the remaining patients used to determine the predictive model. Table 2 presents the patients designated as the training data and the target patient. This process is similar to those described in studies by Hofmann et al. [33] and Johansson et al. [45].

	Cycle1	Cycle2	Cycle3	Cycle4	Cycle5	Cycle6
Training Data	Patient2	Patient1	Patient1	Patient1	Patient1	Patient1
	Patient3	Patient3	Patient2	Patient2	Patient2	Patient2
	Patient4	Patient4	Patient4	Patient3	Patient3	Patient3
	Patient5	Patient5	Patient5	Patient5	Patient4	Patient4
	Patient6	Patient6	Patient6	Patient6	Patient6	Patient5
Target	Patient1	Patient2	Patient3	Patient4	Patient5	Patient6

Table 2: List of training data and the target for each LOOCV cycle.

2.3 CT Number and MR Voxel Intensity

Once pre-processing is completed, the voxel intensity of MR_1, MR_2, and CT number for all patients in the training data is extracted and sorted into regions. Each voxel in the image is a data point and can be considered as a triplet datapoint. The triplet datapoint consists of the corresponding MR_1 intensity value, MR_2 intensity value, and CT number. Voxels of the same region (bony, soft, mixed) for each training patient are sorted together. The voxels from the excluded region are not included in the data to find or to evaluate our prediction model; this is to preserve the integrity of the true correlation between MR_1 intensity value, MR_2 intensity value, and the CT number. The triplet datapoints form the basis for modeling the relation between MR_1, MR_2 and CT.

As previously stated, the voxel method assumes that a correlation exists between a voxel's CT number and the matching voxel's MRI intensity value, at least for voxels of the same tissue type. However, this is not always the case and voxels with the same MRI intensity value, even of the same tissue type, may have a wide range of CT numbers. Therefore, our strategy is to have a second set of MRI images acquired with different

MRI sequences, so that the voxels with the same MRI intensity value (in the first set) but very different CT numbers may have different MRI intensity values in the second set, which will allow us to distinguish those voxels and map them to their corresponding CT numbers.

Furthermore, the MRI data of each region are separated into different MR_1 and MR_2 intensity value bins to reduce the computational burden and noise when determining the mapping function. An equal number of bins ($Nbin$) for MR_1 and MR_2 are used. The bin width is determined based on the normalized maximum MR_1 and MR_2 intensity values (1,420 and 37,100 respectively in this thesis). As a result, every voxel is associated with two bin indices, e.g., i for the MR_1 bin and j for the MR_2 bin, or (i, j). Inside a given (i, j) bin in these two dimensions, there can be multiple voxels with a range of CT numbers. The average CT number of the bin is defined as

$$\overline{CT}_{i,j} = \frac{1}{N_{i,j}} \sum_{k=1}^{N_{i,j}} CT_{i,j}^{k}, \tag{5}$$

where $N_{i,j}$ is the number of voxels within the i-th MR_1 bin and j-th MR_2 bin, and $CT_{i,j}^{k}$ denotes the CT number of the $k-$th voxel within this bin.

2.3.1 Bin Filling

Figure 5A shows the distribution of the average CT number ($\overline{CT}_{i,j}$) versus the MR bin indices (i, j) from the training data. The figure reveals that not all (i, j) bins are filled, i.e., have voxels from the training data, and thus have corresponding CT numbers.

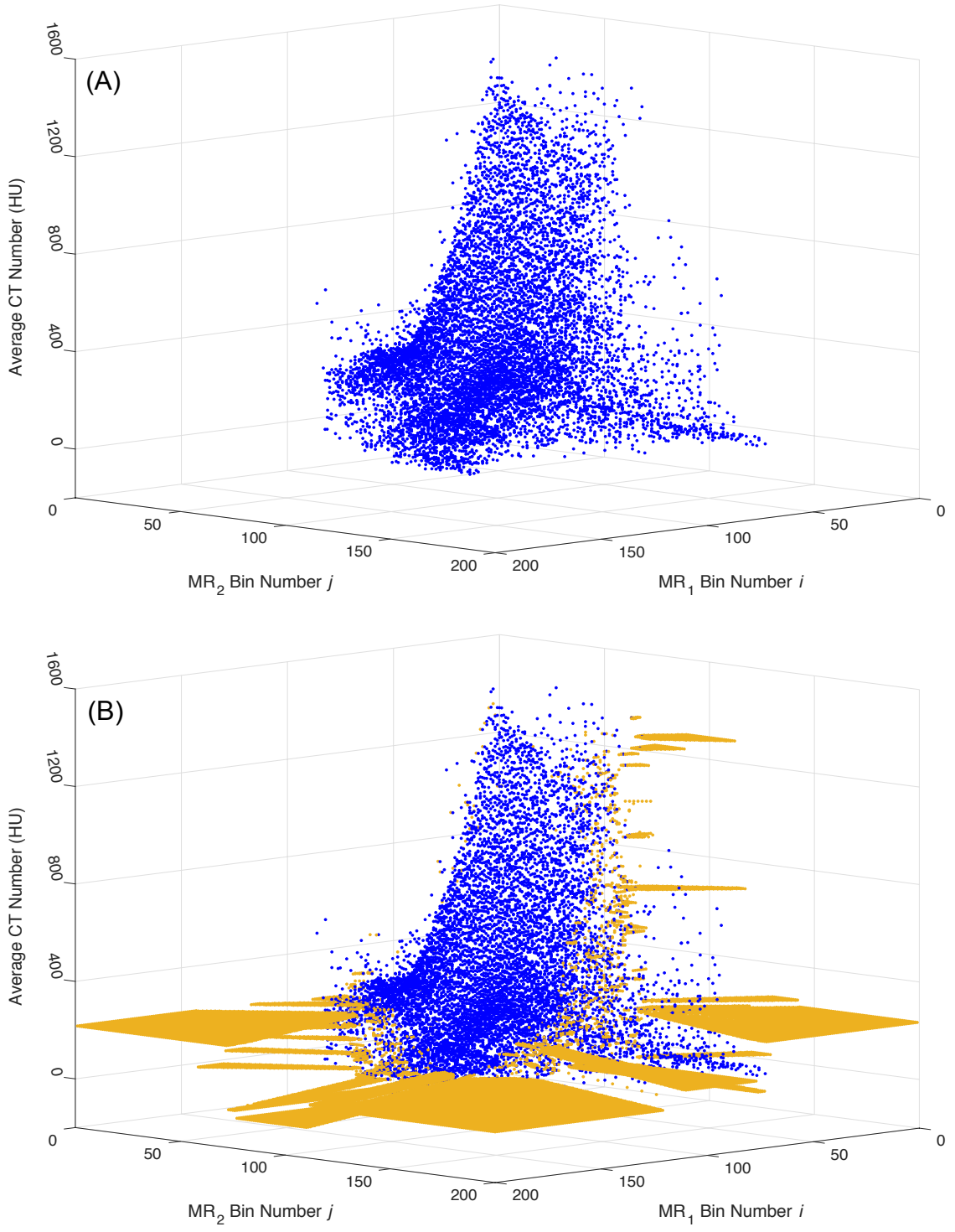

Figure 5: Distribution of the average CT number (HU), $\overline{CT}_{i,j}$, versus the MR_1 and MR_2 bin numbers from the training data for the bony region from Cycle1 without (A) and with (B) the filled empty bins (yellow) with $Nbin = 200$.

This causes the polynomial function to rapidly deteriorate in the MRI region with empty bins. Thus, to improve the stability of the prediction model, the empty (i, j) bins, i.e., the bins with no voxels, are filled with CT numbers, so that all the MRI (i, j) bins have corresponding CT numbers before determining the prediction model. An empty bin is assigned the HU value of the nearest filled bin. For example, for an empty bin with the MR_1 bin number i_e and MR_2 bin number j_e, its distance from a filled bin with the MR_1 bin number i and MR_2 bin number j is calculated as

$$d = \sqrt{(i - i_e)^2 + (j - j_e)^2}. \tag{6}$$

The average HU-value of the filled bin with the smallest distance d is then assigned to the empty bin. If the smallest distance corresponds to multiple filled bins, then the average HU-value of those multiple bins is assigned to the empty bin. Figure 5B shows the final distribution of $\overline{CT}_{i,j}$ as a function of the MR_1 bin numbers i and j from the training data after all empty bins are filled (yellow).

2.4 Prediction Models

This section describes the two general prediction models, the polynomial regression and bilinear interpolation method, developed in this thesis. The final optimal prediction model used is the polynomial regression method.

2.4.1 Polynomial Regression Method

A regression analysis mapping a voxel's two MRI intensities to its CT number on the Hounsfield unit scale for each region is determined. The prediction model is defined as a two-variable nth-degree polynomial function, which depends on a voxel's two MRI

intensity values to predict the voxel's expected CT number:

$$\begin{aligned} HU(S_1, S_2) &= \sum_{i_1,i_2=0}^{i_1+i_2 \le n} c_{i_1,i_2}\, S_1^{i_1}\, S_2^{i_2} \\ &= c_{0,0} + c_{1,0}S_1 + c_{0,1}S_2 + c_{1,1}S_1S_2 \ + \cdots + c_{n,0}\, S_1^n + c_{0,n}\, S_2^n, \end{aligned} \tag{7}$$

where n is the highest polynomial degree, $HU(S_1, S_2)$ is the dependent variable of the mapping function, S_1 is the intensity value from MR_1, S_2 is the intensity value from MR_2, S_1 and S_2 are both independent variables, and c_{i_1,i_2} is the fitting coefficient.

Using the 'NonlinearModelFit' Mathematica (Wolfram, Champaign, United States) function, a regression analysis is performed on the training data of each region to determine the coefficients c_{i_1,i_2} in equation (7), with the MR bin indices plus $-\frac{1}{2}$ as the independent variables and average CT number as the dependent variable. The Mathematica code implemented for determining the coefficients, c_{i_1,i_2}, is shown in appendix C. $HU(S_1, S_2)$ of equation (7) best describes the average CT number $\overline{CT}_{i,j}$ as a function of the MRI intensity values S_1 and S_2. Note that the number of data points within a bin is used as the weighting factor in the regression analysis. The weighting factor that is assigned to an empty bin is set to be 10% of the count in the nearest filled bin. The c_{i_1,i_2} data corresponding to each region that is determined for equation (7) is registered to a data file.

2.4.2 Bilinear Interpolation Method

The other prediction method is to apply a bilinear interpolation to map the two MRI intensity values to the average CT number. The map is divided into $(Nbin$ - $1)^2$ number of planes. For each plane, a bilinear interpolation is applied to four neighboring data points to determine a partial mapping function that describes that specific plane. The four neighboring data points have the MR bin indices, (i_1, j_1), (i_2, j_1), (i_1, j_2), and

(i_2, j_2), and their corresponding average CT numbers, A, B, C, and D. The bin indices, i_2, and j_2, are defined as $i_2 = i_1 + 1$ and $j_2 = j_1 + 1$, respectively. The mapping function describing the plane is formulated as the following:

$$\begin{aligned} HU(S_1, S_2) &= c_0 + c_1 S_1 + c_2 S_2 + c_3 S_1 S_2, \\ c_0 &= A x_2 y_2 - B x_1 y_2 - C x_2 y_1 + D x_1 y_1, \\ c_1 &= x_1(B - D) + x_2(C - A), \\ c_2 &= y_1(C - D) + y_2(B - A), \\ c_3 &= A - B - C + D, \end{aligned} \tag{8}$$

where x_1, x_2, y_1, and y_2 are the MR bin indices, i_1, i_2, j_1, and j_2, plus $-\frac{1}{2}$, respectively. The four coefficients, c_0, c_1, c_2, and c_3, are determined so that HU(S_1,S_2) reproduces the corresponding average CT values, A, B, C, and D, of the four neighboring points. The c_0, c_1, c_2, and c_3 data of each plane are determined for each region and are stored in a data file.

2.5 Generation of Pseudo-CT

To generate pCT values for a target patient, the anatomical structures on the MR_1 and MR_2 images of the target patient are segmented into the same types of regions: bony, soft, and mixed regions. An excluded region is not used for the target patient and all voxels within the body contour are inputed into the prediction model to convert to their respective pCT numbers.

For each voxel in the the target patient, first its region is determined from the segmentation mask and the corresponding prediction model of equation (7) is selected. Next, the voxel intensity of the MR_1 and the MR_2 from the same voxel position are both extracted. Finally, the voxel intensities are applied to the corresponding prediction

model equation to calculate a pCT number. The same process is repeated for all voxels within the body contour to generate the full pCT image volume.

The programmed script shown in appendix D is created and executed on Matlab to determine the region of the voxel from the segmentation masks, to apply the corresponding coefficients c_{i_1,i_2} to equation (7), and to map the S_1 and S_2 MRI intensity values to an expected CT number. Note that the predicted CT number is restricted to the maximum and minimum threshold of -1000 HU and 2000 HU. The pCT images are then generated for the target patient after the CT numbers are generated for all the voxels.

The LOOCV is applied to the six patients to evaluate the accuracy of our method. There are six cycles, where five patients are used as training data to determine the coefficients, c_{i_1,i_2}, in equation (7) for each region and then the prediction model is applied to the remaining (target) patient following Table 2.

2.6 Electron Density Conversion

The conversion of CT number to electron density values is unique to the CT scanner and the operational energy. CT numbers are interpolated to relative electron density values via the Hounsfield lookup table in the database of the treatment planning system. The interpolation process is achieved automatically through the treatment planning system.

2.7 Radiation Treatment Plan

To further assess the accuracy of pCT with a relevant RT quantity and to illustrate the utilization of the generated pCT image volume in RT, a simplified treatment plan is created on an Eclipse treatment planning system (Varian Medical System, Palo Alto, CA, USA).

The treatment plan uses one anterior beam and two posterior oblique beams. The planned target volume (PTV) is the cervix. Contours for the left and right femur heads, bladder, bowel, and rectum are drawn manually on the treatment planning system. Identical contours and PTV are drawn on the rCT and pCT with the same size and shape. For the excluded regions (the bladder and bowel), where the rCT and MR images differ significantly, the CT numbers for the bladder and bowel are overridden and then assigned as 5 HU and 45 HU, respectively, for both the pCT and rCT.

A treatment plan is first created on the rCT. The anterior beam is set to a gantry angle of 0° at the PTV. The two posterior oblique beams have mirror gantry angles to avoid passing through the spinal cord, the right femur head, and the left femur head. All three-irradiation beams are shaped to the contour of the PTV from the beam's eye view. The center of the PTV is prescribed a dose of 56 Gy and all three beams are equally weighted for simplicity. The treatment plan created on the rCT is copied onto the pCT. Dose distributions are calculated separately for the rCT and the pCT treatment plans for comparison using the same electron density conversion.

2.8 Software Tools

This section describes the software tools, Matlab, Mathematica, and Eclipse, used in this dissertation.

2.8.1 Matlab

Matlab (http://www.matlab.com) provides a numerical computing environment and a high-level computational language. With pre-built toolboxes, it allows plotting, implementation of algorithms, fast problem solving, and data visualization. The image processing (generation of target pCT) and data analysis in this thesis are accomplished

through functions created using the Matlab programing language.

2.8.2 Mathematica

Mathematica is a symbolic as well as numerical mathematical computation program that provides built-in nonlinear regression solver. Nonlinear regression analysis is performed during the training phase on the polynomial function to determine the coefficients for our prediction model.

2.8.3 Eclipse

Eclipse(TM) is an integrated treatment planning system that supports a wide variety of treatment options including external beams. The simulated radiation treatment plans are created and then the dose distributions are calculated on the Eclipse treatment planning system.

2.9 Verification Metrics

This section describes the measurements used to evaluate the accuracy of the generated pCT for voxel-wise comparison and comparison of the calculated dose distributions.

2.9.1 Mean Absolute Error

The most commonly use method to evaluate the quality of a generated pCT images is by determining the mean absolute error (MAE) as define below:

$$MAE = \frac{1}{N}\sum_{k=1}^{N}|pCT_k - rCT_k|, \tag{9}$$

where N is the total number of body voxels (except the voxels from the excluded region) of the target patient, pCT_k and rCT_k denote respectively the value of the generated pCT

and the reference CT (rCT) for voxel k. The MAE thus measures the voxel-wise average absolute error. When evaluated for each region, N in equation (9) represents the total number of body voxels in that region of the target patient.

2.9.2 Dose Comparison

The gamma index method compares two dose distributions spatially according to acceptance criteria of dose and distance to agreement (DTA) by the following equation:

$$\Gamma(\vec{r}_e, \vec{r}_r) = \sqrt{\frac{|\ \vec{r}_e - \vec{r}_r\ |^2}{\Delta d^2} + \frac{[D_e(\vec{r}_e) - D_r(\vec{r}_r)]^2}{\Delta D^2}}, \tag{10}$$

where $\vec{r}_e$ is the vector position of the evaluated point, $\vec{r}_r$ is the vector position of the reference point, $D_e(\vec{r}_e)$ is the evaluated dose, $D_r(\vec{r}_r)$ is the reference dose, ΔD is the dose difference criteria, and Δd is the DTA. The minimum value of Γ is the value of γ

$$\gamma(\vec{r}_r) = min\{\Gamma(\vec{r}_e, \vec{r}_r)\}\{\vec{r}_e\}. \tag{11}$$

A voxel is considered to pass the gamma index criteria if and only if $\gamma(\vec{r}_e) \leq 1$. A commonly used acceptance criteria is $\Delta D = 2\%$ and $\Delta d = 2mm$.

In this thesis, the voxel-to-voxel dose comparison is used to compare the dose distribution on the pCT and the rCT instead.

$$ScaledDose_{diff}(\vec{r}) = \sqrt{\frac{[D_e(\vec{r}) - D_r(\vec{r})]^2}{\Delta D^2}}, \tag{12}$$

where $\vec{r}$ is the vector position, and $D_e(\vec{r})$ and $D_r(\vec{r})$ are the evaluated and reference doses, respectively. The dose tolerance, ΔD, is set to 2%. Equation 12 is a more strict comparison of dose distribution than equation 11 because it does not search for a local minimum within a DTA.

3 Results

This chapter presents all attained results relevant to this dissertation. Section 3.1 presents data that justify the necessity of segmenting voxels based on tissue type and an example of the segmentation mask used for a patient. Section 3.2 demonstrates the purpose of the bin filling step. Section 3.3 presents the key results in this dissertation: the 3D-plots of the polynomial prediction function, an example of the generated pCT image volume, and the comparison of pCT to rCT for all cycles. Section 3.4 presents the images of the dose distribution of the treatment plan and the passing rate for each cycle when comparing the dose distribution of the pCT treatment plan to that of the rCT treatment plan. Finally, section 3.5 presents the results from tests of alternative methods.

3.1 Segmentation Mask

Figure 6 shows the distribution of MR_1 and MR_2 voxel intensities for bony (blue) and soft (red) regions. This figure confirms the necessity to segment voxels based on tissue type as noted by other studies [33, 36, 61]. The voxels from bony (blue) and soft (red) regions on the two-dimensional plane of the MR_1 and MR_2 intensity values shown in Fig. 6 have a large overlapping area. This overlapping region is a significant contributing factor to errors in generating pCT, and it causes the prediction models to underestimate the CT number for bony tissues while overestimate the CT numbers for soft tissues. Thus, the anatomical structures are segmented into regions and separate prediction models are determined for each region.

The segmentation masks of bony, soft, and mixed regions used for patient1 are shown for a sequence of axial slice images in Fig. 7. The segmentation masks show extended areas for the mixed region for several axial slices. This is to account for volume averaging

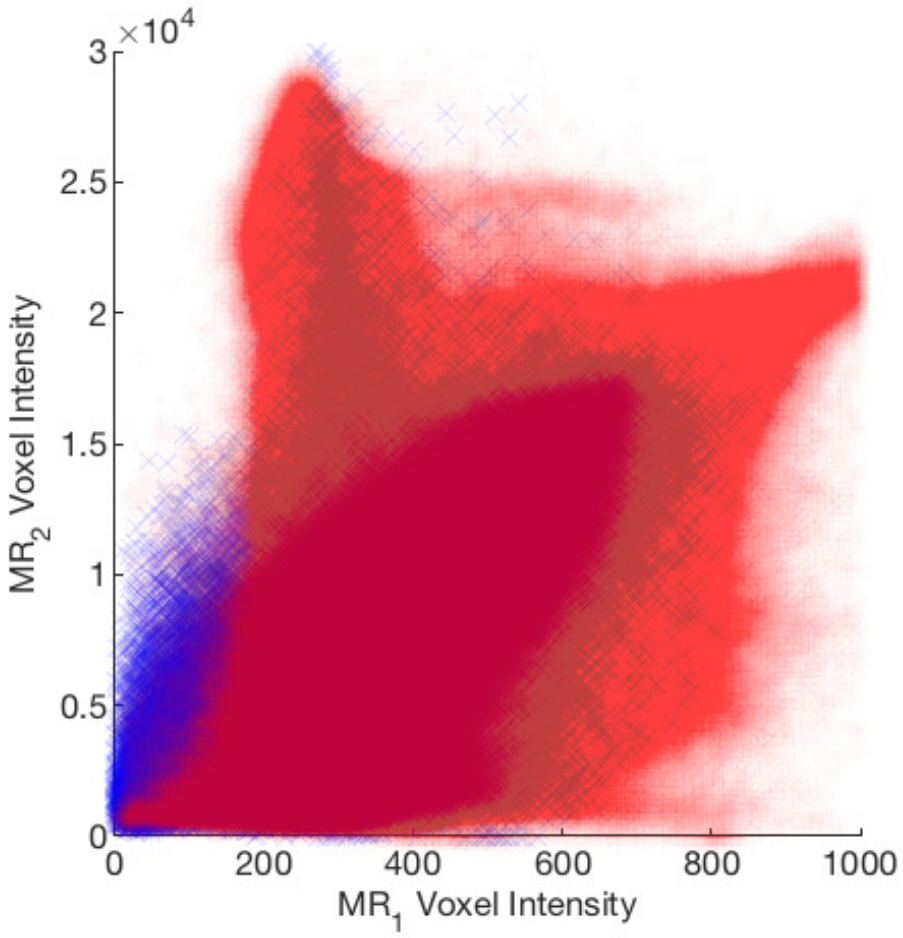

Figure 6: Distribution of voxels on the MR_1 and MR_2 plane from the bony tissue (blue) and soft tissue (red) of all six patients.

between slices and uncertainty in the hip joint bone-soft tissue interface.

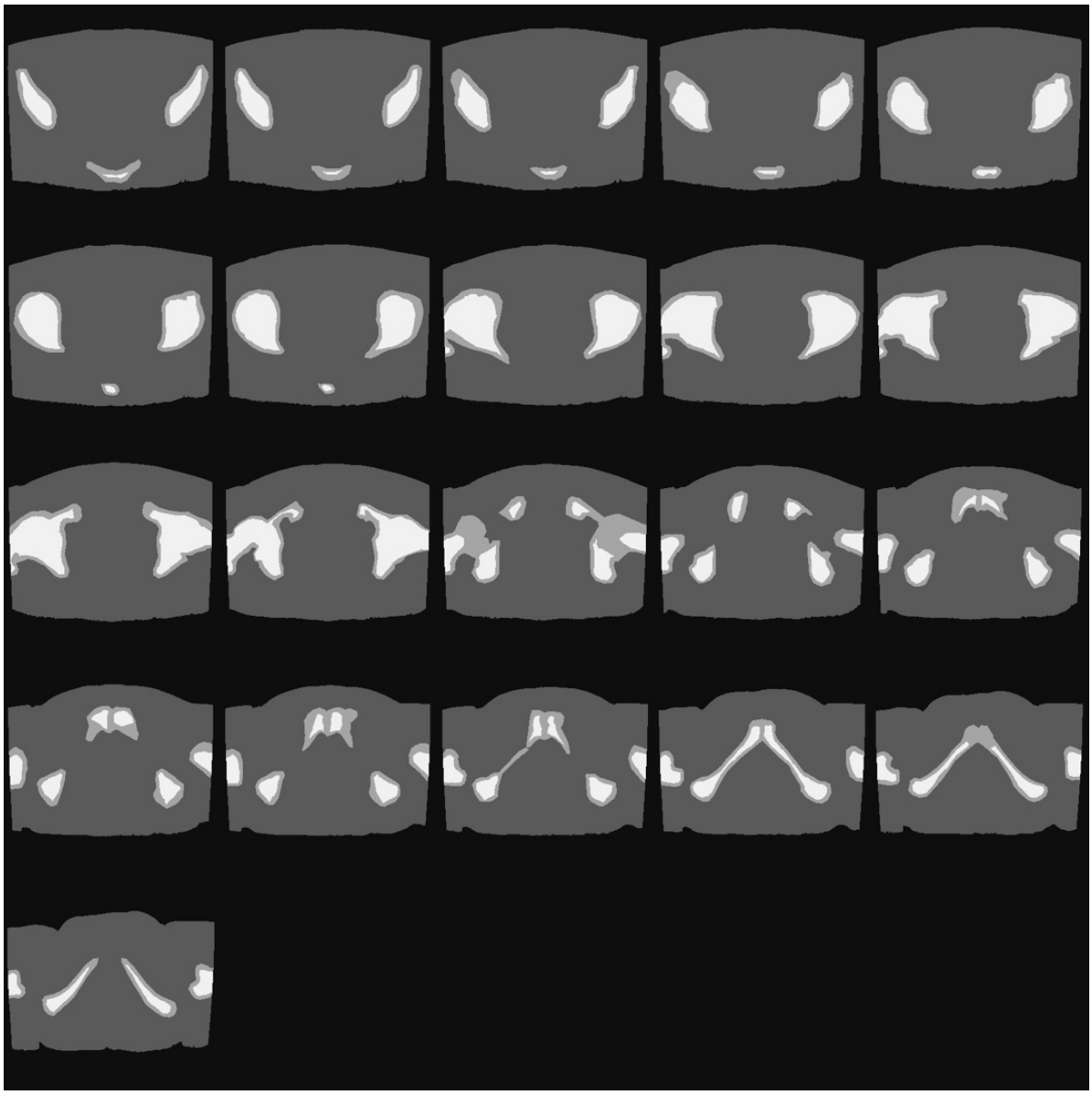

Figure 7: A sequence of segmentation masks in the axial slice orientation created for Cycle1 with the bony region (white), the soft region (dark gray), and the mixed region (light gray).

3.2 Bin Filling

At section 2.3.1, it is unknown if the 'empty bins' seen in Fig. 5A are due to the small sample size or the actual distribution of the average CT number (HU), $\overline{CT}_{i,j}$, versus the MR_1 and MR_2 bin numbers. However, the inclusion of the 'bin filling' step fulfills two

purposes: first, as explained in section 2.3.1, it improves the stability of the prediction model; and secondly it resolves the issue shown in Fig. 8A, where neighboring voxels have high (white) and low (black) predicted HU value, although this error mainly exists

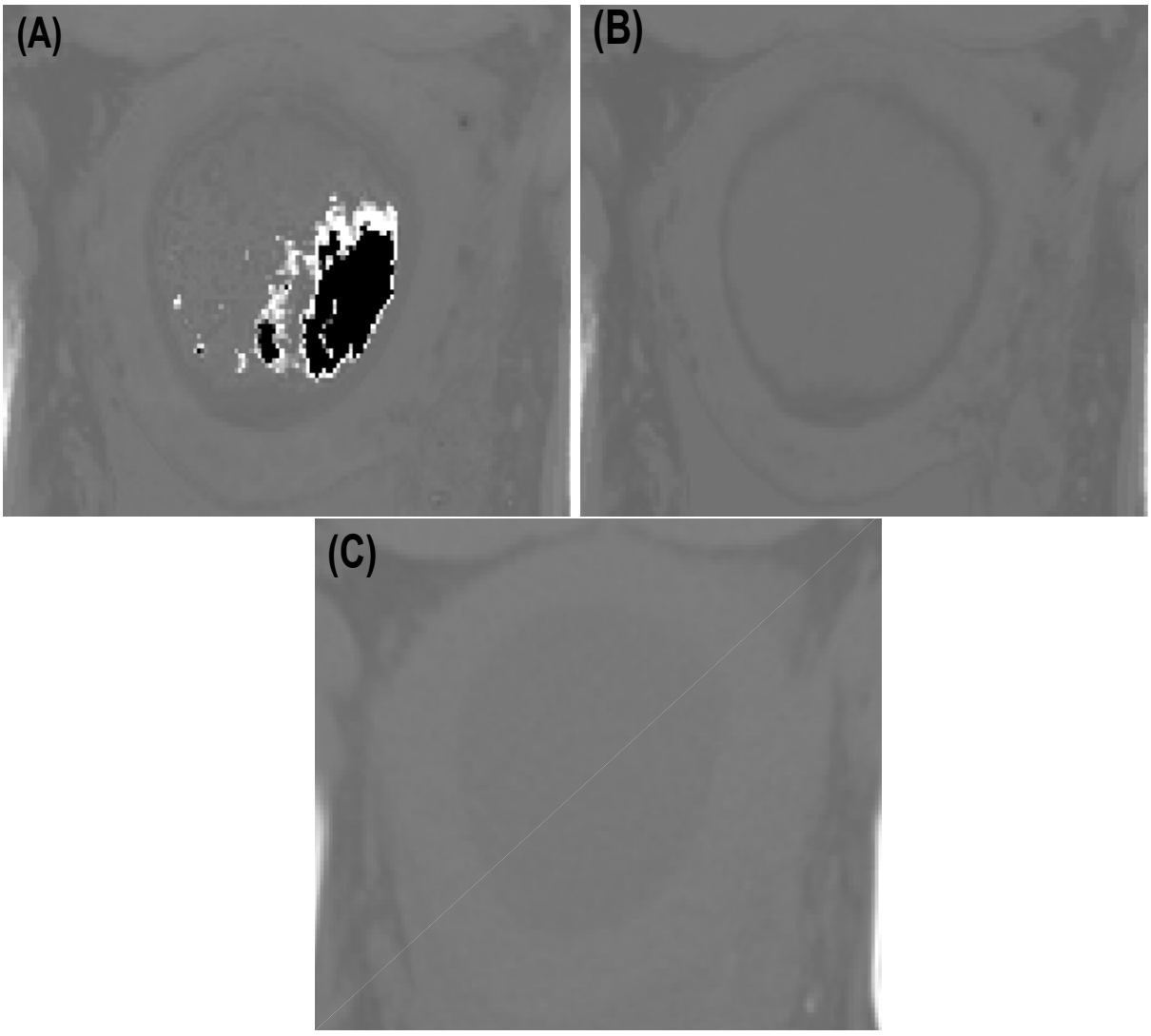

Figure 8: Effect of bin filling on pCT image: (A) without bin filling. (B) with bin filling. (C) Reference-CT.

within the excluded area and therefore normally has no effect on the evaluation of the prediction model. In a normal CT image as seen from Fig. 8C, neighboring voxels do not have such a significant difference in CT number.

Without bin filling, the predicted HU values for the white and black voxels observed in Fig. 8A are $\gg$ 2000 and $\ll$ -1000, and thus the values of 2000 HU and -1000 HU are assigned instead, respectively. We find that the MR_1 and MR_2 intensity values at the corresponding voxel are values outside the range of the training data MR intensity values. A limitation to the polynomial model is the rapid deterioration of extrapolated data outside the range of training data [62], e.g. possible target patient MR_1 and MR_2 voxel intensity values residing in the 'empty bin' and leading to a large error in prediction of HU value. Therefore, to ensure the robustness and to circumvent this issue, the 'Bin Filling' step described in section 2.3.1 is used. The reference CT, Fig. 8C, shows the voxel position of the white and black voxels on Fig. 8A corresponds to an application (i.e. implant) within the patient, thus the area is within the excluded region. This issue reveals that for a target patient with MR values outside the range of training data, it is likely that the prediction model will greatly overestimate or underestimate the predicted CT number, which tends to be outside the range of the HU scale of -1000 HU to 2000 HU. With the inclusion of the 'bin filling' step, the issue of neighboring voxels with high and low predicted HU values is not present as shown in Fig. 8B. The MAE of the target patient shows an improved result from implementing the bin filling step.

3.3 Polynomial Regression Method

Using the optimal values for polynomial degree $n = 30$ and number of MR bins $Nbin = 200$, the mapping functions are determined for the segmentation regions (bony, soft, mixed) and the three-dimensional plot (3D-plot) of the mapping functions are presented in Fig. 9 together with the binned training data.

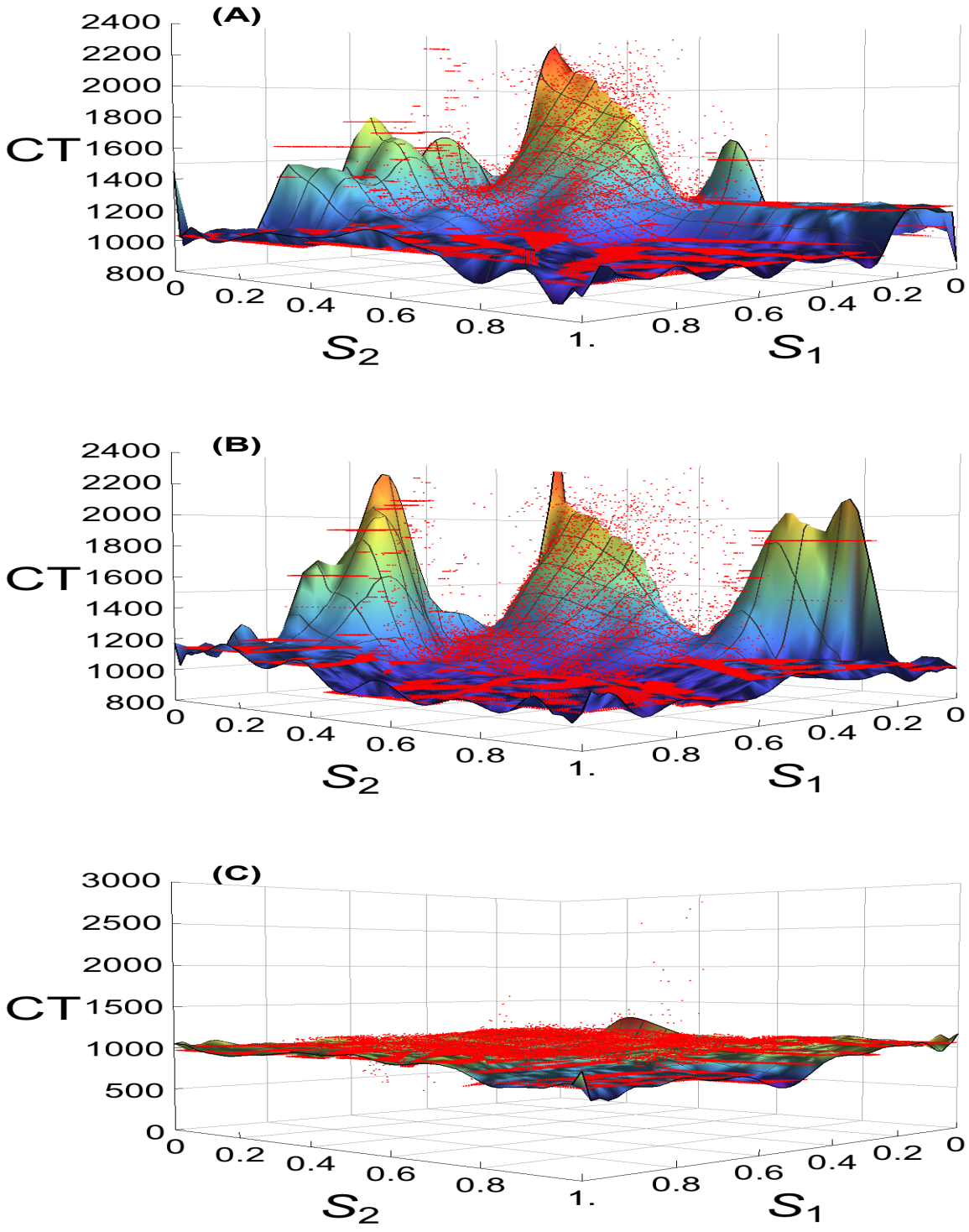

Figure 9: 3D plot of the polynomial mapping function for patient1 together with training data points (red dots) for (A) bone, (B) mixed, and (C) soft region. Note that S_1 and S_2 here represent respectively the MR_1 and MR_2 value after being normalized by their respective maximum value.

Overall, the 3D-plots of the mapping function show that the polynomial function of each region resembles the shape and trend of the training data (red dots), thus proving that the mapping functions are successful in modeling the complex correlation between MR_1, MR_2, and CT number. However, it is observed that the surface of the mapping function for the bone and the soft region does not extend to a few of the training data points (red dots). This is possibly due to a lower weighting of these bins where the CT numbers of the neighboring bins are more important for the mapping function.

3.3.1 MRI, Reference-CT and Pseudo-CT Image Volumes

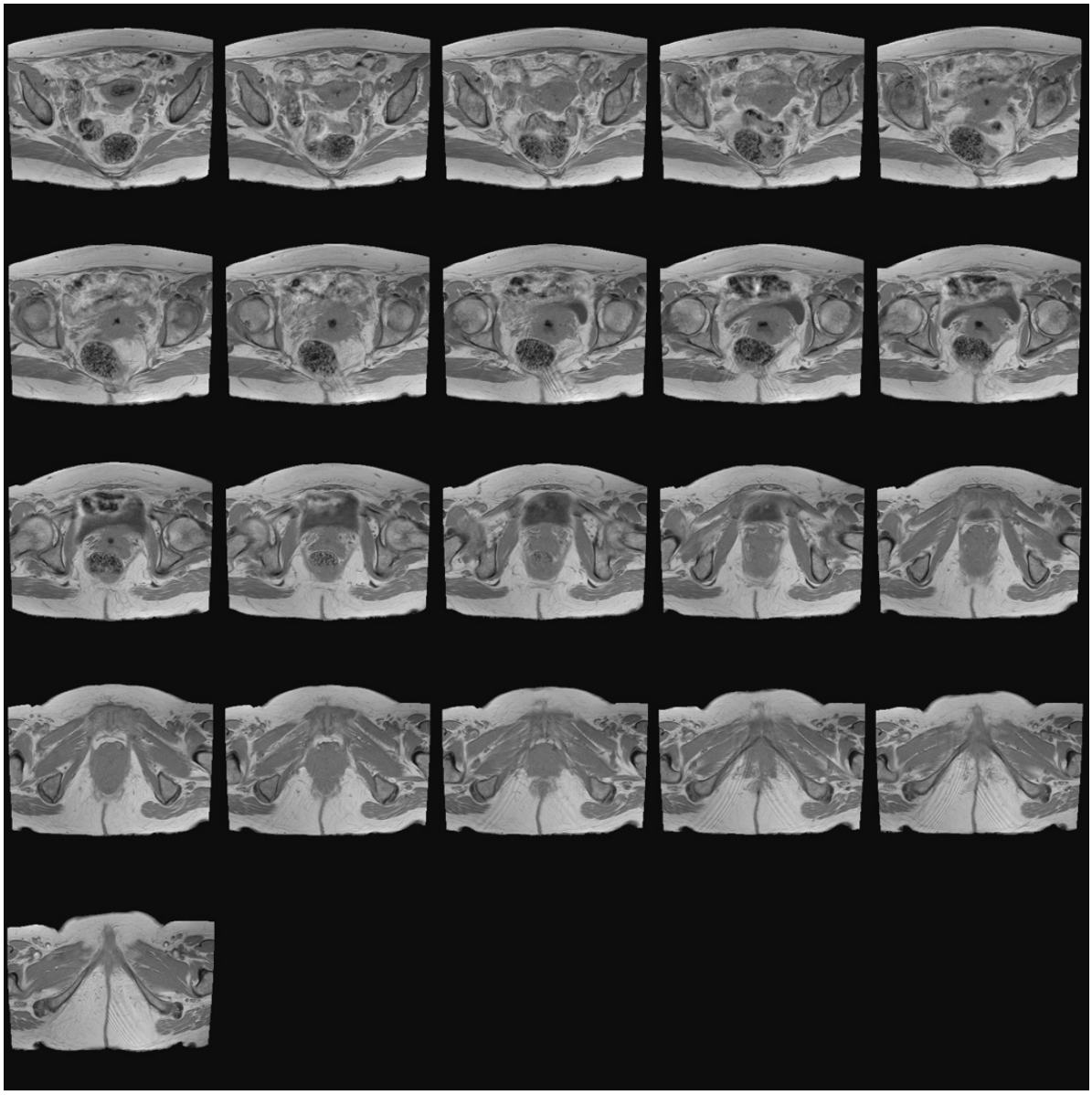

Figure 10: A sequence of MR_1 axial slice images for Cycle1.

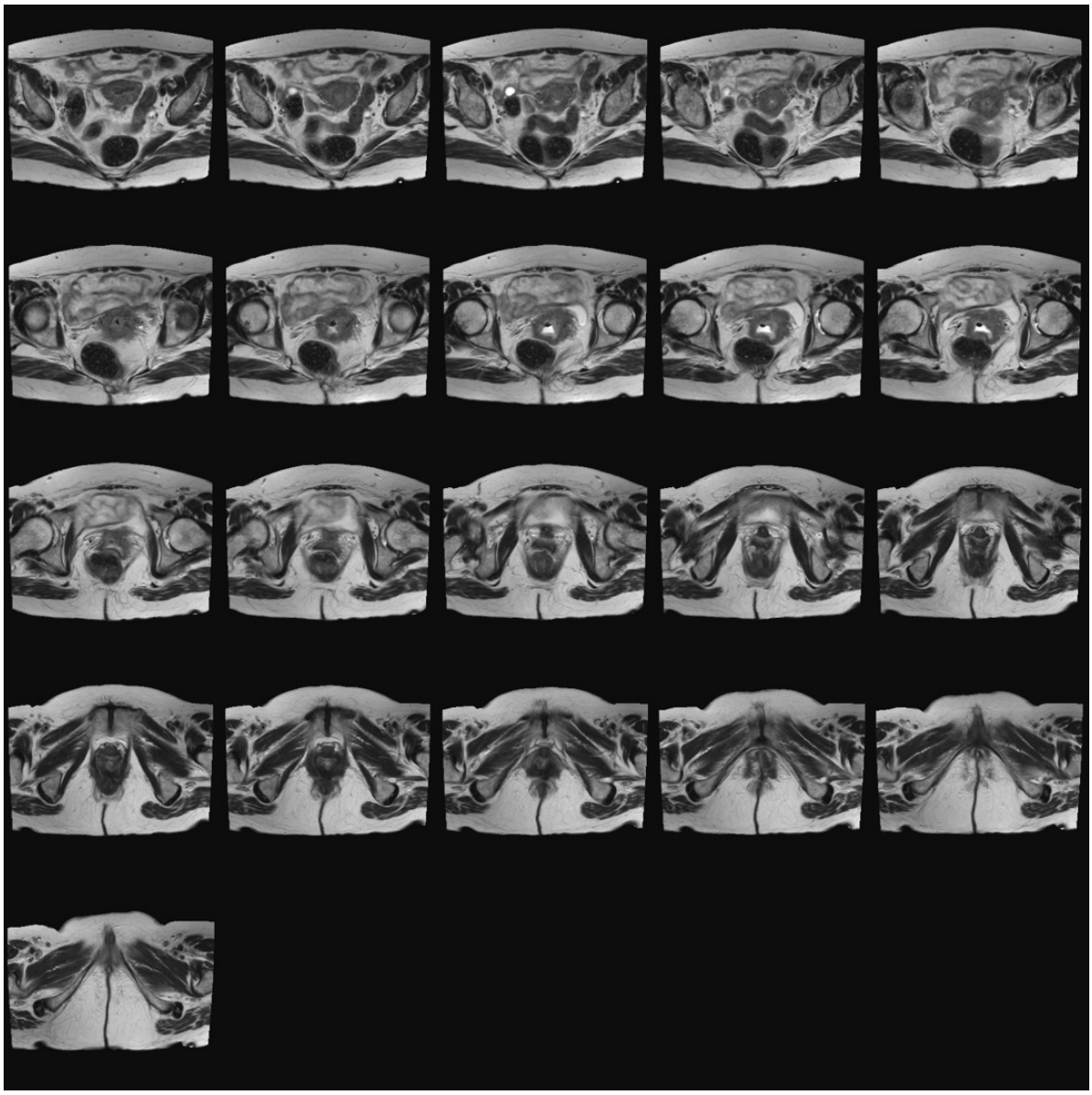

Figure 11: A sequence of MR_2 axial slice images for Cycle1.

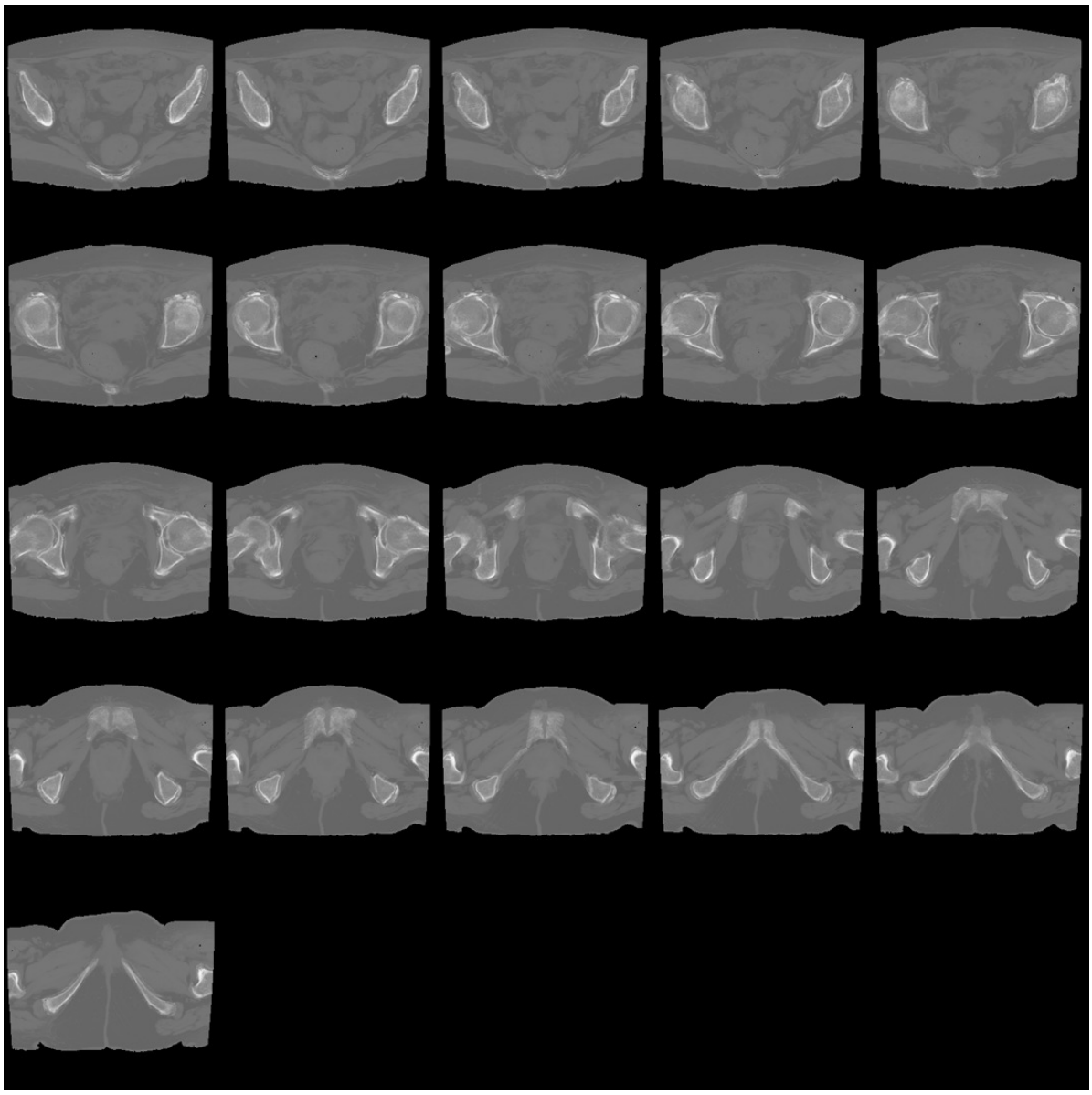

Figure 12: A sequence of pCT axial slice images for Cycle1.

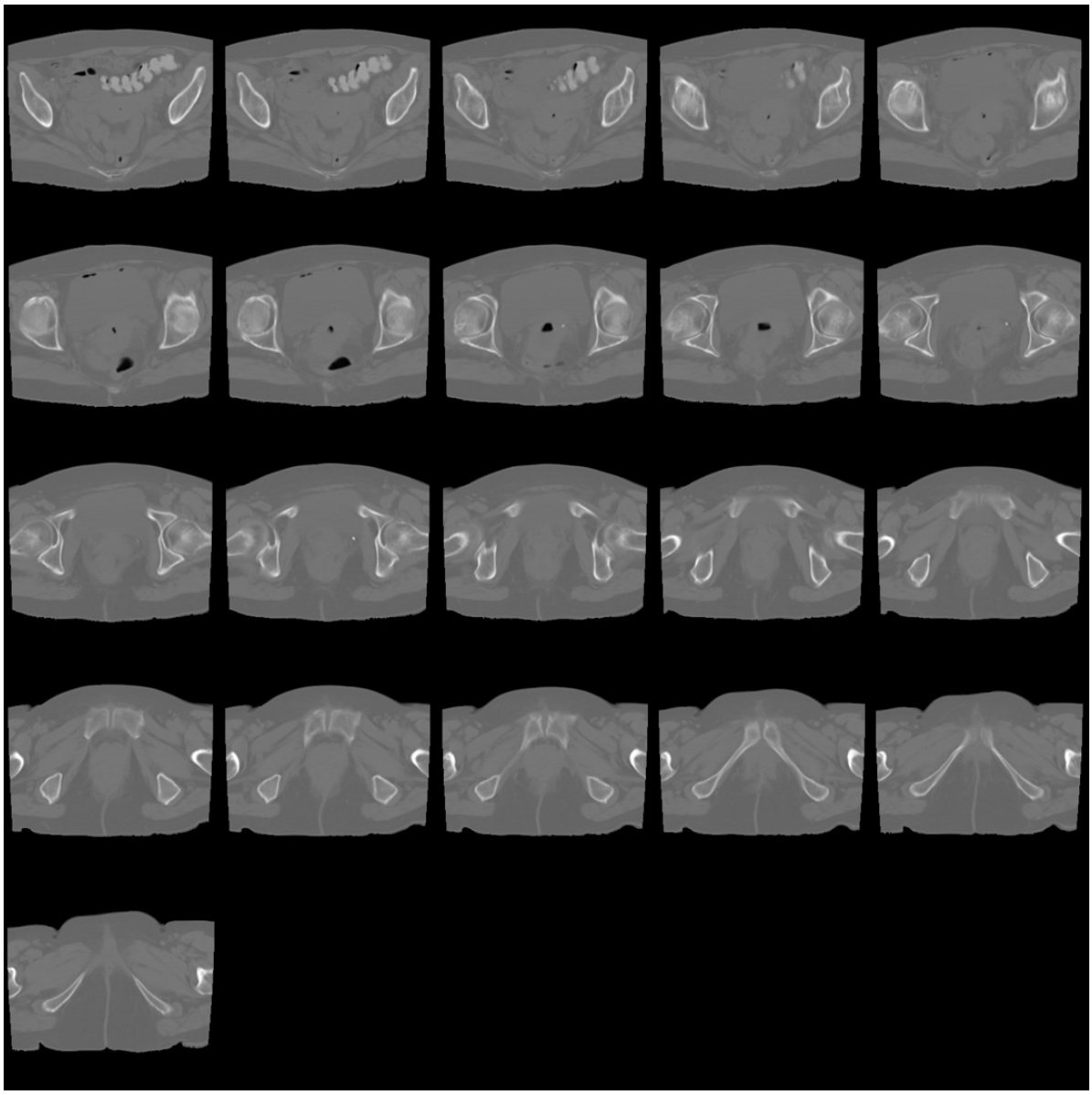

Figure 13: A sequence of rCT axial slice images for Cycle1.

Applying the polynomial mapping function to the data of the target axial image sequence of MR_1 (Fig.10) and MR_2 (Fig.11), the generated sequence of axial pCT images can be seen in Fig.12. Comparing the generated sequence of axial pCT images to the rCT images Fig.13, the overall image for each axial slices are similar except for the intestinal area, where on the rCT there are trapped gas or fecal matter in the bowel.

This difference is also seen between the sequence of MR and rCT images.

A comparison of one axial slice of the patient's MRI (MR_1 and MR_2), reference CT, and generated pseudo CT image at the same location is shown in Fig. 14. The pCT image

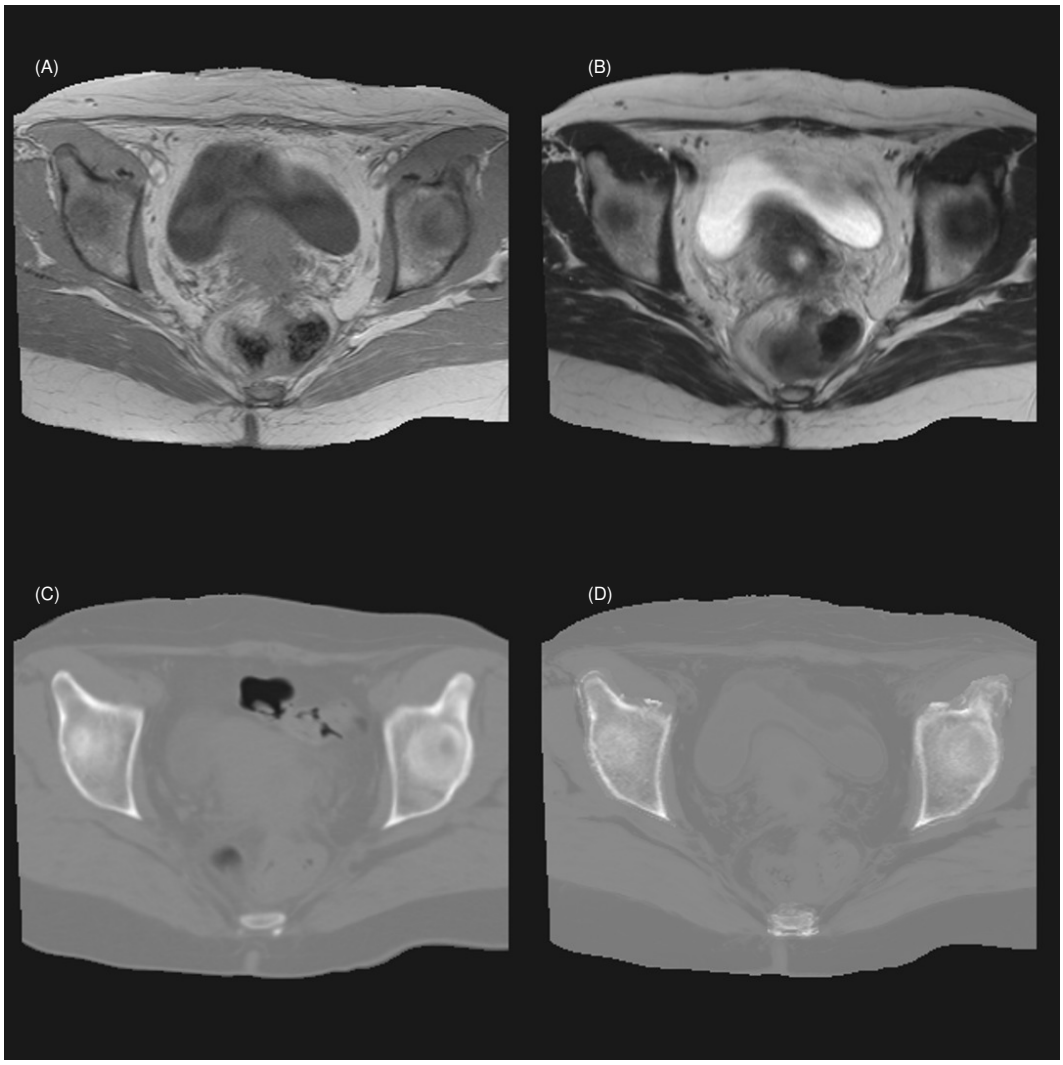

Figure 14: Axial views of the (A) MR_1, (B) MR_2, (C) rCT, and (D) generated pCT image at a given location of a target patient (cycle4).

(Fig. 14D) closely matches the rCT (Fig. 14C) with a few noticeable structural differences predominantly in the soft tissues, specifically the bladder and bowel. Similar differences are also observed between the rCT (Fig. 14C) and MRI images (Fig. 14A & B). Other minor differences are observed at the muscle-fat tissue and bony-tissue interface including

the spinal cord. The differences can be attributed to the usage of a different couch setup during scanning and the difficulty in replicating the same patient position between different modalities when there is a significant time gaps between acquisitions. The major differences (e.g. bladder and bowel daily changes) between the CT and the MRI images are caused by the extended period between the acquisition of the CT and the MRI images. This is why the regions with such major differences have been segmented as the excluded region and thus are not included in determining the prediction model or in calculating the MAE values. In addition, for a target patient, these differences will be nonexistent because a CT scan is not needed, which is the key advantage of MRI-only RT. Similar observations can be made from the other cycles shown in appendix B.

3.3.2 Voxel-Wise Comparison

The rCT and pCT images are compared voxel-to-voxel via the mean absolute error to evaluate the accuracy of the prediction model. Table 3 presents the voxel-wise

	Mean Absolute Error (HU)						
	Overall	Soft Region		Bony Region		Mixed Region	
		Raw	Weighted	Raw	Weighted	Raw	Weighted
Cycle1	44.4	25.8	21.1	118.5	12.1	138.3	11.2
Cycle2	42.7	25.6	20.9	100.2	8.1	134.3	13.7
Cycle3	40.9	24.8	20.8	104.0	9.6	151.8	10.4
Cycle4	38.7	23.0	19.5	105.6	9.5	157.0	9.7
Cycle5	38.1	24.6	20.9	99.7	8.8	135.8	8.4
Cycle6	36.7	23.9	20.4	88.0	8.0	143.6	8.3
Average	40.3	24.6	20.6	102.7	9.4	143.5	10.3
± SD	±3.0	±1.0	±0.6	±9.9	±1.5	±9.2	±2.0

Table 3: MAE values between pCT and reference-CT for the overall patient volume and for each segmented (bony, soft, and mixed) region of each LOOCV cycle and their average values for all six cycles. The raw MAE values are determined from comparing voxels only within the specified regions. The weighted MAE values are determined from the raw MAE values multiplied by the percent of voxels in the specified region.

comparison of pCT and rCT image volume for each individual patient and the average

values for all six patients. The average MAE for the overall volume in the images is 40.3 ± 3.0 HU, while the MAE values for the bony, soft, and mixed regions are 102.7 ± 9.9 HU, 24.6 ± 1.0 HU, and 143.5 ± 9.2 HU, respectively. The weighted MAE value for a region is determined by multiplying the unweighted (raw) MAE value by the percent of voxels in that region (Table 4). The sum of the weighted MAE values of the three regions equals the overall MAE value.

As stated previously for Fig. 14, the bone-tissue interface has the most noticeable differences and the high unweighted MAE values for the mixed region in Table 3 support this observation. This is because the mixed region consists mainly of the bone-tissue interface, where the registration errors are the highest between MRI and rCT images. Table 4 presents the percent of voxels from each region. The bony region and the mixed

Percent of voxels from each region			
	Soft Region	Bony Region	Mixed Region
Cycle1	81.8%	10.2%	8.0%
Cycle2	81.6%	8.1%	10.3%
Cycle3	83.9%	9.2%	6.9%
Cycle4	84.8%	9.0%	6.2%
Cycle5	85.0%	8.8%	6.2%
Cycle6	85.4%	9.1%	5.5%
Average	83.8%	9.1%	7.2%

Table 4: Percent of voxels from each region.

region account for only a small percentage (on average 9.1% and 7.2%, respectively) of all the voxels in the imaged volume, their contributions to the overall MAE (i.e., their weighted MAE values) are lower than that of the soft region.

3.4 Dosimetric Comparison of Pseudo-CT and Reference-CT

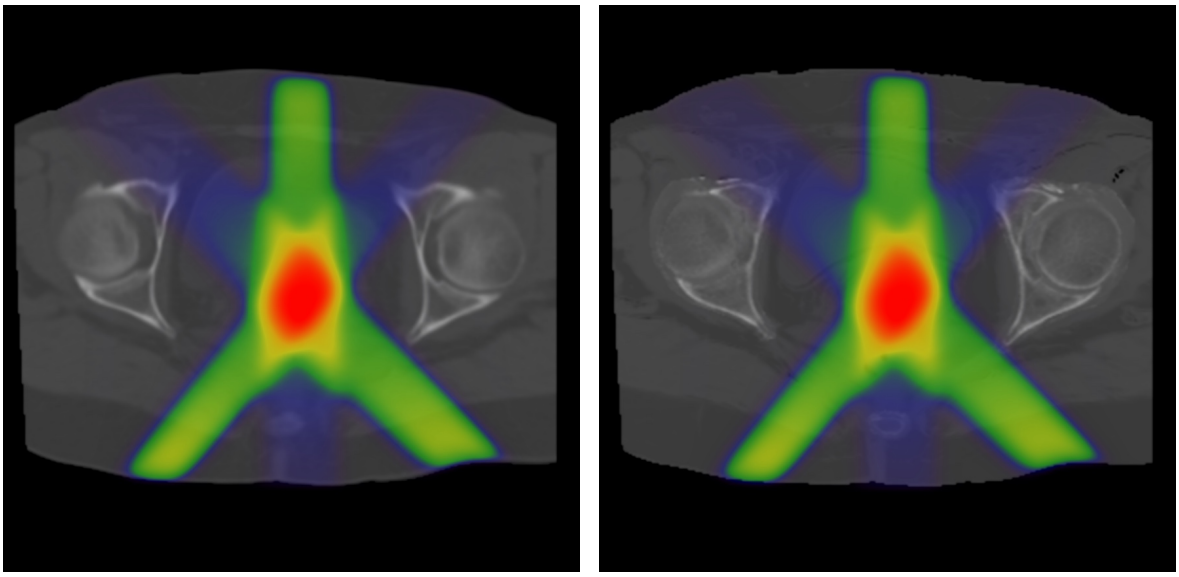

Figure 15: An axial image of rCT (left) and pCT (right) with overlay of dose distribution for cycle4.

The purpose of section 2.7 is to verify that the generated pCT can be imported into a TPS, the dose distribution can be calculated, and the voxel-to-voxel dosimetric comparisons show a close agreement between the treatment plans created on pCT and rCT. Therefore we have created a simple treatment plan on the rCT as described in section 2.7 targeting the cervix. The TPS calculates the dose distribution for the treatment plan and Fig. 15 (left) shows the calculated dose distribution overlaid on an axial slice rCT image. The treatment plan created on the rCT is replicated onto the pCT. Using the same electron density conversion lookup table as the rCT treatment plan, the dose distribution is calculated for the pCT treatment plan. Figure 15 (right) shows the calculated dose distribution overlaid on an axial slice pCT image.

The voxel-to-voxel dose comparison described in section 2.9.2 is performed on the pCT and the rCT treatment plan with a passing criterion of 2% for the dose difference tolerance. Passing voxels within the body contour are tabulated and a passing rate is

calculated. Table 5 presents the dose comparison results for individual patients, where an average passing rate of 95.4% is obtained in the point-to-point dose comparisons between the pCT and rCT treatment plans.

	Cycle1	Cycle2	Cycle3	Cycle4	Cycle5	Cycle6	Average
Passing rate	95.7%	94.8%	95.8%	96.2%	95.7%	94.2%	95.4%

Table 5: Passing rates (with a dose difference less than 2%) from the point-to-point dose comparisons between the pCT and rCT treatment plans.

3.5 Tests of Alternative Methods

This section presents the test results of alternative methods to generate the pCT image volume. The alternative methods are using only a singular MRI set (MR_1 or MR_2), determining the polynomial prediction model without segmentation masks, and using a bilinear interpolation prediction model to generate the pCT. Alternative methods are to evaluate the effect of singular MRI set (one-variable) compared to two MRI set (two-variable) and the effect of segmentation on generating pCT.

3.5.1 Using a Single MRI Set

Using only a singular MRI set (MR_1 or MR_2), the method is identical to those described in section 2 if the segmentation and exclusion masks were the same. The difference is that there is only one independent variable, S:

$$HU(S) = \sum_{i=0}^{i \leq n} c_i \, S^i = c_0 + c_1 S \ + \cdots + c_n \, S^n, \tag{13}$$

where n is the highest polynomial degree, $HU(S)$ is the dependent variable of the mapping function, S is the intensity value from MR_1 or MR_2, and c_i is the $i-th$ fitting coefficient.

3.5.2 Using Two MRI Sets without Segmentation

The other alternative method is generating pCT using two MRI sets but without segmentation. Identical steps in section 2 are followed, except that the creation of the segmentation masks described in section 2.2.3 is left out. The polynomial mapping function remains the same as equation (7).

For both alternative methods, the same optimal values for the number of MR bins and the polynomial degree are used. Table 6 presents MAE comparison of using both

	Mean Absolute Error (HU)			
	Default Method	MR_1 only	MR_2 only	Using Two MR Sets but Without Segmentation
Cycle1	44.4	48.2	55.6	66.0
Cycle2	42.7	47.3	64.4	65.3
Cycle3	41.3	46.1	81.5	61.9
Cycle4	38.6	44.1	64.6	60.8
Cycle5	38.1	41.7	53.2	64.7
Cycle6	36.7	40.8	66.4	59.5
Average	40.3	44.7	64.3	63.0
± SD	± 3.0	± 3.0	± 10.0	± 2.6

Table 6: MAE values from the method using two MRI sets with segmentation (default method) in comparison with those using only one MRI set or using two MRI sets but without segmentation.

multiple MR sets and segmentation (default method) to using singular MR set (only MR_1 or only MR_2) or using two MR sets but without segmentation. The MAE values without segmentation, 63.0 ± 2.6 HU, and current method, 40.3 ± 3.0 HU, further prove the essential need for tissue segmentation similar to the findings in section 3.1. The use of two MR sets, 40.3 ± 3.0 HU, compared to using a singular MR set, 44.7 ± 3.0 HU for MR_1 only and 64.3 ± 10.0 HU for MR_1 only, has an improvement on the MAE value. Of interest is that using only the MR_2 set results in worse MAE values compared to using only the MR_1 set. This is likely due to the difference in nuclear magnetic resonance properties between that of MR_2 data acquired with a T2-weighted sequence to that of

MR_1 data acquired with a T1-weighted sequence. This also shows a need for developing and optimizing specific MR sequence parameters of near-orthogonal contrast properties for use in MR to pCT generation.

3.5.3 Bilinear Interpolation Method

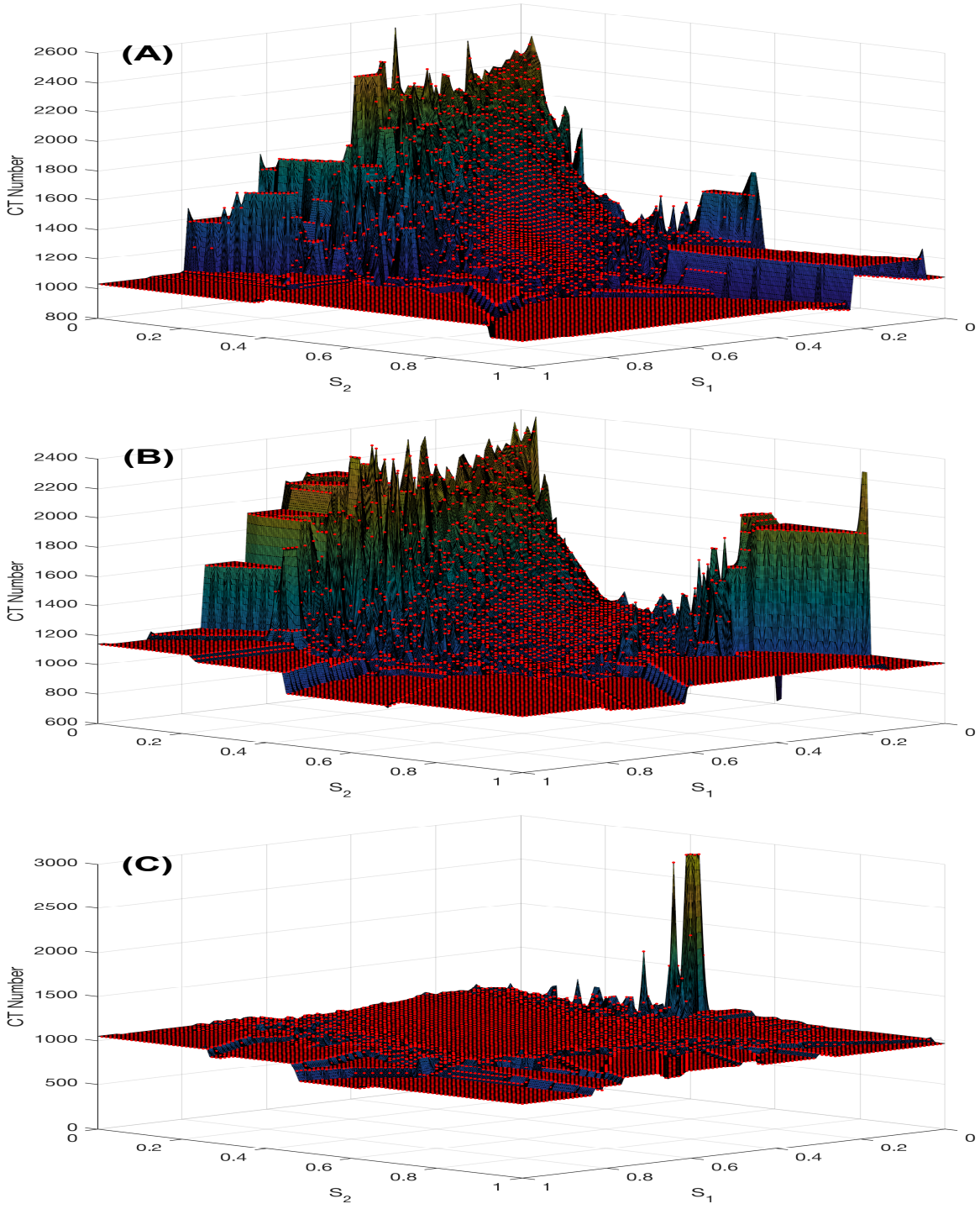

Figure 16: 3D plot of the bilinear interpolation mapping function for cycle1 for (A) bone, (B) soft, and (C) mixed region. Note that S_1 and S_2 here represent respectively the MR_1 and MR_2 value after being normalized by their respective maximum value.

Another alternative method in this thesis is using a bilinear interpolation for the prediction model. Figure 16 shows the 3D-plot of the mapping functions for each region generated using the bilinear interpolation method. As expected of the interpolation method, multiple planes are situated directly between the training points (red dots). The bilinear interpolation mapping functions (Fig. 16) are somewhat similar to the polynomial mapping function (Fig. 9), except for the rough surface and the peaks seen in the soft tissue (Fig. 16B) 3D-plot. The rough surfaces are a reflection of the multiple planes interpolated between four neighboring points as described in section 2.4.2. The sharp peaks observed in Fig. 16B are due to the large HU value difference (> 1500) between four neighboring training points used to determine the interpolation plane.

	Default Method	Interpolation Method
Cycle1	44.4	44.5
Cycle2	42.7	42.9
Cycle3	41.2	41.1
Cycle4	38.6	38.8
Cycle5	38.1	38.3
Cycle6	36.7	36.9
Average	40.3	40.4
± SD	±2.9	±2.9

Table 7: Comparison of MAE values from applying the polynomial method (default method) and applying the bilinear interpolation methods

Table 7 compares MAE values using optimal *Nbin* of 200 for the polynomial and bilinear interpolation prediction model. The average MAE values are 40.3 ± 2.9 HU and 40.4 ± 2.9 HU for polynomial and bilinear interpolation methods, respectively, showing that both methods have almost equal accuracy. Individual MAE values for each cycle show that for all cycles except for cycle3 the polynomial method is within $< 0.3\%$ of the interpolation method. The results show that both models have a similar accuracy in predicting pCT numbers.

4 Discussion

This chapter examines the parameters that optimize the prediction model, the sources contributing to the error in the generated pCT and the future work related to this dissertation. First, section 4.1 examines the optimization of the two key parameters in the polynomial model: the number of MR intensity bins $Nbin$ and the polynomial degree n for the polynomial function. Section 4.2 examines in detail the sources that contribute to the difference from the generated pCT and the reference CT. Finally, section 4.3 shows possible future directions.

4.1 Optimization of Number of Bins and Polynomial Degree

Two key parameters that can be optimized in our prediction model are the polynomial degree n (for polynomial regression analysis) and the number of MR intensity bins, $Nbin$. The decision on optimal values is based on the numerical observation of MAE value, pCT image quality, computation time, and model requirement.

From Fig. 17A, an overall decreasing trend in the average MAE value as the polynomial degree n increases (with $Nbin = 200$) is observed. In particular, the polynomial model's prediction improves significantly as degree n increases to $n \sim 20$, while further increase of n changes the average MAE by no more than $\sim 1\%$. Therefore, the optimal value for the polynomial degree used in equation (7) is taken as $n = 30$.

The optimal value used in this thesis for the polynomial degree is $n = 30$. Such a high polynomial degree is desired for the model to reproduce the complicated structure [62] of the relation between MR_1 voxel intensity value, MR_2 voxel intensity value, and CT number. From Fig. 17A, a steady decrease in MAE with polynomial degree up to $n = 20$ is observed. For $n > 20$, although no significant overall change is observed, a few individual patients' MAE values decrease, showing a slight improvement in the HU value

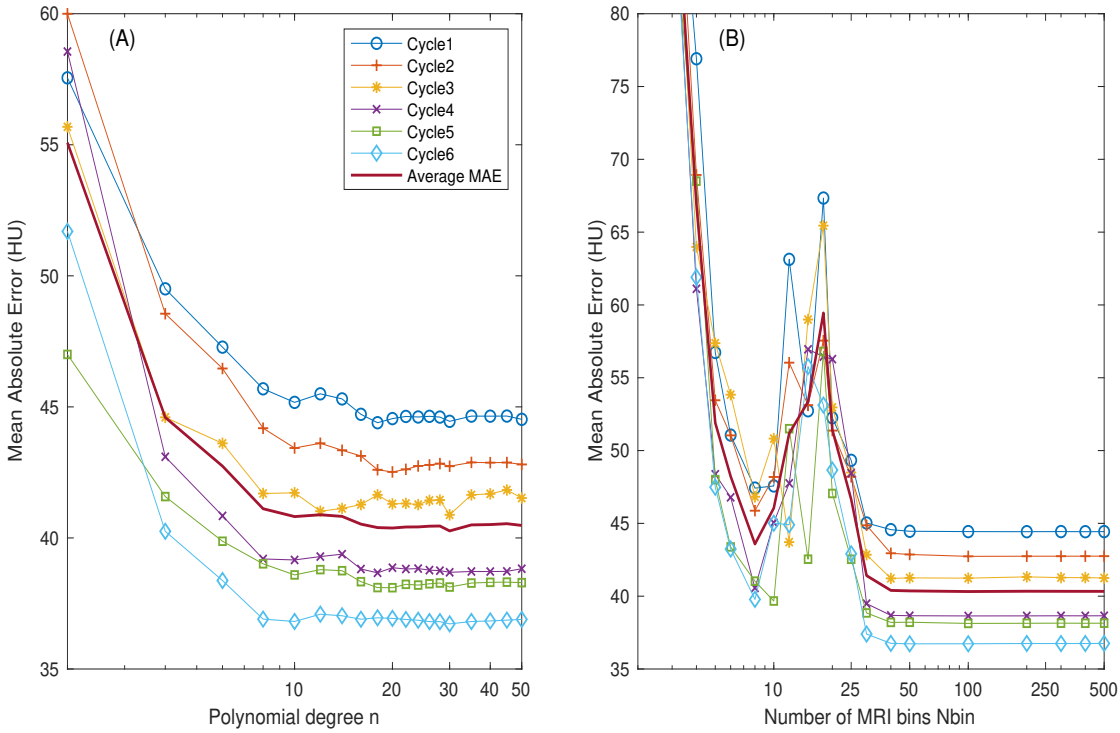

Figure 17: (A) MAE versus the polynomial degree n for all patient studies with the number of bins for each MRI set at 200. (B) MAE versus the number of bins for all patient studies with the polynomial degree set at 30.

prediction. However, computation time increases significantly when n is greater than 40 for both the regression analysis and CT number prediction.

The optimal value used in this thesis for the total number of bins is $Nbin = 200$. The value for the total number of bins represents the resolution of MR_1 to MR_2 for the regression analysis. A bigger $Nbin$ allows for more detail and variations in the training data to determine the polynomial function, therefore in theory increasing $Nbin$ has the effect of increasing resolution and improving accuracy of the prediction model. The effect of the number of MRI bins on the MAE values is shown in Fig. 17B.

Although the MAE has a non-monotonous dependence on $Nbin$ at low $Nbin$ values from 10 to 25, the average MAE values are the lowest for $Nbin > 40$. The three-dimensional (3D) plots in Fig. 18 for the polynomial function for $Nbin = 18$ and $Nbin$

= 200 show significant differences in shape for predicted HU values when the normalized S_1 and S_2 values approach 0 or 1, which may be responsible for the large MAE at *Nbin* values $\sim$ 20.

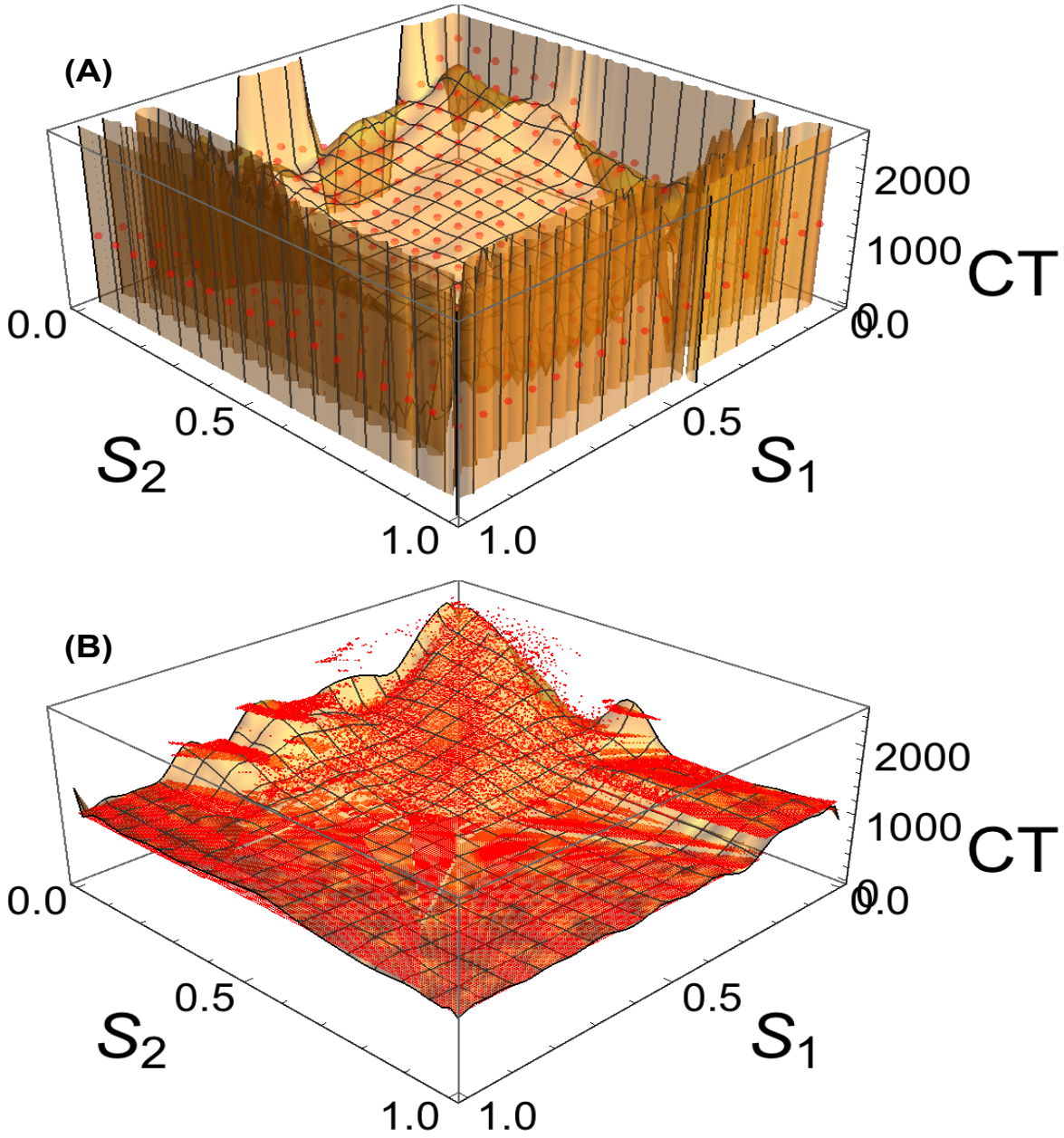

Figure 18: 3D plot of polynomial function for patient1 at (A) *Nbin* = 18 and (B) *Nbin* = 200 together with the training data points (red dots). Note that S_1 and S_2 here represent respectively the MR_1 and MR_2 value after being normalized by their respective maximum value.

For $Nbin > 100$, the average MAE decreases to 40.5 HU, with further increase of $Nbin$ giving improvement less than 0.1%. With $Nbin > 400$, similar to the case of using a large polynomial degree, the computational time increases significantly with no improvement to the CT number prediction. Therefore, $Nbin = 200$ is chosen for this thesis.

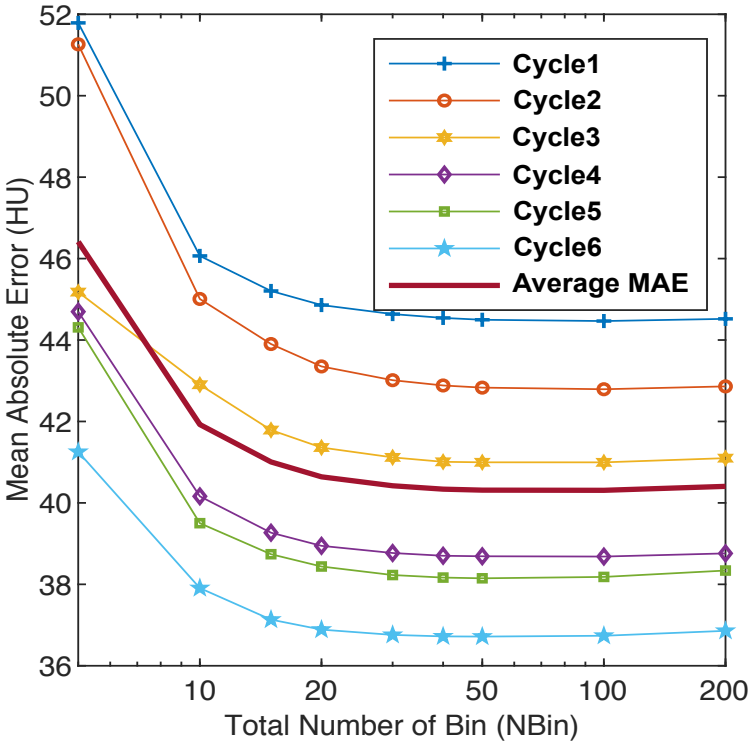

Figure 19: MAE versus $Nbin$ for all patient studies using a bilinear interpolation method.

Using the bilinear interpolation method as described in section 2.4.2, the number of bins is also optimized by observing the effect of increasing $Nbin$ on MAE as seen in Fig. 19. As expected, similar to the polynomial method, increasing the number of bins results in an observed decreasing MAE value. Because the bilinear interpolation method is a mapping function with the limits within the range of the HU scale, the non-monotonous dependence observed in Fig. 17 is not seen in Fig. 19.

4.2 Analysis of Sources to the pCT Error

Here, the sources that contribute to the finite MAE between the generated pCT and the rCT are investigated. In general, the MAE has two main contributions, one from the imperfect fitting of the average CT number $\overline{CT}_{i,j}$ as a function of the MRI bin numbers (i, j) with equation (7), and the other from the intrinsic fluctuation or spread of the CT values at a given MRI bin numbers (i, j) around the mean value $\overline{CT}_{i,j}$, including individual differences among patients.

To investigate the differences of pCT and rCT numbers, dError is determined for each voxel position by the following equation:

$$dError_k = pCT_k - rCT_k, \tag{14}$$

where pCT_k is the predicted CT number for voxel k, and rCT_k is the reference CT number for voxel k.

Figure 20 presents a comparison of rCT and pCT for the same axial slice, together with the dError contour map. The figure shows voxels with dError $<$ -500 or dError $>$ 500 are located mainly at the boundary of the soft-bone tissue interface (the mixed region) and within the bony region where the cortical and the cancellous tissues are neighboring; this is consistent with the MAE values in Table 3. This also shows that there is still an alignment issue between the pCT and the rCT after image registration. Another area with high difference (dError $>$ 500) between rCT and pCT has low intensity (dark spot) on Fig. 20A, where a pocket of air is located within the bowel. This is not seen in Fig. 20B and is attributed to the extended time between acquiring the MR and the CT images.

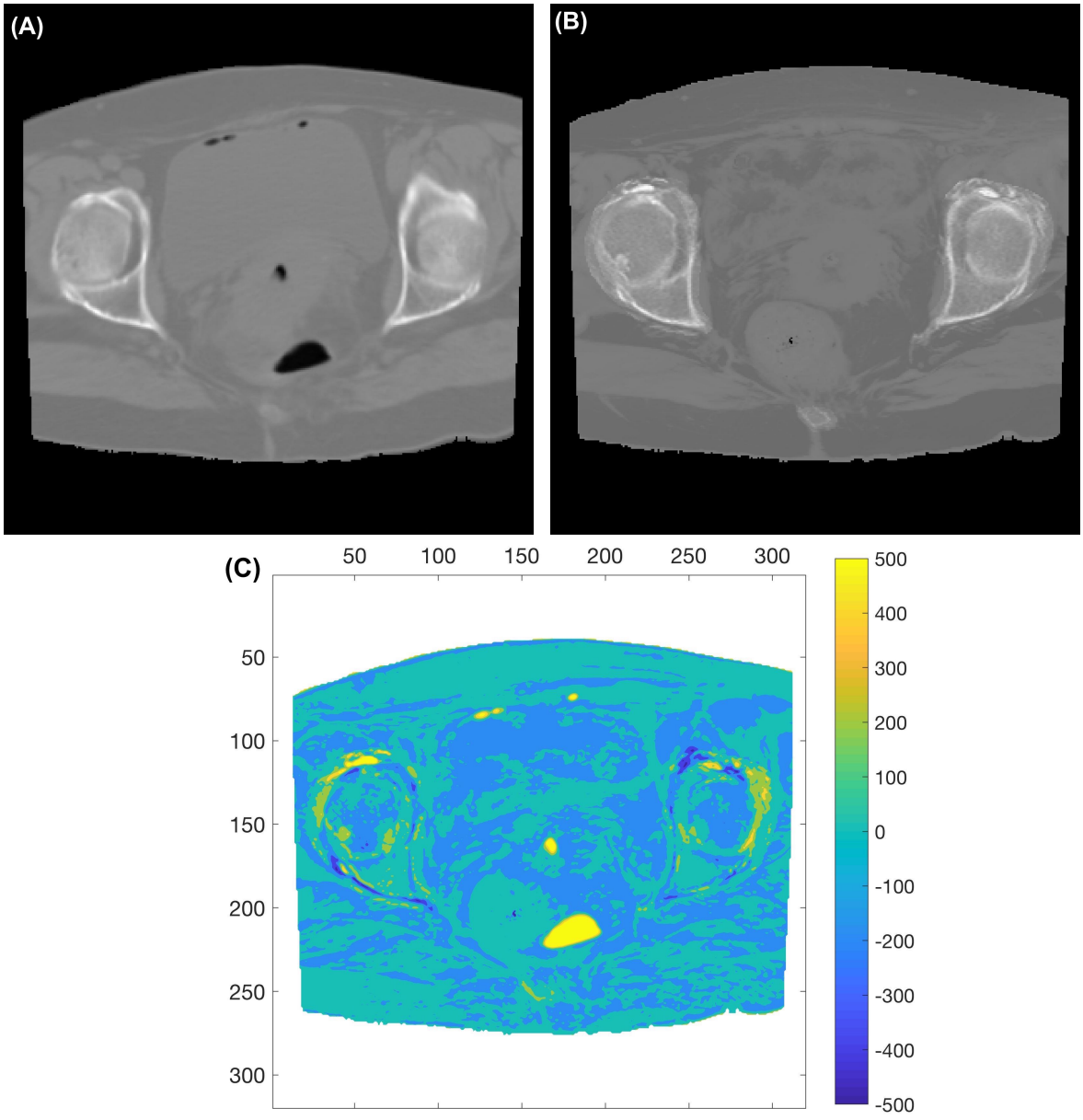

Figure 20: Axial slice of (A) rCT, (B) pCT, and (C) dError contour map.

The mean error (ME) values are evaluated to determine if the overall mapping function is negatively or positively biased by the following equation

$$ME = \frac{1}{N}\sum_{k=1}^{N}(pCT_k - rCT_k), \tag{15}$$

where N is the total number of body voxels (except the voxels from the excluded region) of the target patient, pCT_k and rCT_k denote respectively the value of the generated pCT and the (rCT) for voxel k. Table 8 presents the ME values for the overall generated pCT

	Mean Error (HU)			
	Overall	Soft Region	Bony Region	Mixed Region
Cycle1	15.8	5.5	69.1	52.6
Cycle2	5.3	4.6	-17.6	29.5
Cycle3	-19.1	-10.7	-61.9	-63.8
Cycle4	-2.5	-1.7	-1.2	-15.2
Cycle5	9.8	6.3	32.5	25.5
Cycle6	-4.9	-0.7	-14.6	-52.5
Average	0.7	0.5	1.0	-4.0
± SD	±12.4	±6.4	±45.2	±47.4

Table 8: ME values between pCT and rCT for the overall patient volume and for each segmented region of each LOOCV cycle and the average values for all six cycles.

image volume. The ME values are 0.7 ± 12.4 HU overall, 0.5 ± 6.4 HU for soft region, 1.0 ± 45.2 HU for bony region, and -4.0 ± 47.4 HU for mixed region. The values show that the mapping function has no general bias on average for all cycles, however, individually the cycles have large varying ME values ranging from 6.3 to -10.7 HU, -61.9 to 69.1 HU, and -52.5 to 52.6 HU for the soft, the bony and the mixed region, respectively. This is possibly due to individual differences between patients and the large spread of CT number for the same MR_1 and MR_2 bin indices.

Instead of mean differences another aspect to look at is the root-mean-squared (RMS) difference between pCT and rCT:

$$\sigma_{pCT} = \sqrt{\frac{1}{N}\sum_{k=1}^{N}(pCT_k - rCT_k)^2}\ , \tag{16}$$

where N is the total number of voxels in the imaged volume (not including the voxels in the excluded region), and k is voxel index. When evaluated for each region, N in

the above equation then represents the total number of body voxels in that region in the imaged volume. The σ_{pCT} values are presented in Table 9. Note that the σ_{pCT} is

	σ_{pCT} (HU)			
	Overall	Soft Region	Bony Region	Mixed Region
Cycle1	86.1	48.4	160.0	188.1
Cycle2	80.7	46.0	133.7	180.6
Cycle3	79.4	41.1	142.5	209.0
Cycle4	80.4	43.6	147.8	216.5
Cycle5	69.0	39.3	128.1	179.3
Cycle6	70.0	41.7	118.2	192.7
Average	77.6	43.3	138.4	194.4
± SD	±6.7	±3.4	±14.9	±15.3

Table 9: σ_{pCT} values between pCT and rCT for the overall patient volume and for each segmented region of each LOOCV cycle and their average values for all six cycles.

always higher than (or equal to) the corresponding unweighted (i.e. raw) MAE value, which can be verified by comparing Tables 3 and 9. As expected, the largest differences are observed for bony and mixed regions, consistent with the fact that their unweighted MAE values shown in Table 3 are higher than that of the soft region.

To evaluate the goodness of fit of the polynomial equation (7), the mean error, mean absolute error and RMS differences between the predicted $HU(S_1, S_2)$ from equation (7) and the averaged CT number $\overline{CT}_{i,j}$ in the reference-CT training data for each segmented region are determined:

$$ME_{fit} = \frac{1}{N}\sum_{i,j=1}(\overline{CT}_{i,j} - pCT_{i,j})N_{i,j}, \tag{17}$$

$$MAE_{fit} = \frac{1}{N}\sum_{i,j=1}|\overline{CT}_{i,j} - pCT_{i,j}|N_{i,j}, \tag{18}$$

$$\sigma_{fit} = \sqrt{\frac{1}{N}\sum_{i,j=1}\left(\overline{CT}_{i,j} - pCT_{i,j}\right)^2 N_{i,j}}, \tag{19}$$

where $N = \sum_{i,j=1}^{Nbin} N_{i,j}$ gives the total number of voxels in the imaged volume for that

region. In the above, $pCT_{i,j} = HU(S_1, S_2)$ is the predicted CT number for the (i, j) MRI bin, where S_1 and S_2 here represents the central intensity value of the i-th MR_1 bin and the j-th MR_2 bin, respectively.

	ME_{fit} (HU)			MAE_{fit} (HU)			σ_{fit} (HU)		
	Soft	Bony	Mixed	Soft	Bony	Mixed	Soft	Bony	Mixed
Cycle1	-0.003	0.004	0.053	2.0	10.4	16.6	5.3	21.5	31.6
Cycle2	-0.002	0.002	0.055	2.1	11.0	17.3	4.5	22.6	33.3
Cycle3	-0.003	-0.018	0.060	2.1	10.4	16.0	5.4	20.0	31.3
Cycle4	-0.004	0.026	0.028	2.1	10.5	15.8	5.5	21.4	29.8
Cycle5	-0.006	0.073	0.062	2.1	11.3	16.5	5.7	23.2	32.4
Cycle6	-0.004	-0.073	0.031	2.1	10.9	15.9	5.4	23.3	31.7
Average	-0.004	0.005	0.048	2.1	10.8	16.3	5.3	22.0	31.7
± SD	±0.002	±0.048	±0.015	±0.0	±0.4	±0.6	±0.4	±1.2	±1.3

Table 10: ME_{fit}, MAE_{fit} and σ_{fit} values for the overall patient volume, for all segmented regions of each LOOCV cycle, and their average values for all six cycles. ME_{fit} values x10

Table 10 presents the ME_{fit}, MAE_{fit}, and σ_{fit} values for each regions, each cycles and their average values. On average for all cycles, ME_{fit} is (-0.4 ± 0.2) x10^{-2} HU, (-0.5 ± 0.5) x10^{-2} HU, and (-4.8 ± 1.5) x10^{-2} HU for the soft, the bony and the mixed region, respectively. The values for ME_{fit} in Table 10 show that for all cycles and regions ME_{fit} values are close to 0, proving that each region's polynomial fit function is unbiased and overall closely resembles the $\overline{CT}_{i,j}$ distribution, which is observed in Fig. 9. The MAE_{fit} as well as σ_{fit} values show that the fit is much better for the soft region compared to the other two regions.

Figure 21 displays MAE_{fit}, i.e., the absolute difference between $\overline{CT}_{i,j}$ and $pCT_{i,j}$ values on the MR_1-MR_2 bin indices plane. It confirms the observation from Table 10 that overall the fit is much better for the soft region. Note that in Fig. 21 the areas of high (> 400) MAE_{fit} values closely match the edges of the data distribution before bin filling for each region (as shown in Fig. 6).

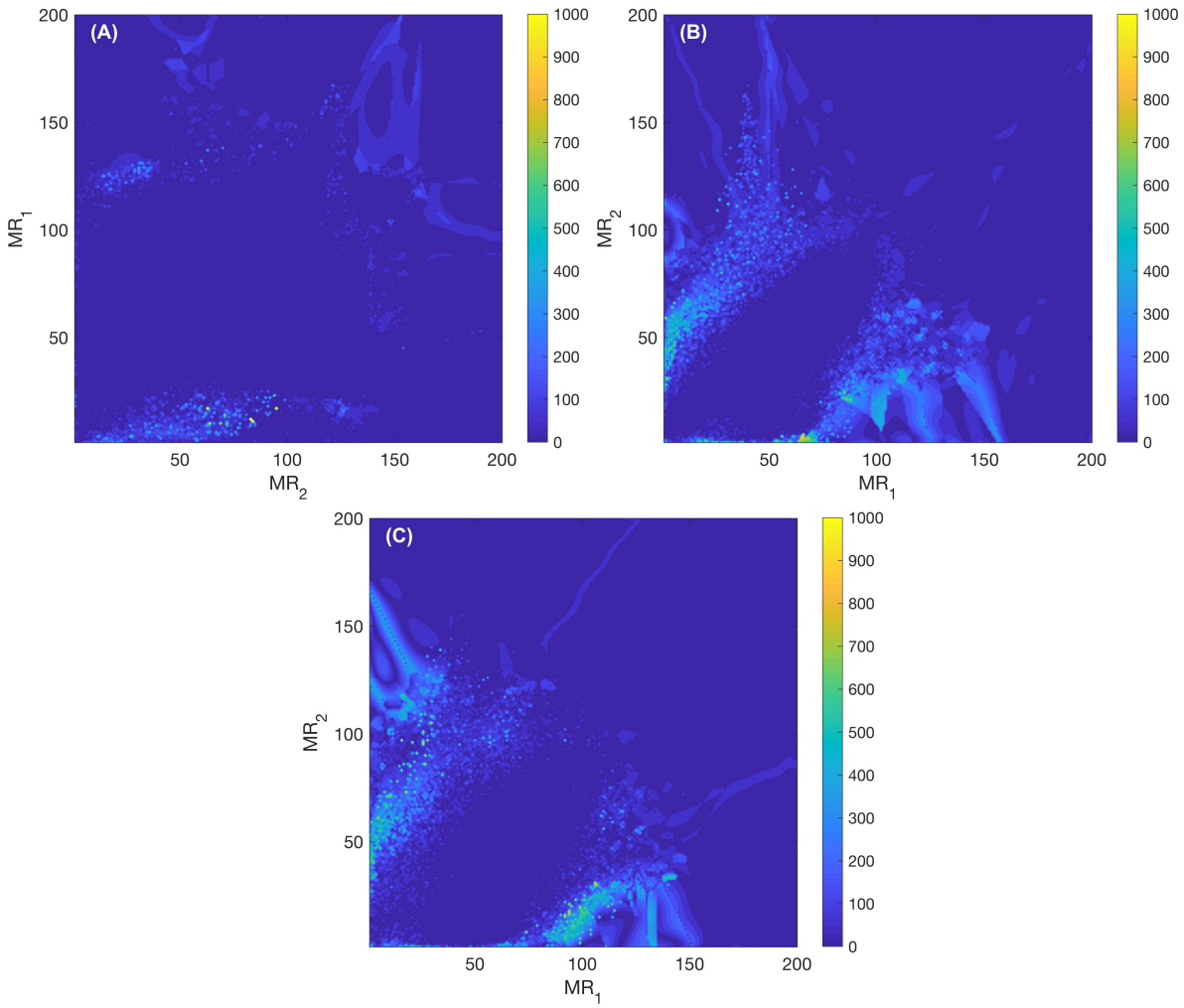

Figure 21: MAE_{fit} values are plotted on the MR_1-MR_2 plane for (A) soft, (B) bone, and (C) mixed region.

Another contribution to the MAE of the generated pCT comes from the fact that voxels with the same MR_1 and MR_2 bin numbers (i, j) do not have exactly the same CT number, although they average to the mean value $\overline{CT}_{i,j}$. For this, the mean absolute error and the RMS difference between individual voxel's rCT number and the average

value $\overline{CT}_{i,j}$ at the same MRI bin (i,j) are calculated for each region as

$$MAE_{rCT} = \frac{1}{N}\sum_{i,j=1}^{Nbin}\sum_{k=1}^{N_{i,j}}|rCT_k - \overline{CT}_{i,j}|, \quad (20)$$

$$\sigma_{rCT} = \sqrt{\frac{1}{N}\sum_{i,j=1}^{N_{i,j}}\sum_{k=1}^{}\left(rCT_k - \overline{CT}_{i,j}\right)^2}, \quad (21)$$

where N = $\sum_{i,j=1}^{Nbin} N_{i,j}$, and k is voxel index within the MRI bin (i,j). As shown in Table 11, the values for the bony region and the mixed region are much higher than that for the soft region, similar to Table 9. Comparing the average MAE_{rCT} value in Table 11 to the raw average MAE value Table 3, we see that their values are close to each other and both are much higher than the MAE_{fit} values in Table 10. Therefore, the error of pCT is mostly due to the intrinsic fluctuation of the CT numbers around the mean value in the same MR_1-MR_2 bin, not much due to the fitting function.

	MAE_{rCT} (HU)			σ_{rCT} (HU)		
	Soft Region	Bony Region	Mixed Region	Soft Region	Bony Region	Mixed Region
Cycle1	23.4	95.3	138.0	40.2	128.4	187.5
Cycle2	23.7	97.6	141.3	40.3	132.5	190.6
Cycle3	23.7	97.6	133.3	41.4	131.9	183.6
Cycle4	24.1	96.8	133.3	41.0	129.9	182.7
Cycle5	23.6	98.8	138.1	42.5	134.4	189.3
Cycle6	23.9	100.3	135.1	41.2	135.3	186.8
Average	23.7	97.7	136.5	41.1	132.1	186.7
± SD	± 0.2	± 1.7	± 3.2	± 0.8	± 2.6	± 3.1

Table 11: MAE_{rCT} and σ_{rCT} values for the spread of CT numbers at the same MRI bin for the overall patient volume, for all segmented regions of each LOOCV cycle, and their average values for all six cycles.

The σ_{rCT} values on the MR_1-MR_2 bin indices plane are presented in Fig. 22. The figure shows small CT number fluctuation (< 50 HU) from the overall soft region, whereas for the bone and mixed region high fluctuation (> 250 HU) is seen for almost the entire

area of the data distribution.

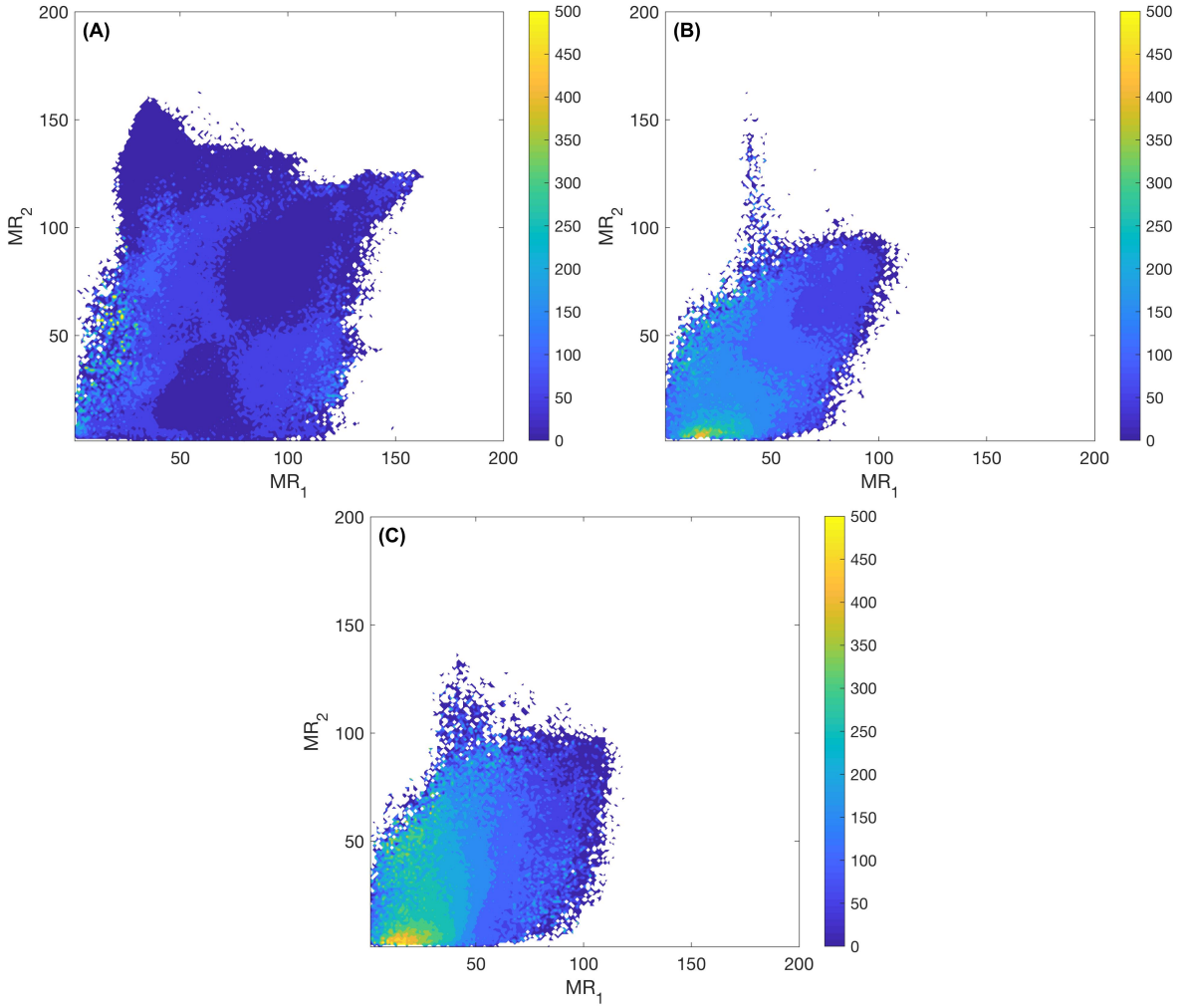

Figure 22: σ_{rCT} values are plotted on the MR_1-MR_2 plane for (A) soft, (B) bone, and (C) mixed region.

It is also observed that the MAE_{rCT} or σ_{rCT} values are much higher than the corresponding MAE_{fit} or σ_{fit} values for the same region. Furthermore, if the uncertainties from these two sources were independent, one would expect the following relation for each region:

$$\sigma_{pCT}^2 = \sigma_{rCT}^2 + \sigma_{fit}^2. \tag{22}$$

From Tables 9, 10 and 11, the average σ_{pCT} value of each region is indeed higher than the corresponding average value of either σ_{rCT} or σ_{fit}, and the above relation is approximately true quantitatively. We use equation (22) to calculate the expected σ_{pCT} from σ_{fit} and σ_{rCT} values in Tables 10 and 11, respectively. To compare the σ_{pCT} and its corresponding calculated value, $\Delta\sigma$ is determined by

$$\Delta\sigma = \sqrt{\sigma_{rCT}^2 + \sigma_{fit}^2} - \sigma_{pCT}, \tag{23}$$

where σ_{pCT} is from Table 9. These values are shown in Table 12.

	Soft		Bone		Mixed	
	$\sqrt{\sigma_{rCT}^2 + \sigma_{Fit}^2}$	$\Delta\sigma$	$\sqrt{\sigma_{rCT}^2 + \sigma_{fit}^2}$	$\Delta\sigma$	$\sqrt{\sigma_{rCT}^2 + \sigma_{fit}^2}$	$\Delta\sigma$
Cycle1	40.6	-7.9	130.2	-29.8	190.1	2.0
Cycle2	40.5	-5.5	134.4	0.7	193.5	12.9
Cycle3	41.7	0.6	133.4	-9.1	186.2	-22.8
Cycle4	41.3	-2.3	131.6	-16.2	185.1	-31.4
Cycle5	42.9	3.6	136.4	8.3	192.0	12.7
Cycle6	41.6	-0.1	137.3	19.2	189.4	-3.3
Average	41.4	-1.9	133.9	-4.5	189.4	-5.0

Table 12: Calculated σ_{pCT} values and the difference from the corresponding actual σ_{pCT} value.

Similar features can also be observed for the MAE values from Tables 3, 10 and 11, as we may expect the following relation:

$$MAE_{calc}^2 \approx MAE_{rCT}^2 + MAE_{fit}^2. \tag{24}$$

Equation (24) presents an approximate method to estimate MAE from MAE_{fit} and MAE_{rCT} values. To compare the estimated MAE and actual values, ΔMAE is determined by

$$\Delta MAE = MAE_{calc} - MAE, \tag{25}$$

where MAE is from Table 3. These values are shown in Table 13. The average (raw) MAE value of each region is higher than the corresponding average value of either MAE_{rCT} or MAE_{fit}, with $MAE_{rCT} \gg MAE_{fit}$, and the relation $MAE^2 \approx MAE^2_{rCT} + MAE^2_{fit}$ holds approximately.

	Soft		Bone		Mixed	
	MAE_{calc}	ΔMAE	MAE_{calc}	ΔMAE	MAE_{calc}	ΔMAE
Cycle1	23.5	-2.3	95.8	-22.7	138.9	0.6
Cycle2	23.8	-1.8	98.2	-1.9	142.4	8.0
Cycle3	23.8	-1.0	98.2	-5.8	134.3	-17.6
Cycle4	24.1	1.1	97.4	-8.3	134.2	-22.8
Cycle5	23.7	-0.8	99.4	-0.3	139.1	3.3
Cycle6	24.0	0.1	100.9	12.9	136.1	-7.6
Average	23.8	0.8	98.3	-4.4	137.5	-6.0

Table 13: MAE_{calc} values and difference from the corresponding actual MAE value.

Therefore, we conclude that the intrinsic fluctuation of the rCT numbers for voxels with similar MRI intensity values, not the fitting procedure from the regression analysis, is the dominant source of the uncertainty in the generated pCT images.

4.3 Future Work

One future development of this research project will be on improving the segmentation of the bony, soft and mixed regions in this thesis. The implementation of auto-segmentation [63, 64] is more desirable for reproducibility and efficiency. Possible implementation methods are by modifying an edge detection algorithm or intensity thresholding, which is possible by commercially available products. It may also be helpful to increase the number of segmented regions.

Another future development of this research project will be the inclusion of multiple (more than two) MRI sequence parameters. The polynomial prediction model can be

easily modified to the following form:

$$\begin{aligned} HU(S_1, \ldots, S_m) &= \sum_{i_1, \ldots, i_m=0}^{i_1+\cdots+i_m \leq n} \left(c_{i_1, \ldots, i_m} S_1^{i_1} \ \ldots \ S_m^{i_m} \right) \\ &= c_{0, \ldots, 0} + c_{1,0, \ldots, 0} S_1 + \ \ldots \ + c_{0, \ldots, 0,1} S_m + \ \ldots \ + c_{1,0, \ldots, 0,1} S_1 S_m + \ \ldots \\ &\quad + c_{N,0, \ldots, 0} \, S_1^N + \ \ldots \ + c_{0, \ldots, 0,N} \, S_m^N, \end{aligned} \tag{26}$$

where n is the highest polynomial degree, $HU(S_1, \ldots, S_m)$ is the dependent variable of the mapping function, S_1 is the intensity value from the first set of MRI scan, S_m is the intensity value from the m_{th} set of MRI scan, S_1 and S_m are both independent variables, i_1 is the exponent for S_1, i_m is the exponent for S_m, and $c_{i_1, \ldots, i_m}$ is the fitting coefficient. In addition to increasing the number of independent variables, determining or developing the optimal MR sequence parameters for near-orthogonal tissue contrast to use in acquiring the MRI scans could greatly increase the accuracy of our prediction model and thus the pCT accuracy.

In addition, a future study for this research project could be to extend the prediction model to other relevant anatomical locations (lung or head & neck). The optimal MRI sequence parameters may be different and thus need to be determined due to the different composition of tissues.

Finally, a patent application has been filed on our method of establishing and applying the polynomial prediction method as described in this thesis project.

5 Conclusions

This thesis work has developed a voxel-based method that uses two MRI sets to create the pCT image. The two MRI sets are acquired with different MRI sequence parameters. The anatomical structures of the acquired images are segmented into regions including the bony region, soft region, and mixed region; and then a regression analysis is used to determine the two-variable high-degree polynomial function for each region. A high polynomial degree, $n \geq 20$, and a high number of MRI bins, $Nbin \geq 100$, are preferred in order to accurately reproduce the relationship between the voxel's two MRI intensity values and its CT number without significant computation burden. The method can be easily extended to more than two MRI sets to create the pCT image.

Using data from six patients, a high accuracy is obtained in predicting the CT numbers, with the pCT image volume having an average MAE of 40.3 $\pm$ 3.0 HU using the LOOCV method. This is better than previous results from voxel-based methods or most atlas-based methods and comparable to another study that used a more complicated method. That study [59], which uses a hybrid method that combines a statistical decomposition algorithm to determine the most probable CT representation and a non-linear warping procedure to align template MRI database to the target MRI, has an average MAE of 36.5 HU. Our dosimetric calculations of an example treatment plan are performed using the pCT and then compared with those using the rCT. An average passing rate of more than 95% is obtained in point-to-point dose comparisons between the two simulated treatment plans. The largest deviations are found at the bone-tissue interface, indicating that misalignments between the acquired MRI and CT images are a significant contribution to MAE in our study. This will not be an issue when applied to MRI-only RT. An automated segmentation method, better alignments between the MRI and CT images, and optimization of the MRI sequence parameters will minimize

the deviations found at the bone-tissue interface and further improve the accuracy of our method.

In addition, our analysis into the sources of pCT error first shows that the average ME_{fit} values for the soft, the bony and the mixed region are fairly close to 0, indicating that the fitting function is unbiased. Next, the average MAE_{rCT} values are significantly higher than average MAE_{fit} values for each (soft, bony, and mixed) region. The same is true when comparing σ_{rCT} values to σ_{fit} values for soft, bony, and mixed region. MAE_{rCT} and σ_{rCT} are estimates on the fluctuation of rCT number around the mean rCT number at a MRI bin (i, j). MAE_{fit} and σ_{fit} are estimates on the goodness of the fitting function. The significantly higher MAE_{rCT} and σ_{rCT} values indicate that the intrinsic fluctuation is the dominant source of error rather than the fitting procedure for the regression analysis.

Overall, our proposed pCT generation method using multiple MRI sets with anatomical segmentation shows promising results and provides a convenient tool for MRI-only radiation treatment planning.

References

[1] M. Karlsson, M. G. Karlsson, T. Nyholm, C. Amies, and B. Zackrisson, "Dedicated magnetic resonance imaging in the radiotherapy clinic," *International Journal of Radiation Oncology* Biology* Physics*, vol. 74, no. 2, pp. 644–651, 2009.

[2] T. Nyholm, M. Nyberg, M. G. Karlsson, and M. Karlsson, "Systematisation of spatial uncertainties for comparison between a MR and a CT-based radiotherapy workflow for prostate treatments," *Radiation Oncology*, vol. 4, no. 1, p. 54, 2009.

[3] I. Barillot and A. Reynaud-Bougnoux, "The use of MRI in planning radiotherapy for gynaecological tumours," *Cancer Imaging*, vol. 6, no. 1, p. 100, 2006.

[4] J. A. Dowling, J. Lambert, J. Parker, O. Salvado, J. Fripp, A. Capp, C. Wratten, J. W. Denham, and P. B. Greer, "An atlas-based electron density mapping method for magnetic resonance imaging (MRI)-alone treatment planning and adaptive MRI-based prostate radiation therapy," *International Journal of Radiation Oncology* Biology* Physics*, vol. 83, no. 1, pp. 5–11, 2012.

[5] M. Kapanen and M. Tenhunen, "T1/T2*-weighted MRI provides clinically relevant pseudo-CT density data for the pelvic bones in MRI-only based radiotherapy treatment planning," *Acta Oncologica*, vol. 52, no. 3, pp. 612–618, 2013.

[6] W. Skrzyński, S. Zielińska-Dąbrowska, M. Wachowicz, W. Ślusarczyk-Kacprzyk, P. F. Kukołowicz, and W. Bulski, "Computed tomography as a source of electron density information for radiation treatment planning," *Strahlentherapie und Onkologie*, vol. 186, no. 6, pp. 327–333, 2010.

[7] M. K. Bucci, A. Bevan, and M. Roach III, "Advances in radiation therapy: conventional to 3D, to IMRT, to 4D, and beyond," *CA: A Cancer Journal for Clinicians*, vol. 55, no. 2, pp. 117–134, 2005.

[8] F. H. Attix, *Introduction to radiological physics and radiation dosimetry*. John Wiley & Sons, 2008.

[9] J. T. Bushberg and J. M. Boone, *The essential physics of medical imaging*. Lippincott Williams & Wilkins, 2011.

[10] W. Nitz and P. Reimer, "Contrast mechanisms in MR imaging," *European radiology*, vol. 9, no. 6, pp. 1032–1046, 1999.

[11] E. Berry and A. J. Bulpitt, *Fundamentals of MRI: an interactive learning approach*. CRC Press, 2008.

[12] B. N. Weissman, *Imaging of arthritis and metabolic bone disease*. Elsevier Health Sciences, 2009.

[13] T. Kron, D. Eyles, L. J. Schreiner, and J. Battista, "Magnetic resonance imaging for adaptive cobalt tomotherapy: A proposal," *Journal of Medical Physics*, vol. 31, no. 4, p. 242, 2006.

[14] B. Fallone, M. Carlone, B. Murray, S. Rathee, T. Stanescu, S. Steciw, K. Wachowicz, and C. Kirkby, "TU-C-M100F-01: development of a linac-MRI system for real-time ART," *Medical Physics*, vol. 34, no. 6Part17, pp. 2547–2547, 2007.

[15] J. J. Lagendijk, B. W. Raaymakers, A. J. Raaijmakers, J. Overweg, K. J. Brown, E. M. Kerkhof, R. W. van der Put, B. Hårdemark, M. van Vulpen, and U. A. van der Heide, "MRI/linac integration," *Radiotherapy and Oncology*, vol. 86, no. 1, pp. 25–29, 2008.

[16] S. Mutic and J. F. Dempsey, "The ViewRay system: magnetic resonance–guided and controlled radiotherapy," in *Seminars in Radiation Oncology*, vol. 24, pp. 196–199, Elsevier, 2014.

[17] B. Raaymakers, J. Lagendijk, J. Overweg, J. Kok, A. Raaijmakers, E. Kerkhof, R. Van der Put, I. Meijsing, S. Crijns, F. Benedosso, *et al.*, "Integrating a 1.5 T MRI scanner with a 6 MV accelerator: proof of concept," *Physics in Medicine & Biology*, vol. 54, no. 12, p. N229, 2009.

[18] B. Raaymakers, I. Jürgenliemk-Schulz, G. Bol, M. Glitzner, A. Kotte, B. van Asselen, J. de Boer, J. Bluemink, S. Hackett, M. Moerland, *et al.*, "First patients treated with a 1.5 T MRI-linac: clinical proof of concept of a high-precision, high-field MRI guided radiotherapy treatment," *Physics in Medicine & Biology*, vol. 62, no. 23, p. L41, 2017.

[19] B. J. Pichler, A. Kolb, T. Nägele, and H.-P. Schlemmer, "PET/MRI: paving the way for the next generation of clinical multimodality imaging applications," *Journal of Nuclear Medicine*, vol. 51, no. 3, pp. 333–336, 2010.

[20] H. Jadvar and P. M. Colletti, "Competitive advantage of PET/MRI," *European Journal of Radiology*, vol. 83, no. 1, pp. 84–94, 2014.

[21] P. Metcalfe, G. Liney, L. Holloway, A. Walker, M. Barton, G. Delaney, S. Vinod, and W. Tome, "The potential for an enhanced role for MRI in radiation-therapy treatment planning," *Technology in Cancer Research & Treatment*, vol. 12, no. 5, pp. 429–446, 2013.

[22] B. Emami, A. Sethi, and G. J. Petruzzelli, "Influence of MRI on target volume delineation and IMRT planning in nasopharyngeal carcinoma," *International Journal of Radiation Oncology* Biology* Physics*, vol. 57, no. 2, pp. 481–488, 2003.

[23] S. Hanvey, A. Sadozye, M. McJury, M. Glegg, and J. Foster, "The influence of MRI scan position on image registration accuracy, target delineation and calculated dose in prostatic radiotherapy," *The British Journal of Radiology*, vol. 85, no. 1020, pp. 1256–1262, 2012.

[24] V. S. Khoo, D. P. Dearnaley, D. J. Finnigan, A. Padhani, S. F. Tanner, and M. O. Leach, "Magnetic resonance imaging (MRI): considerations and applications in radiotherapy treatment planning," *Radiotherapy and Oncology*, vol. 42, no. 1, pp. 1–15, 1997.

[25] M. Hofmann, B. Pichler, B. Schölkopf, and T. Beyer, "Towards quantitative PET/MRI: a review of MR-based attenuation correction techniques," *European Journal of Nuclear Medicine and Molecular Imaging*, vol. 36, no. 1, pp. 93–104, 2009.

[26] I. Bezrukov, F. Mantlik, H. Schmidt, B. Schölkopf, and B. J. Pichler, "MR-based PET attenuation correction for PET/MR imaging," in *Seminars in Nuclear Medicine*, vol. 43, pp. 45–59, Elsevier, 2013.

[27] D. Visvikis, F. Monnier, J. Bert, M. Hatt, and H. Fayad, "PET/MR attenuation correction: where have we come from and where are we going?," *European Journal of Nuclear Medicine and Molecular Imaging*, vol. 41, no. 6, pp. 1172–1175, 2014.

[28] T. Nyholm and J. Jonsson, "Counterpoint: opportunities and challenges of a magnetic resonance imaging–only radiotherapy work flow," in *Seminars in Radiation Oncology*, vol. 24, pp. 175–180, Elsevier, 2014.

[29] J. M. Edmund and T. Nyholm, "A review of substitute CT generation for MRI-only radiation therapy," *Radiation Oncology*, vol. 12, no. 1, p. 28, 2017.

[30] B. Wafa and A. Moussaoui, "A review on methods to estimate a CT from MRI data in the context of MRI-alone RT," *Medical Technologies Journal*, vol. 2, no. 1, pp. 150–178, 2018.

[31] M.-L. Montandon and H. Zaidi, "Atlas-guided non-uniform attenuation correction in cerebral 3D PET imaging," *Neuroimage*, vol. 25, no. 1, pp. 278–286, 2005.

[32] M. Hofmann, F. Steinke, V. Scheel, G. Charpiat, J. Farquhar, P. Aschoff, M. Brady, B. Schölkopf, and B. J. Pichler, "MRI-based attenuation correction for PET/MRI: a novel approach combining pattern recognition and atlas registration," *Journal of Nuclear Medicine*, vol. 49, no. 11, pp. 1875–1883, 2008.

[33] M. Hofmann, I. Bezrukov, F. Mantlik, P. Aschoff, F. Steinke, T. Beyer, B. J. Pichler, and B. Schölkopf, "MRI-based attenuation correction for whole-body PET/MRI: quantitative evaluation of segmentation-and atlas-based methods," *Journal of Nuclear Medicine*, vol. 52, no. 9, pp. 1392–1399, 2011.

[34] J. Dowling, J. Lambert, J. Parker, P. B. Greer, J. Fripp, J. Denham, S. Ourselin, and O. Salvado, "Automatic MRI atlas-based external beam radiation therapy treatment planning for prostate cancer," in *International Workshop on Prostate Cancer Imaging*, pp. 25–33, Springer, 2010.

[35] S. Klein, U. A. Van Der Heide, I. M. Lips, M. Van Vulpen, M. Staring, and J. P. Pluim, "Automatic segmentation of the prostate in 3D MR images by atlas matching using localized mutual information," *Medical Physics*, vol. 35, no. 4, pp. 1407–1417, 2008.

[36] D. Andreasen, K. Van Leemput, R. H. Hansen, J. A. Andersen, and J. M. Edmund, "Patch-based generation of a pseudo CT from conventional MRI sequences for MRI-only radiotherapy of the brain," *Medical Physics*, vol. 42, no. 4, pp. 1596–1605, 2015.

[37] D. Andreasen, K. Van Leemput, and J. M. Edmund, "A patch-based pseudo-CT approach for MRI-only radiotherapy in the pelvis," *Medical Physics*, vol. 43, no. 8Part1, pp. 4742–4752, 2016.

[38] J. Uh, T. E. Merchant, Y. Li, X. Li, and C. Hua, "MRI-based treatment planning with pseudo CT generated through atlas registration," *Medical Physics*, vol. 41, no. 5, 2014.

[39] J. Degen and M. P. Heinrich, "Multi-atlas based pseudo-CT synthesis using multimodal image registration and local atlas fusion strategies," in *Proceedings of the IEEE Conference on Computer Vision and Pattern Recognition Workshops*, pp. 160–168, 2016.

[40] B. Demol, C. Boydev, J. Korhonen, and N. Reynaert, "Dosimetric characterization of MRI-only treatment planning for brain tumors in atlas-based pseudo-ct images generated from standard T1-weighted MR images," *Medical Physics*, vol. 43, no. 12, pp. 6557–6568, 2016.

[41] J. Sjölund, D. Forsberg, M. Andersson, and H. Knutsson, "Generating patient specific pseudo-CT of the head from MR using atlas-based regression," *Physics in Medicine & Biology*, vol. 60, no. 2, p. 825, 2015.

[42] H. Arabi, N. Koutsouvelis, M. Rouzaud, R. Miralbell, and H. Zaidi, "Atlas-guided generation of pseudo-CT images for MRI-only and hybrid PET–MRI-guided radiotherapy treatment planning," *Physics in Medicine & Biology*, vol. 61, no. 17, p. 6531, 2016.

[43] J. M. Edmund, H. M. Kjer, K. Van Leemput, R. H. Hansen, J. A. Andersen, and D. Andreasen, "A voxel-based investigation for MRI-only radiotherapy of the brain

using ultra short echo times," *Physics in Medicine & Biology*, vol. 59, no. 23, p. 7501, 2014.

[44] Y. K. Lee, M. Bollet, G. Charles-Edwards, M. A. Flower, M. O. Leach, H. McNair, E. Moore, C. Rowbottom, and S. Webb, "Radiotherapy treatment planning of prostate cancer using magnetic resonance imaging alone," *Radiotherapy and Oncology*, vol. 66, no. 2, pp. 203–216, 2003.

[45] A. Johansson, M. Karlsson, and T. Nyholm, "CT substitute derived from MRI sequences with ultrashort echo time," *Medical Physics*, vol. 38, no. 5, pp. 2708–2714, 2011.

[46] A. Johansson, A. Garpebring, M. Karlsson, T. Asklund, and T. Nyholm, "Improved quality of computed tomography substitute derived from magnetic resonance (MR) data by incorporation of spatial information–potential application for MR-only radiotherapy and attenuation correction in positron emission tomography," *Acta Oncologica*, vol. 52, no. 7, pp. 1369–1373, 2013.

[47] C. M. Rank, C. Tremmel, N. Hünemohr, A. M. Nagel, O. Jäkel, and S. Greilich, "MRI-based treatment plan simulation and adaptation for ion radiotherapy using a classification-based approach," *Radiation Oncology*, vol. 8, no. 1, p. 51, 2013.

[48] C. M. Rank, N. Hünemohr, A. M. Nagel, M. C. Röthke, O. Jäkel, and S. Greilich, "MRI-based simulation of treatment plans for ion radiotherapy in the brain region," *Radiotherapy and Oncology*, vol. 109, no. 3, pp. 414–418, 2013.

[49] S.-H. Hsu, Y. Cao, K. Huang, M. Feng, and J. M. Balter, "Investigation of a method for generating synthetic CT models from MRI scans of the head and neck for radiation therapy," *Physics in Medicine & Biology*, vol. 58, no. 23, p. 8419, 2013.

[50] J. Korhonen, M. Kapanen, J. Keyriläinen, T. Seppälä, and M. Tenhunen, "A dual model HU conversion from MRI intensity values within and outside of bone segment for MRI-based radiotherapy treatment planning of prostate cancer," *Medical Physics*, vol. 41, no. 1, 2014.

[51] J. Kim, C. Glide-Hurst, A. Doemer, N. Wen, B. Movsas, and I. J. Chetty, "Implementation of a novel algorithm for generating synthetic CT images from magnetic resonance imaging data sets for prostate cancer radiation therapy," *International Journal of Radiation Oncology* Biology* Physics*, vol. 91, no. 1, pp. 39–47, 2015.

[52] X. Han, "MR-based synthetic CT generation using a deep convolutional neural network method," *Medical Physics*, vol. 44, no. 4, pp. 1408–1419, 2017.

[53] M. Hirsch, M. Hofmann, F. Mantlik, B. J. Pichler, B. Schölkopf, and M. Habeck, "A blind deconvolution approach for pseudo CT prediction from MR image pairs," in *2012 19th IEEE International Conference on Image Processing*, pp. 2953–2956, IEEE, 2012.

[54] A. L. Chin, A. Lin, S. Anamalayil, and B.-K. K. Teo, "Feasibility and limitations of bulk density assignment in MRI for head and neck IMRT treatment planning," *Journal of Applied Clinical Medical Physics*, vol. 15, no. 5, pp. 100–111, 2014.

[55] H. Yu, C. Caldwell, J. Balogh, and K. Mah, "Toward magnetic resonance–only simulation: segmentation of bone in MR for radiation therapy verification of the head," *International Journal of Radiation Oncology* Biology* Physics*, vol. 89, no. 3, pp. 649–657, 2014.

[56] L. Zhong, L. Lin, Z. Lu, Y. Wu, Z. Lu, M. Huang, W. Yang, and Q. Feng, "Predict CT image from MRI data using KNN-regression with learned local descriptors," in

2016 IEEE 13th International Symposium on Biomedical Imaging (ISBI), pp. 743–746, IEEE, 2016.

[57] J. Teuho, J. Linden, J. Johansson, J. Tuisku, T. Tuokkola, and M. Teräs, "Tissue probability-based attenuation correction for brain PET/MR by using SPM8," *IEEE Transactions on Nuclear Science*, vol. 63, no. 5, pp. 2452–2463, 2016.

[58] M. S. R. Gudur, W. Hara, Q.-T. Le, L. Wang, L. Xing, and R. Li, "A unifying probabilistic bayesian approach to derive electron density from MRI for radiation therapy treatment planning," *Physics in Medicine & Biology*, vol. 59, no. 21, p. 6595, 2014.

[59] C. Siversson, F. Nordström, T. Nilsson, T. Nyholm, J. Jonsson, A. Gunnlaugsson, and L. E. Olsson, "MRI only prostate radiotherapy planning using the statistical decomposition algorithm," *Medical Physics*, vol. 42, no. 10, pp. 6090–6097, 2015.

[60] V. Keereman, Y. Fierens, T. Broux, Y. De Deene, M. Lonneux, and S. Vandenberghe, "MRI-based attenuation correction for PET/MRI using ultrashort echo time sequences," *Journal of Nuclear Medicine*, vol. 51, no. 5, p. 812, 2010.

[61] Y. Berker, J. Franke, A. Salomon, M. Palmowski, H. C. Donker, Y. Temur, F. M. Mottaghy, C. Kuhl, D. Izquierdo-Garcia, Z. A. Fayad, *et al.*, "Mri-based attenuation correction for hybrid PET/MRI systems: a 4-class tissue segmentation technique using a combined ultrashort-echo-time/dixon MRI sequence," *Journal of Nuclear Medicine*, vol. 53, no. 5, p. 796, 2012.

[62] C. Croarkin, P. Tobias, J. Filliben, B. Hembree, W. Guthrie, *et al.*, "NIST/SEMATECH e-handbook of statistical methods," *NIST/SEMATECH, July. Available online: http://www.itl.nist.gov/div898/handbook*, 2006.

[63] D. Pasquier, T. Lacornerie, M. Vermandel, J. Rousseau, E. Lartigau, and N. Betrouni, "Automatic segmentation of pelvic structures from magnetic resonance images for prostate cancer radiotherapy," *International Journal of Radiation Oncology* Biology* Physics*, vol. 68, no. 2, pp. 592–600, 2007.

[64] H. Seim, D. Kainmueller, M. Heller, H. Lamecker, S. Zachow, and H.-C. Hege, "Automatic segmentation of the pelvic bones from CT data based on a statistical shape model.," *VCBM*, vol. 2008, pp. 93–100, 2008.

[65] M. E. Korsholm, L. W. Waring, and J. M. Edmund, "A criterion for the reliable use of MRI-only radiotherapy," *Radiation Oncology*, vol. 9, no. 1, p. 16, 2014.

[66] J. H. Jonsson, M. G. Karlsson, M. Karlsson, and T. Nyholm, "Treatment planning using MRI data: an analysis of the dose calculation accuracy for different treatment regions," *Radiation Oncology*, vol. 5, no. 1, p. 62, 2010.

[67] P. B. Greer, J. A. Dowling, J. A. Lambert, J. Fripp, J. Parker, J. W. Denham, C. Wratten, A. Capp, and O. Salvado, "A magnetic resonance imaging-based workflow for planning radiation therapy for prostate cancer," *Medical Journal of Australia*, vol. 194, no. 4, p. S24, 2011.

[68] Y. Lei, H. Shu, S. Tian, T. Wang, T. Liu, H. Mao, H. Shim, W. Curran, and X. Yang, "Pseudo CT estimation using patch-based joint dictionary learning," in *2018 40th Annual International Conference of the IEEE Engineering in Medicine and Biology Society (EMBC)*, pp. 5150–5153, IEEE, 2018.

[69] A. Jhingran, M. Salehpour, M. Sam, L. Levy, and P. J. Eifel, "Vaginal motion and bladder and rectal volumes during pelvic intensity-modulated radiation therapy after hysterectomy," *International Journal of Radiation Oncology* Biology* Physics*, vol. 82, no. 1, pp. 256–262, 2012.

[70] M. van Herk, A. Bruce, A. G. Kroes, T. Shouman, A. Touw, and J. V. Lebesque, "Quantification of organ motion during conformal radiotherapy of the prostate by three dimensional image registration," *International Journal of Radiation Oncology* Biology* Physics*, vol. 33, no. 5, pp. 1311–1320, 1995.

[71] R. Jadon, C. Pembroke, C. Hanna, N. Palaniappan, M. Evans, A. Cleves, and J. Staffurth, "A systematic review of organ motion and image-guided strategies in external beam radiotherapy for cervical cancer," *Clinical Oncology*, vol. 26, no. 4, pp. 185–196, 2014.

[72] A. Akbarzadeh, D. Gutierrez, A. Baskin, M. R. Ay, A. Ahmadian, N. R. Alam, K.-O. Lövblad, and H. Zaidi, "Evaluation of whole-body MR to CT deformable image registration," *Journal of Applied Clinical Medical Physics*, vol. 14, no. 4, pp. 238–253, 2013.

Appendices

Appendix A IRB Documentation

EAST CAROLINA UNIVERSITY
University & Medical Center Institutional Review Board Office
1L-09 Brody Medical Sciences Building· Mail Stop 682
600 Moye Boulevard · Greenville, NC 27834
Office **252-744-2914** · Fax **252-744-2284** · **www.ecu.edu/irb**

Notification of Exempt Certification

From: Biomedical IRB
To: Zhibin Huang
CC:

Date: 3/5/2012
Re: UMCIRB 12-000410
Cervical Cancer: Predictive Assay by MR Imaging #CA7 1906-06

I am pleased to inform you that your research submission has been certified as exempt on 3/3/2012. This study is eligible for Exempt Certification under category #4.

It is your responsibility to ensure that this research is conducted in the manner reported in your application and/or protocol, as well as being consistent with the ethical principles of the Belmont Report and your profession.

This research study does not require any additional interaction with the UMCIRB unless there are proposed changes to this study. Any change, prior to implementing that change, must be submitted to the UMCIRB for review and approval. The UMCIRB will determine if the change impacts the eligibility of the research for exempt status. If more substantive review is required, you will be notified within five business days.

The UMCIRB office will hold your exemption application for a period of five years from the date of this letter. If you wish to continue this protocol beyond this period, you will need to submit an Exemption Certification request at least 30 days before the end of the five year period.

The Chairperson (or designee) does not have a potential for conflict of interest on this study.

IRB00000705 East Carolina U IRB #1 (Biomedical) IORG0000418
IRB00003781 East Carolina U IRB #2 (Behavioral/SS) IORG0000418 IRB00004973
East Carolina U IRB #4 (Behavioral/SS Summer) IORG0000418

East Carolina University

Hello, **Samuel Leu**

Dashboard | Home | IRB Studies | Issues

Back to Change Log | Previous | Next

Number of modification(s) on this page: 1

Number of modified page(s): 2

Currently Approved: UMCIRB 12-000410		Proposed Modifications	
Study Identification Information		**Study Identification Information**	
This is the first step in your Human Research Application. You will automatically be guided to the appropriate page views needed to complete your submission. If a question is not applicable to your study, you may state this as your response. Please read the help text located on the right side of the page throughout this application.		This is the first step in your Human Research Application. You will automatically be guided to the appropriate page views needed to complete your submission. If a question is not applicable to your study, you may state this as your response. Please read the help text located on the right side of the page throughout this application.	
1.0 * **Study Name (Short):** Cervical Cancer: Predictive Assay by MR Imaging #CA7 1906-06	The short study name is limited to 255 characters.	1.0 * **Study Name (Short):** Cervical Cancer: Predictive Assay by MR Imaging #CA7 1906-06	The short study name is limited to 255 characters.
2.0 **Study Name (Long):**	Most other text boxes do not have any limits on number of characters.	2.0 **Study Name (Long):**	Most other text boxes do not have any limits on number of characters.
3.0 * **Summary of Research in Lay Terms:** This NIH funded study was a transfer from the University of Iowa and the University of Oklahoma to Ohio State University. All PHI of the subjects had already been accrued at the 2 outside institutions. The PI and team are complete the remaining analysis of the data at OSU and no patients will be accrued. The raw data and PHI had been anonymized with ID numbers. The purpose of the study is to identify imaging parameters in cervical cancer for the early prediction of therapy failure. The preliminary data suggested prediction of failure can be achieved as early as 2 weeks into the 8 week treatment cycle.	The lay summary should be no more than 400 words and should include the following: Background/Purpose of Study Description of Subjects/Participants Research Methods/Procedures	3.0 * **Summary of Research in Lay Terms:** This NIH funded study was a transfer from the University of Iowa and the University of Oklahoma to Ohio State University. All PHI of the subjects had already been accrued at the 2 outside institutions. The PI and team are complete the remaining analysis of the data at OSU and no patients will be accrued. The raw data and PHI had been anonymized with ID numbers. The purpose of the study is to identify imaging parameters in cervical cancer for the early prediction of therapy failure. The preliminary data suggested prediction of failure can be achieved as early as 2 weeks into the 8 week treatment cycle.	The lay summary should be no more than 400 words and should include the following: Background/Purpose of Study Description of Subjects/Participants Research Methods/Procedures
4.0 * **Principal Investigator:** Zhibin Huang	Use the "select" or "add" button to choose from a list of individuals for each applicable role.	4.0 * **Principal Investigator:** Zhibin Huang	Use the "select" or "add" button to choose from a list of individuals for each applicable role.
5.0 **Faculty Investigator** (Serving as the responsible individual in the oversight of the research study when the PI is a student, resident, fellow or visiting faculty.) Faculty Investigator IRB Certification Renewal Deadline:		5.0 **Faculty Investigator** (Serving as the responsible individual in the oversight of the research study when the PI is a student, resident, fellow or visiting faculty.) Faculty Investigator IRB Certification Renewal Deadline:	
6.0 **Study Coordinator or Contact Individual:**		6.0 **Study Coordinator or Contact Individual:**	
7.0 **Contact Individual(s) (if different from Study Coordinator or Principal Investigator):**	People added here will be able to edit the study. Clicking the "Add" button allows you to choose individuals that are already registered within ePIRATE. This function will not add individuals that have not registered in ePIRATE yet.	7.0 **Contact Individual(s) (if different from Study Coordinator or Principal Investigator):**	People added here will be able to edit the study. Clicking the "Add" button allows you to choose individuals that are already registered within ePIRATE. This function will not add individuals that have not registered in ePIRATE yet.
Last Name / First Name / Organization / Profile / IRB Certification Renewal Deadline		Last Name / First Name / Organization / Profile / IRB Certification Renewal Deadline	
There are no items to display		There are no items to display	
8.0 **Sub-Investigators:**		8.0 **Sub-Investigators:**	
Last Name / First Name / Organization / Profile / IRB Certification Renewal Deadline		Last Name / First Name / Organization / Profile / IRB Certification Renewal Deadline	
9.0	Other study staff may include	9.0 **Other Study Staff - (Read-Only):**	Other study staff may include graduate assistants, statisticians or others that may only have a very limited

Other Study Staff - (Read-Only):

Last Name	First Name	Organization	Profile	IRB Certification Renewal Deadline

There are no items to display

graduate assistants, statisticians or others that may only have a very limited and specific role in the study. People added here will be able to read the study.

Last Name	First Name	Organization	Profile	IRB Certification Renewal Deadline
Leu	Samuel	Physics, Department of	Samuel Leu's Profile	
Stuart	Brian	Radiation Oncology, Department of	Brian Stuart's Profile	7/5/2019
Winkler	Stephanie	Physics, Department of	Stephanie Winkler's Profile	

and specific role in the study. People added here will be able to read the study.

Appendix B Sequences of MR_1, MR_2, rCT, and pCT Axial Images

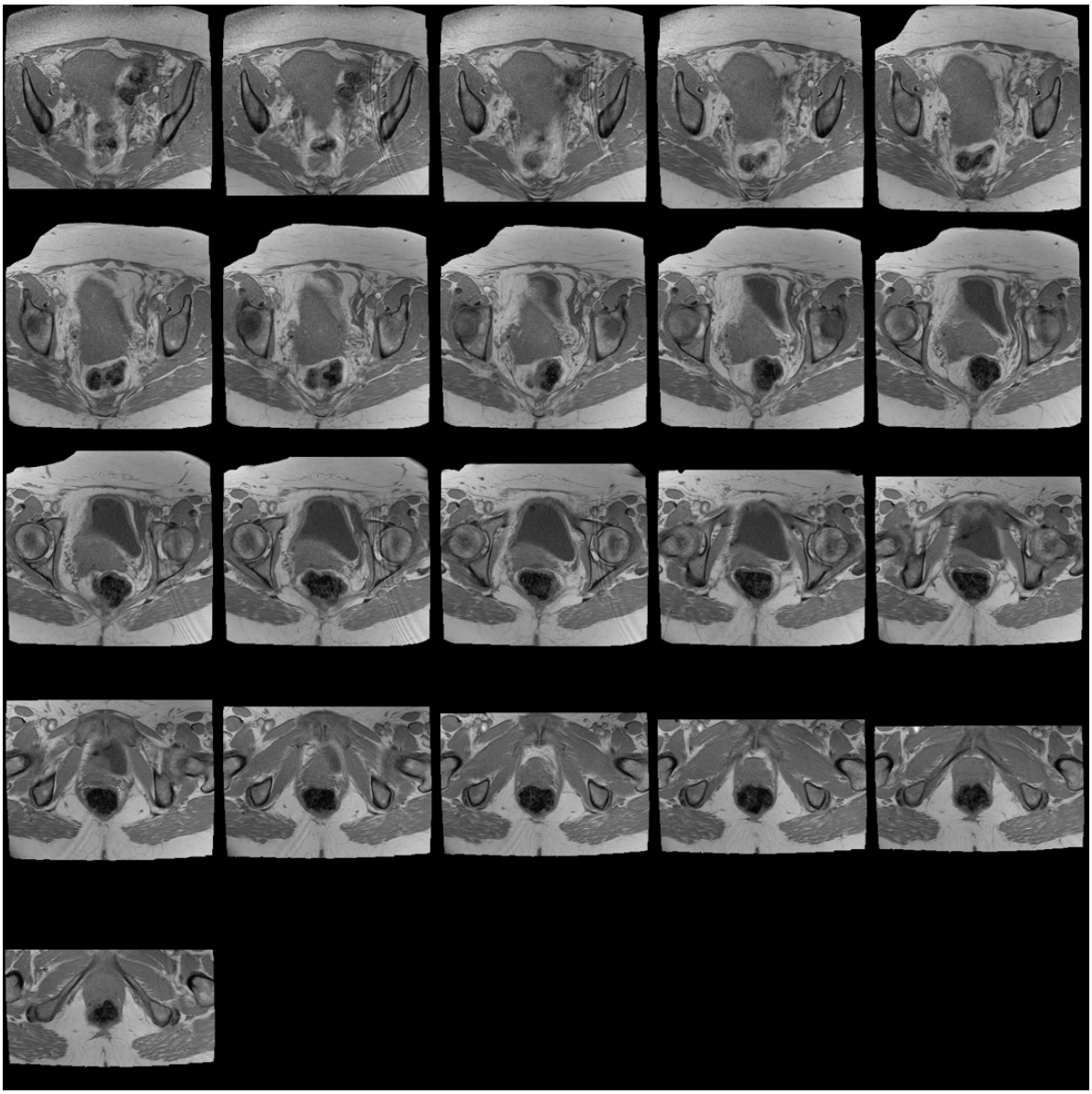

Figure 23: A sequence of MR_1 axial slice images for Cycle2.

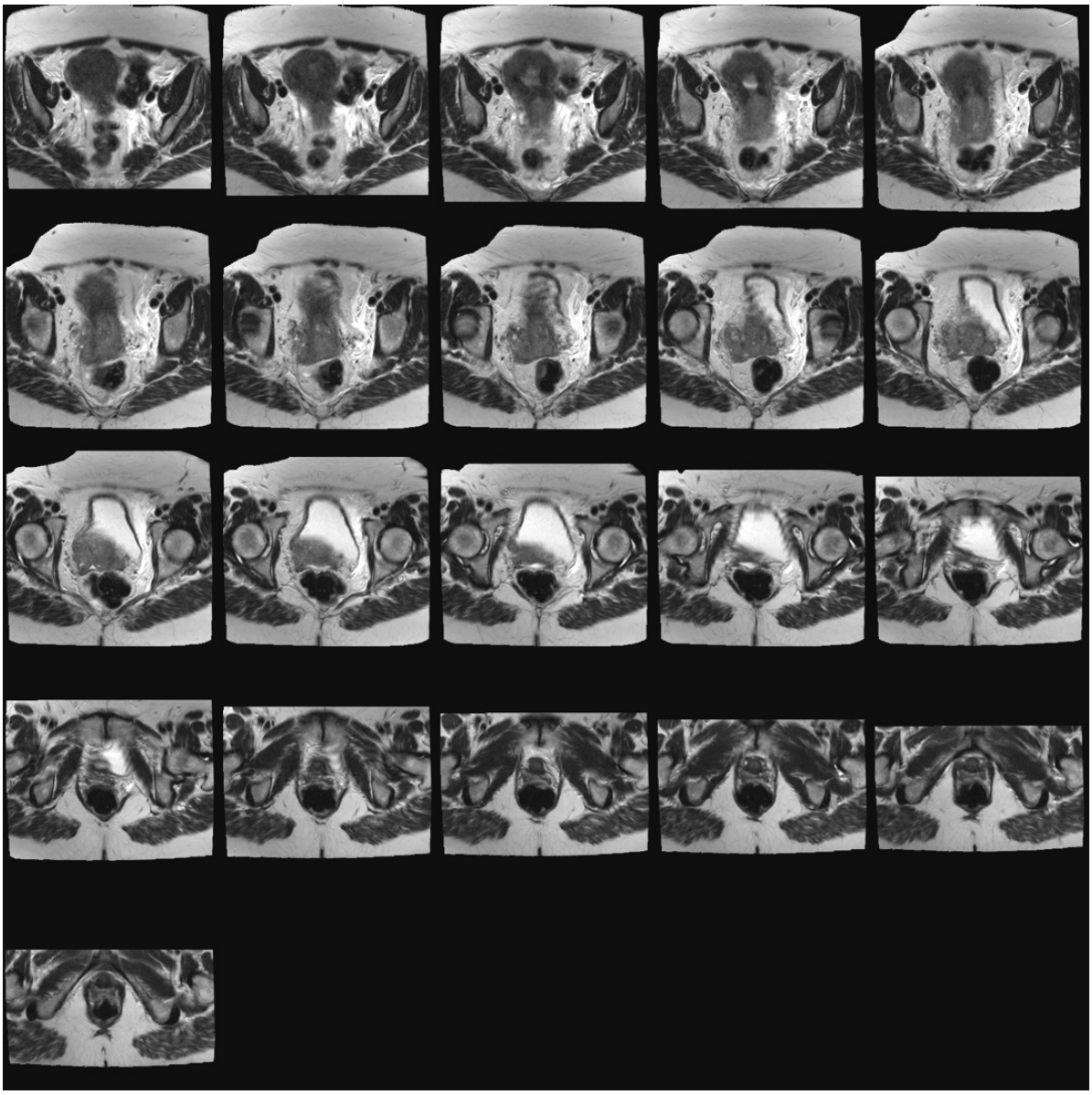

Figure 24: A sequence of MR_2 axial slice images for Cycle2.

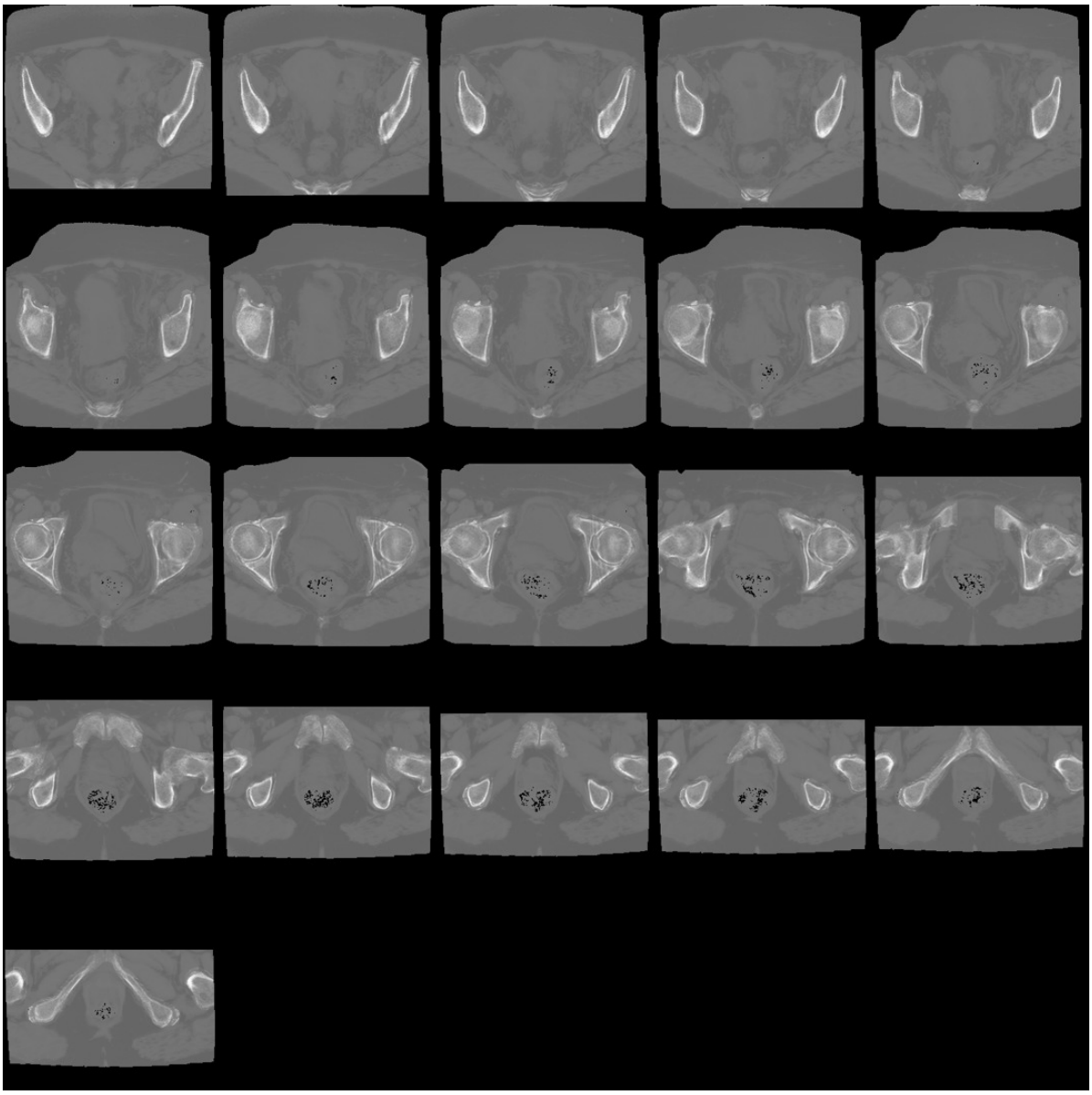

Figure 25: A sequence of pCT axial slice images for Cycle2.

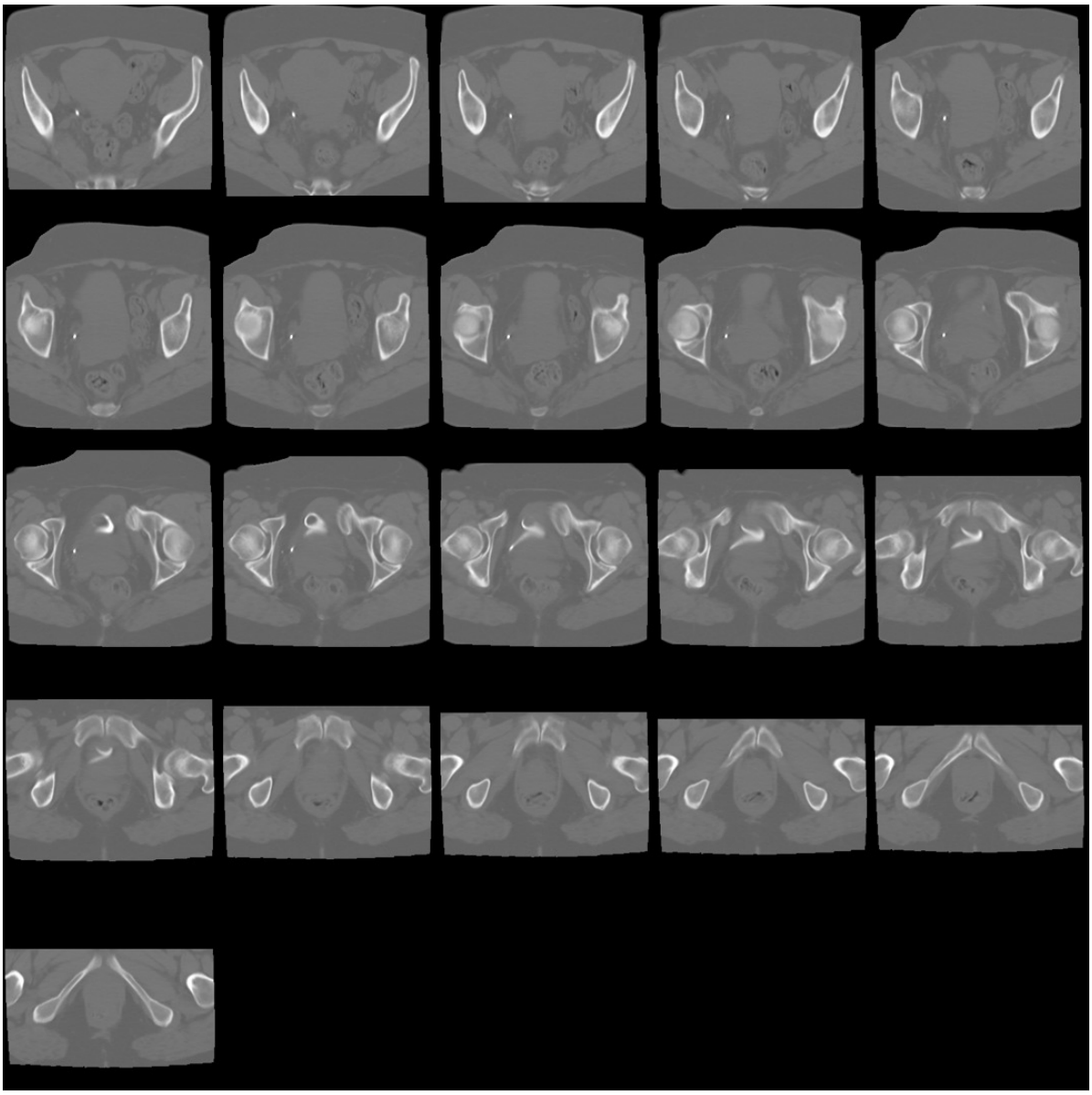

Figure 26: A sequence of rCT axial slice images for Cycle2.

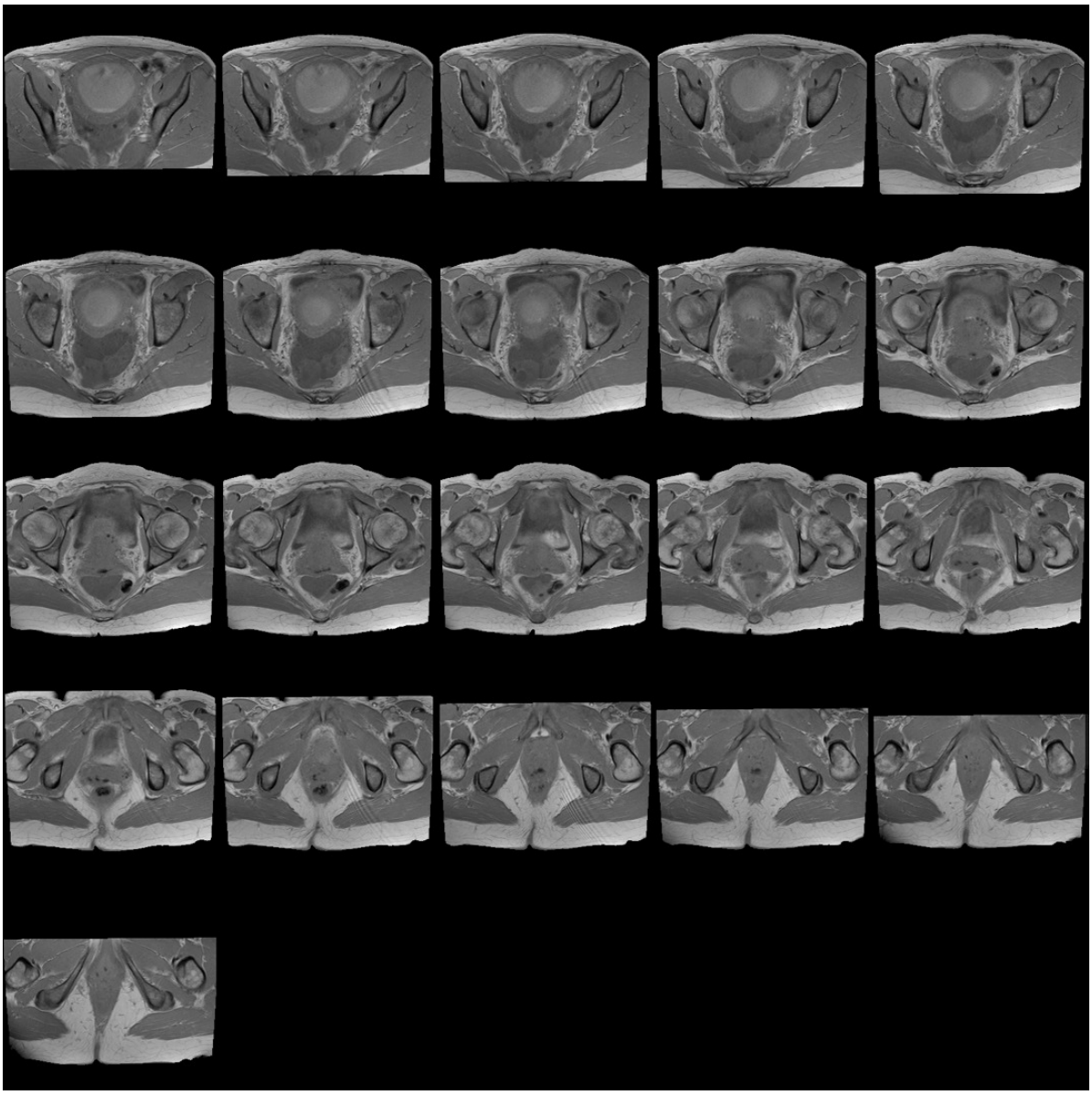

Figure 27: A sequence of MR_1 axial slice images for Cycle3.

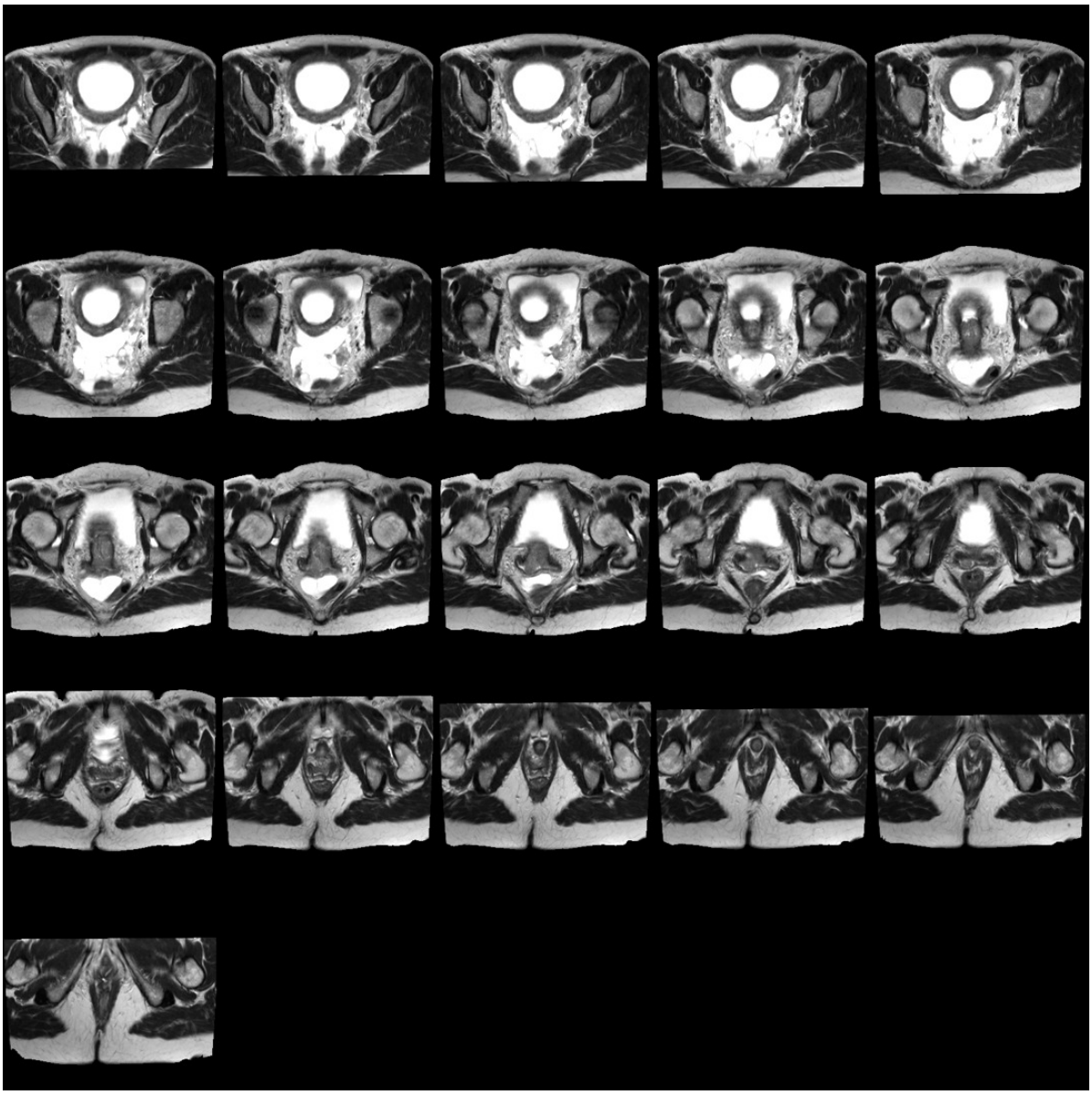

Figure 28: A sequence of MR_2 axial slice images for Cycle3.

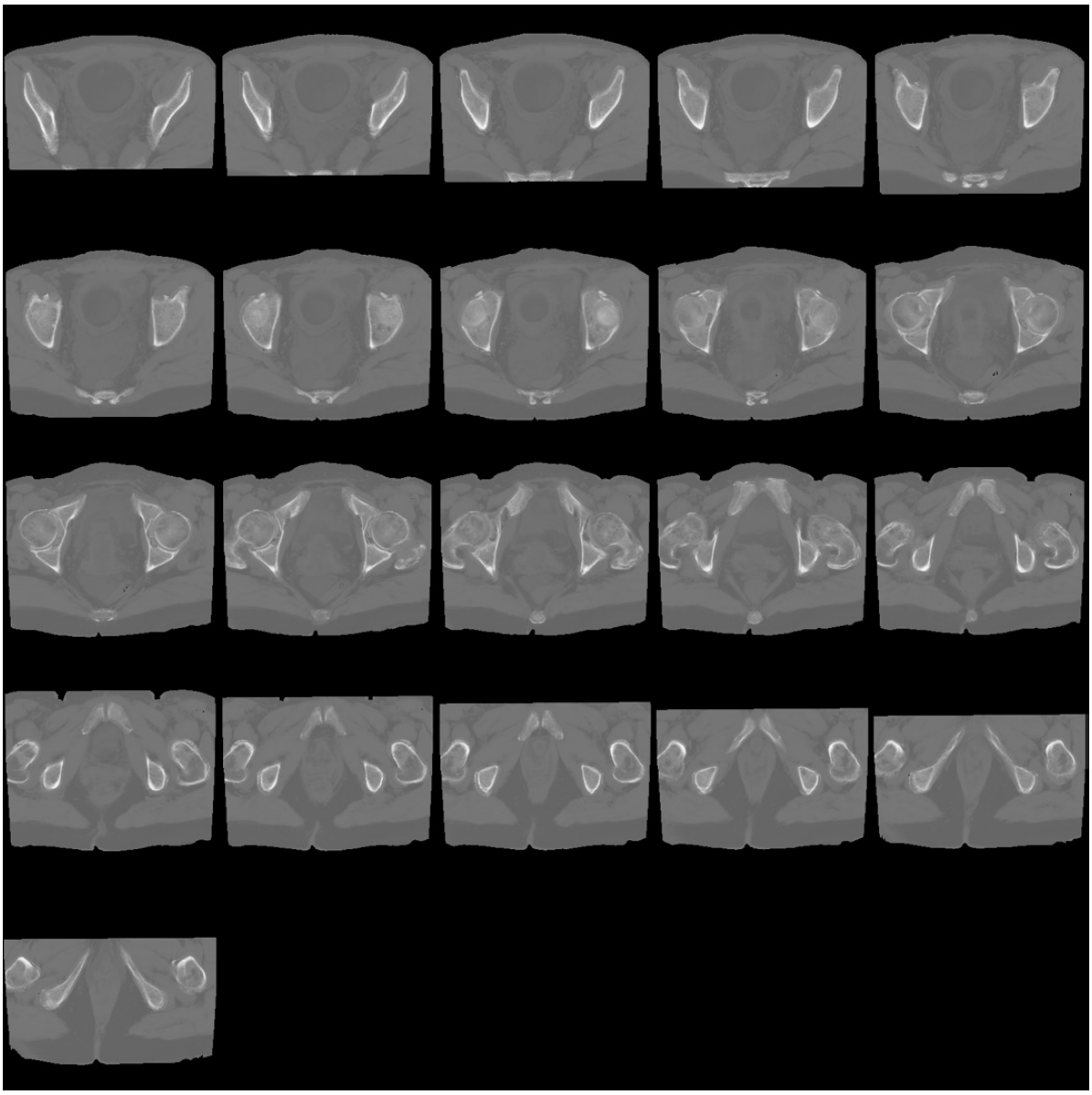

Figure 29: A sequence of pCT axial slice images for Cycle3.

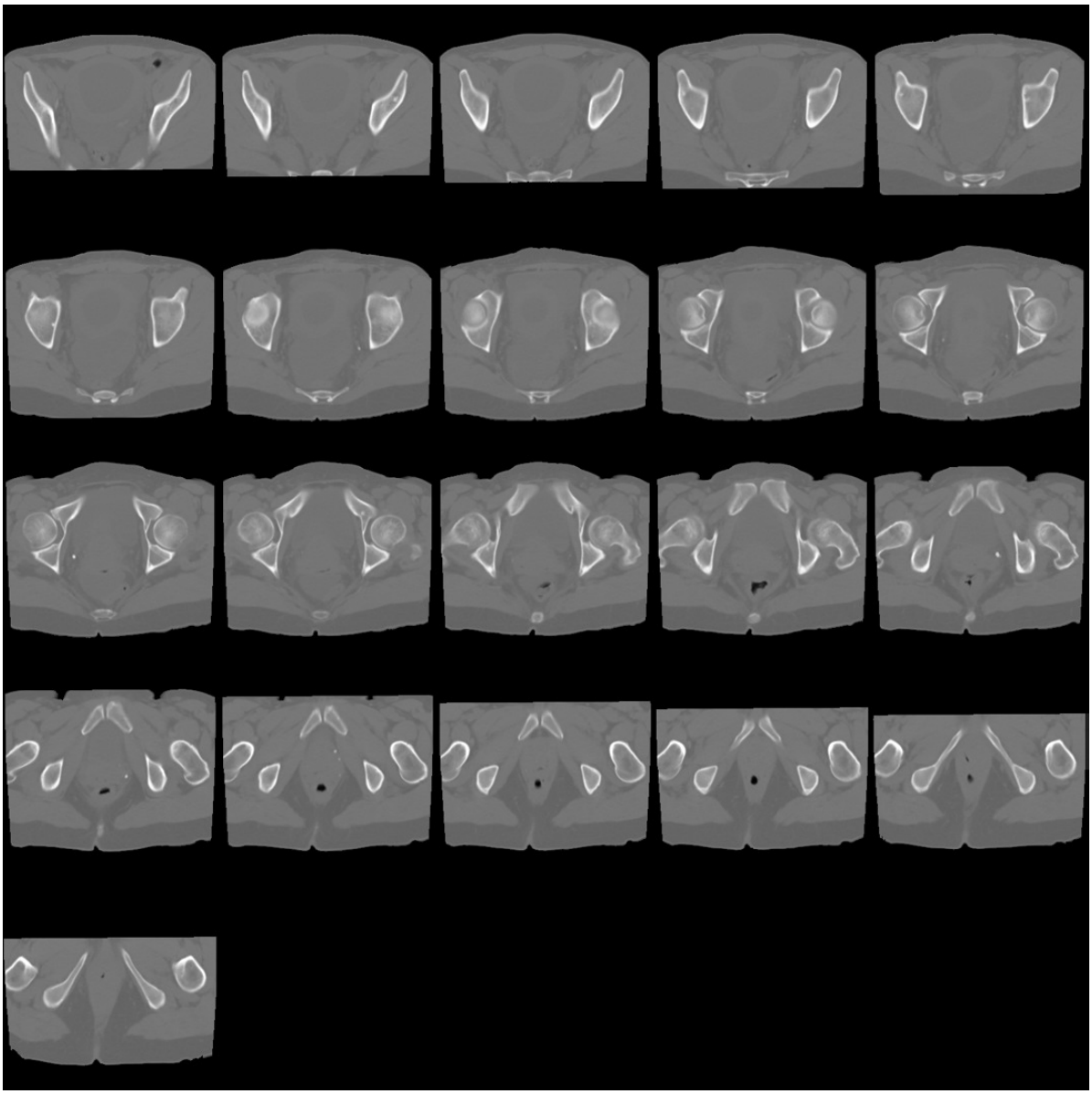

Figure 30: A sequence of rCT axial slice images for Cycle3.

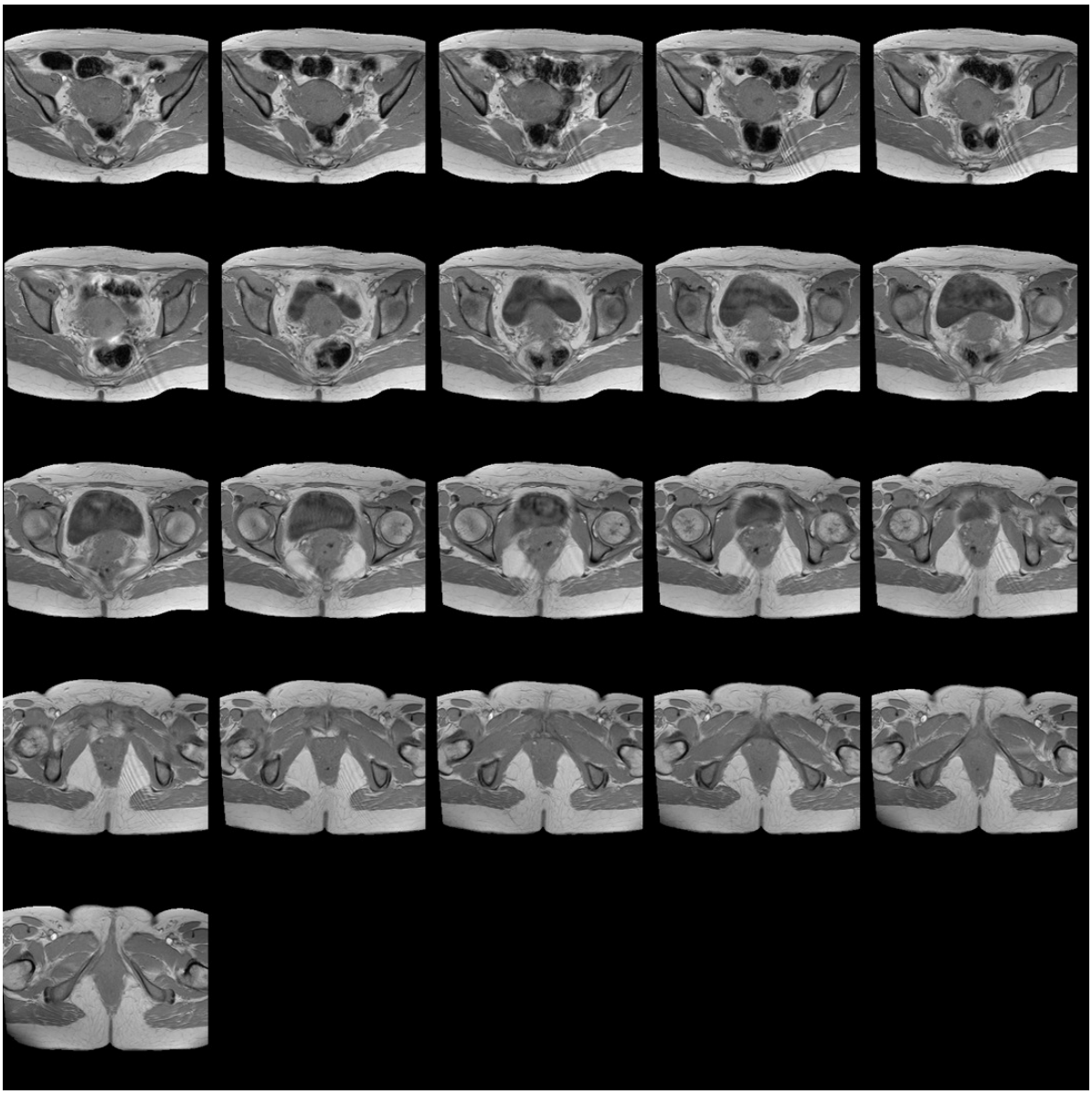

Figure 31: A sequence of MR_1 axial slice images for Cycle4.

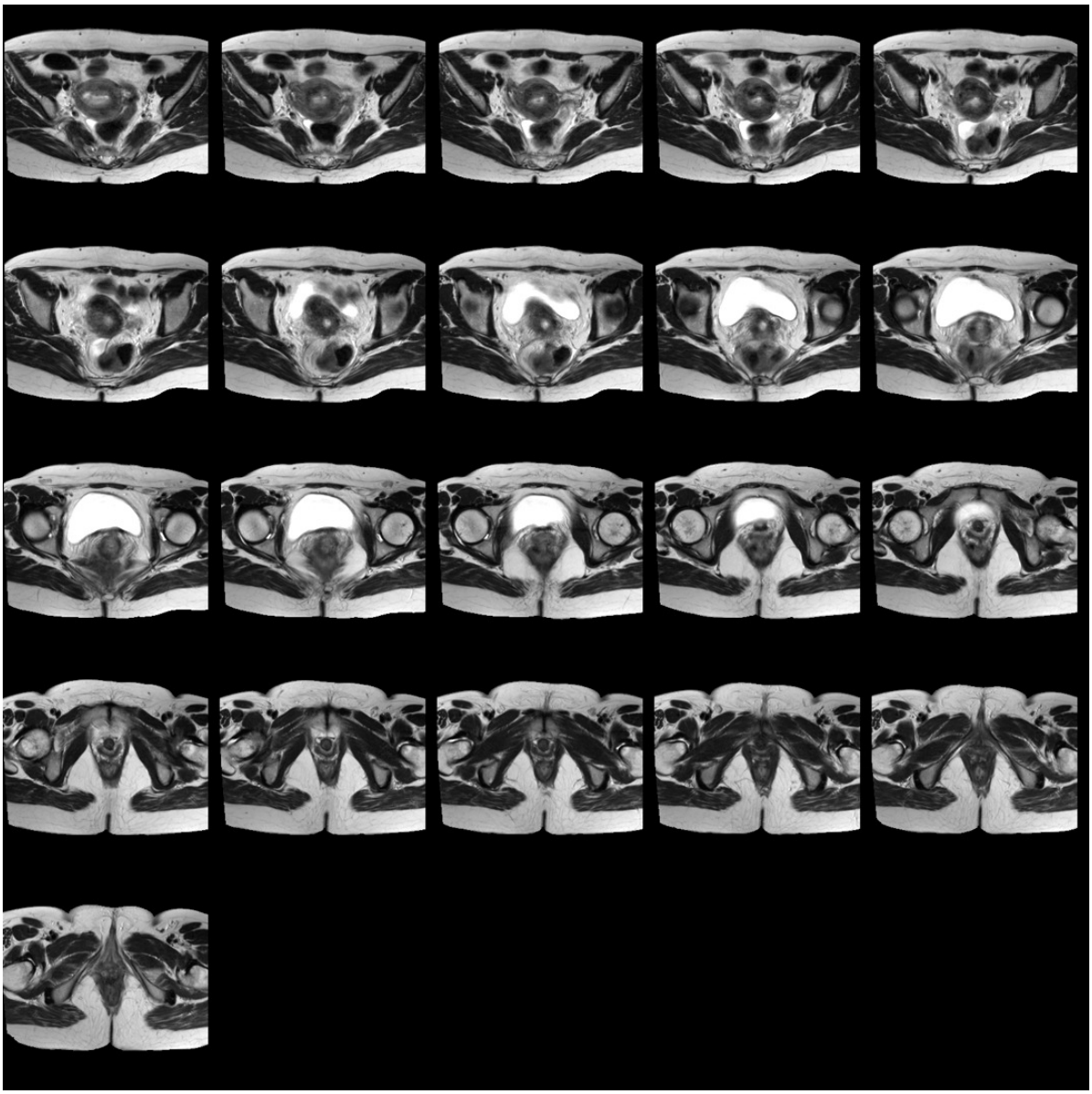

Figure 32: A sequence of MR_2 axial slice images for Cycle4.

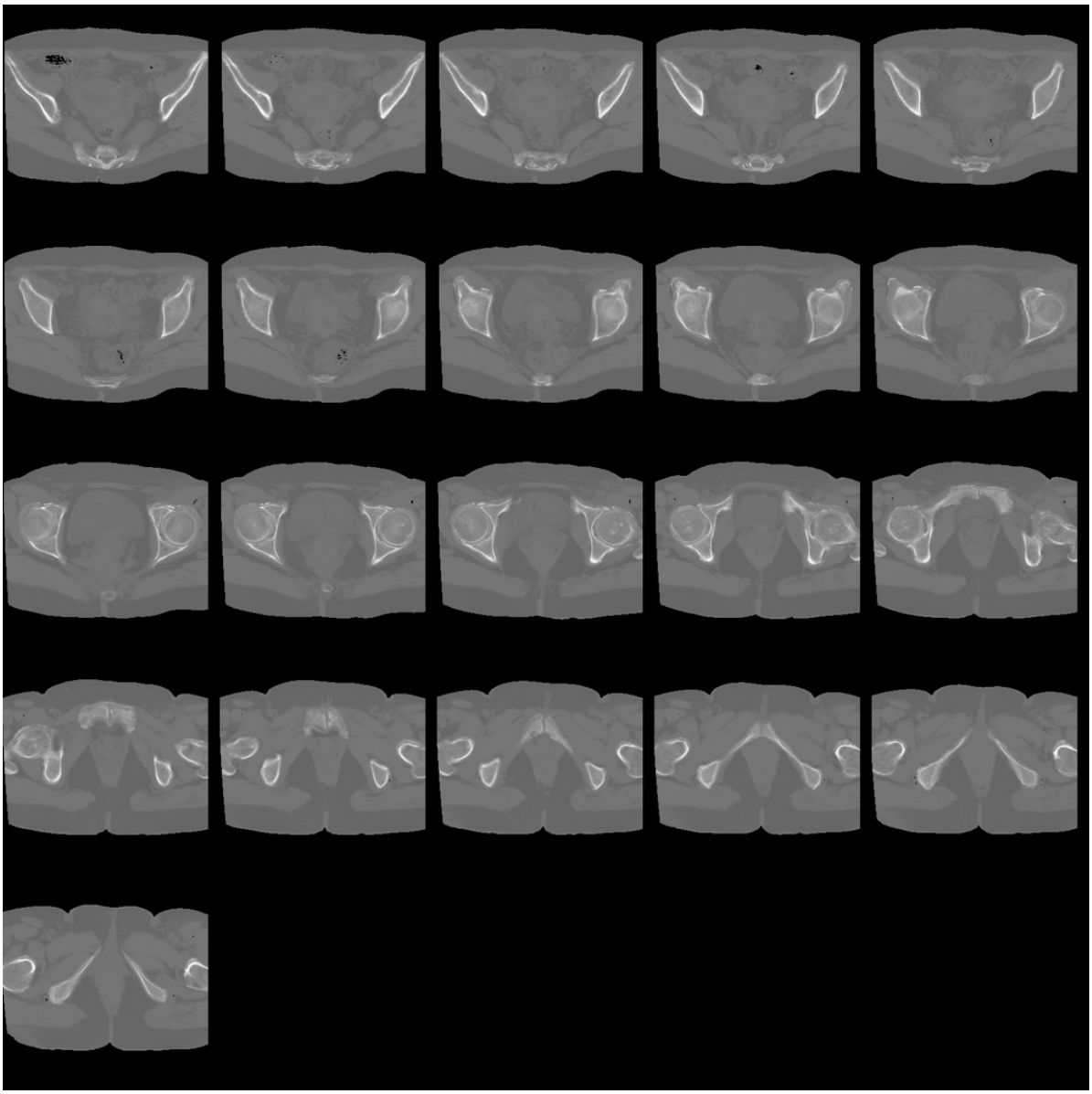

Figure 33: A sequence of pCT axial slice images for Cycle4.

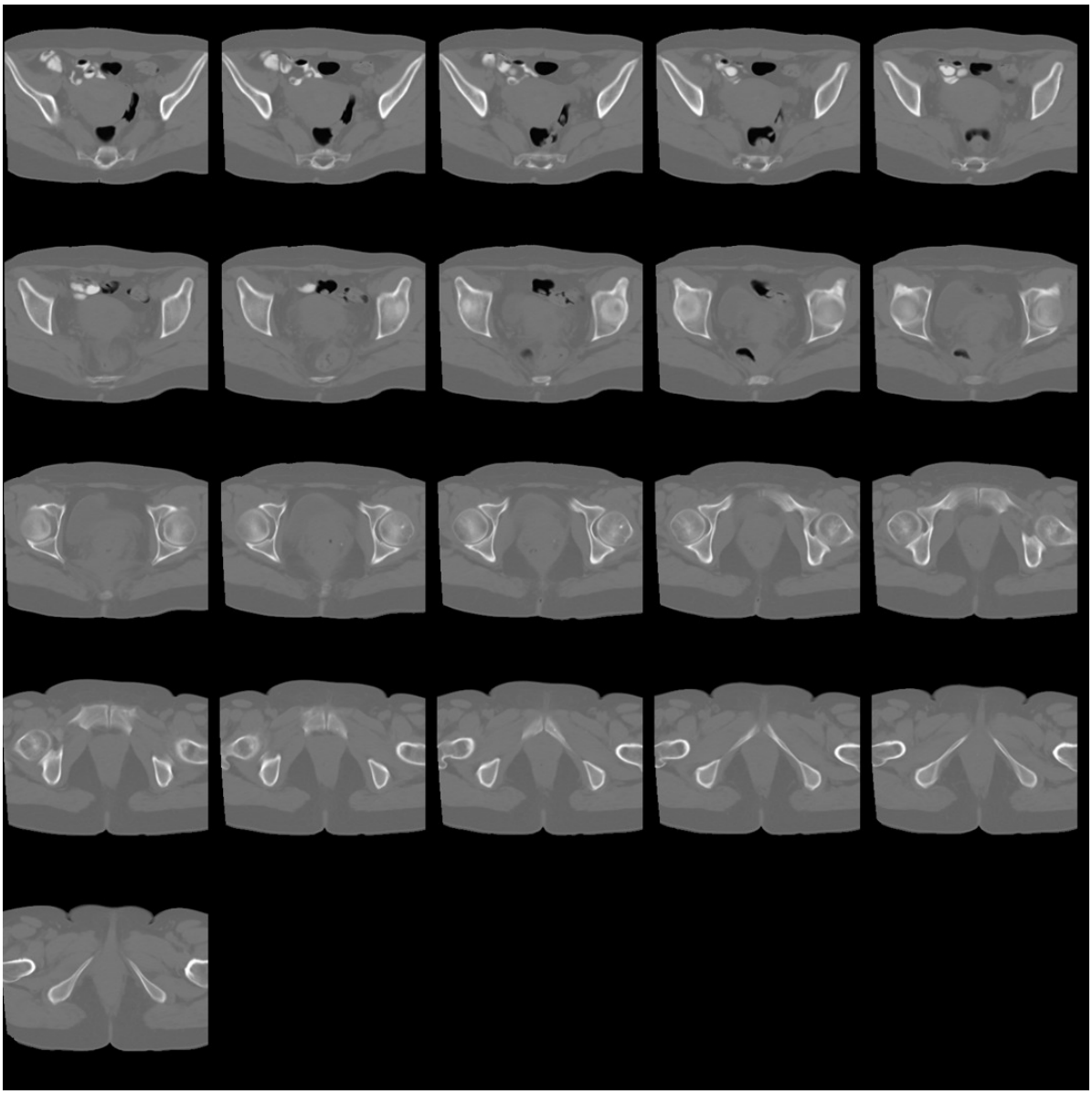

Figure 34: A sequence of rCT axial slice images for Cycle4.

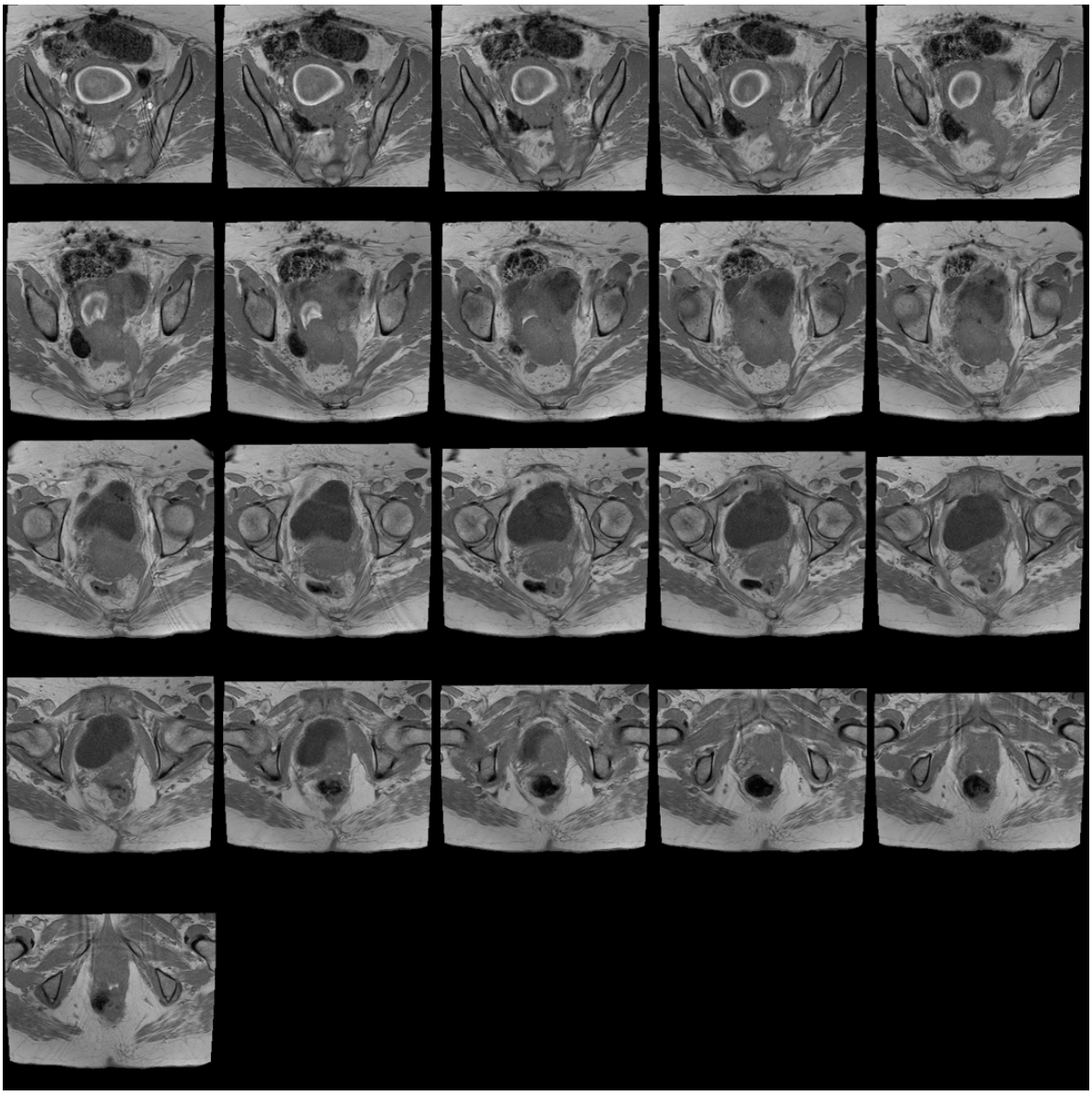

Figure 35: A sequence of MR_1 axial slice images for Cycle5.

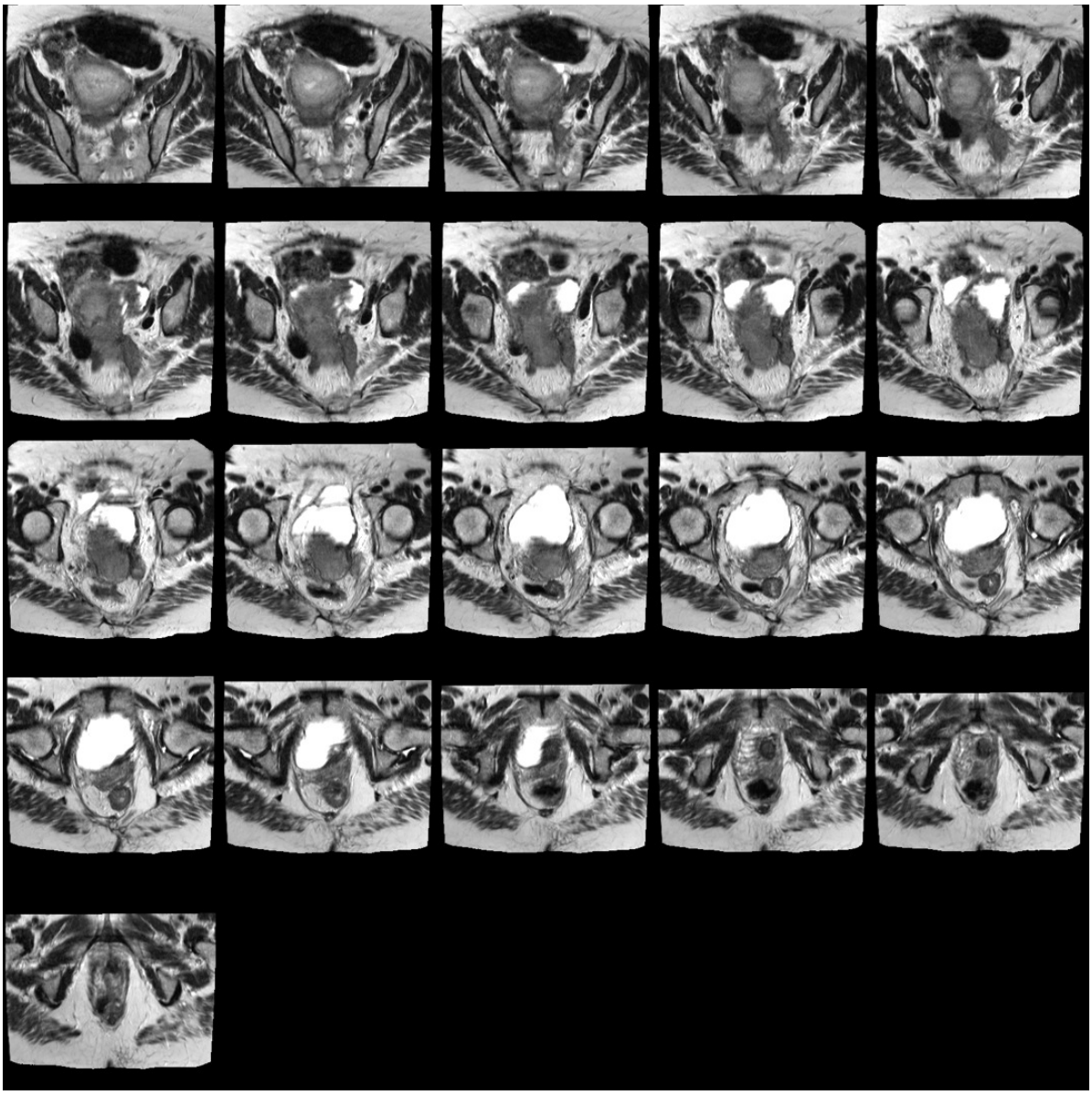

Figure 36: A sequence of MR_2 axial slice images for Cycle5.

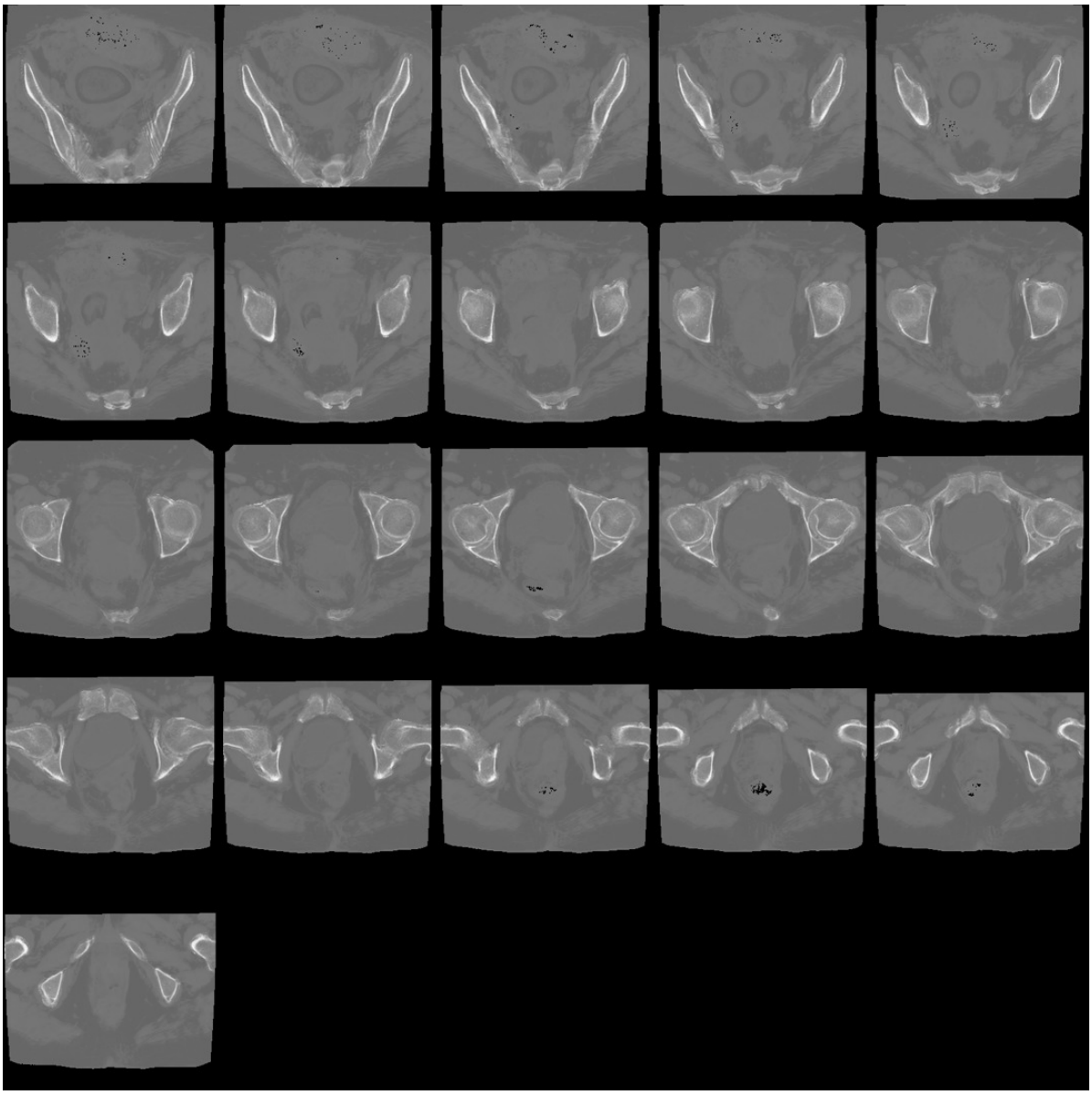

Figure 37: A sequence of pCT axial slice images for Cycle5.

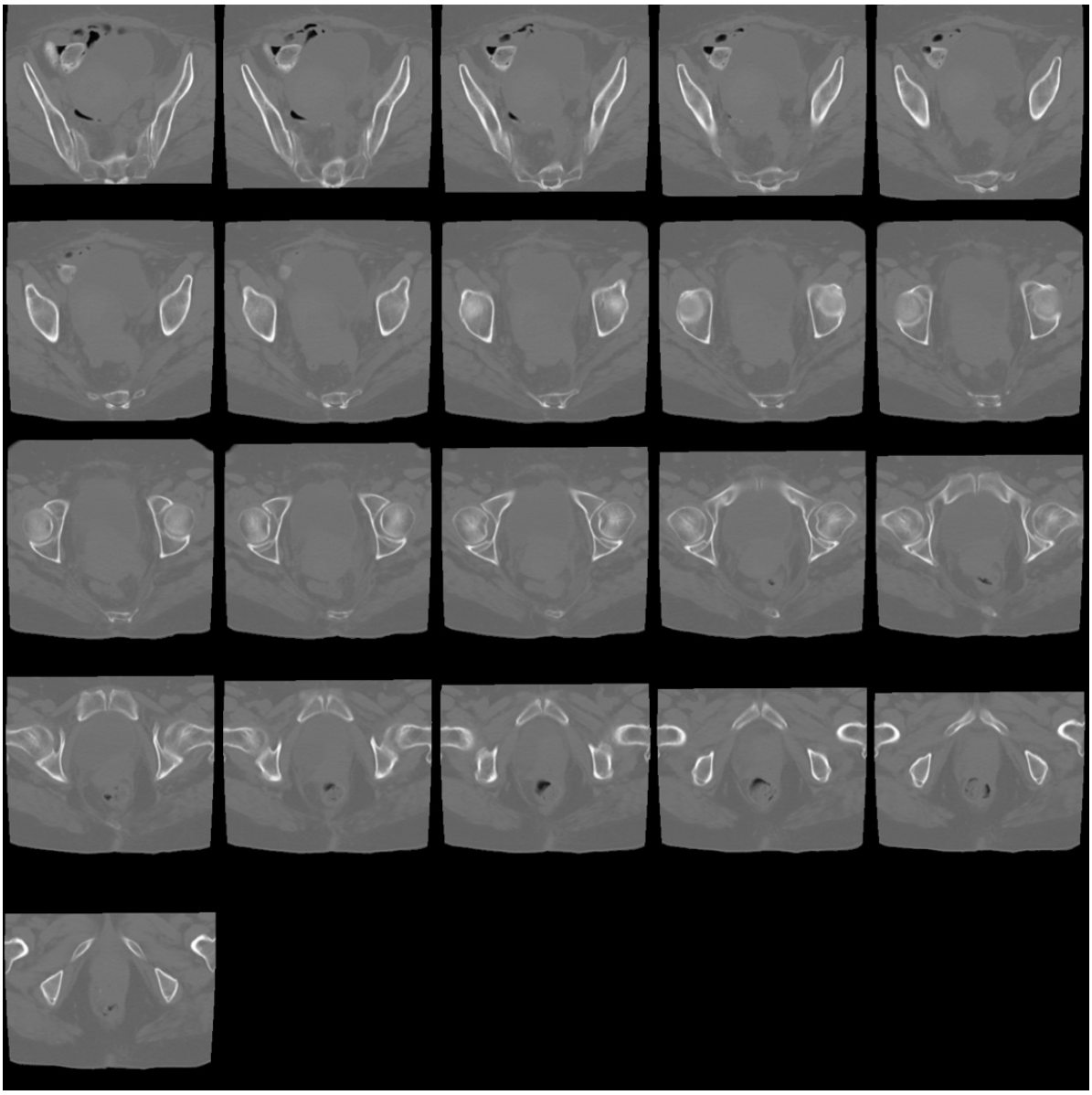

Figure 38: A sequence of rCT axial slice images for Cycle5.

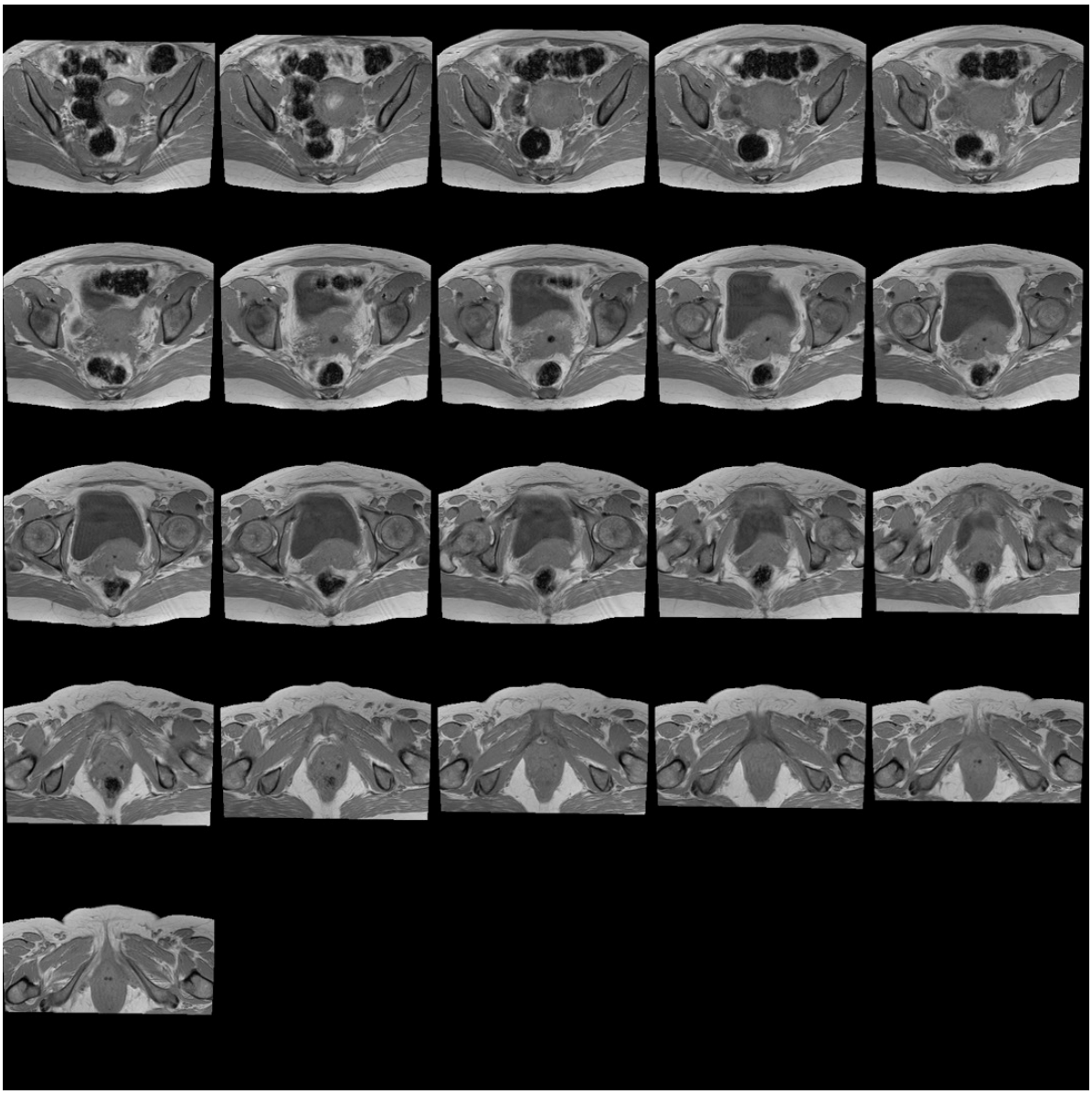

Figure 39: A sequence of MR_1 axial slice images for Cycle6.

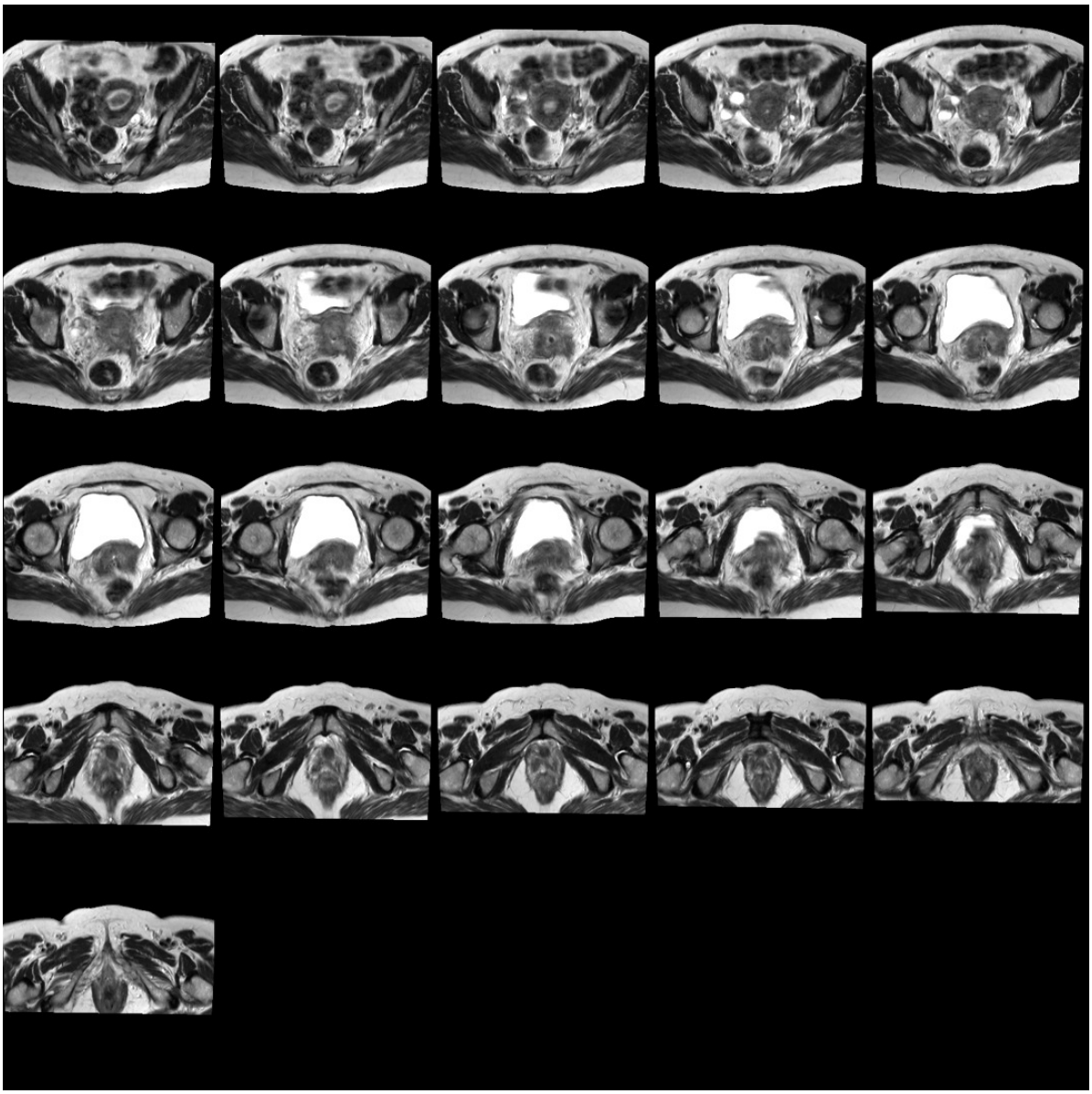

Figure 40: A sequence of MR_2 axial slice images for Cycle6.

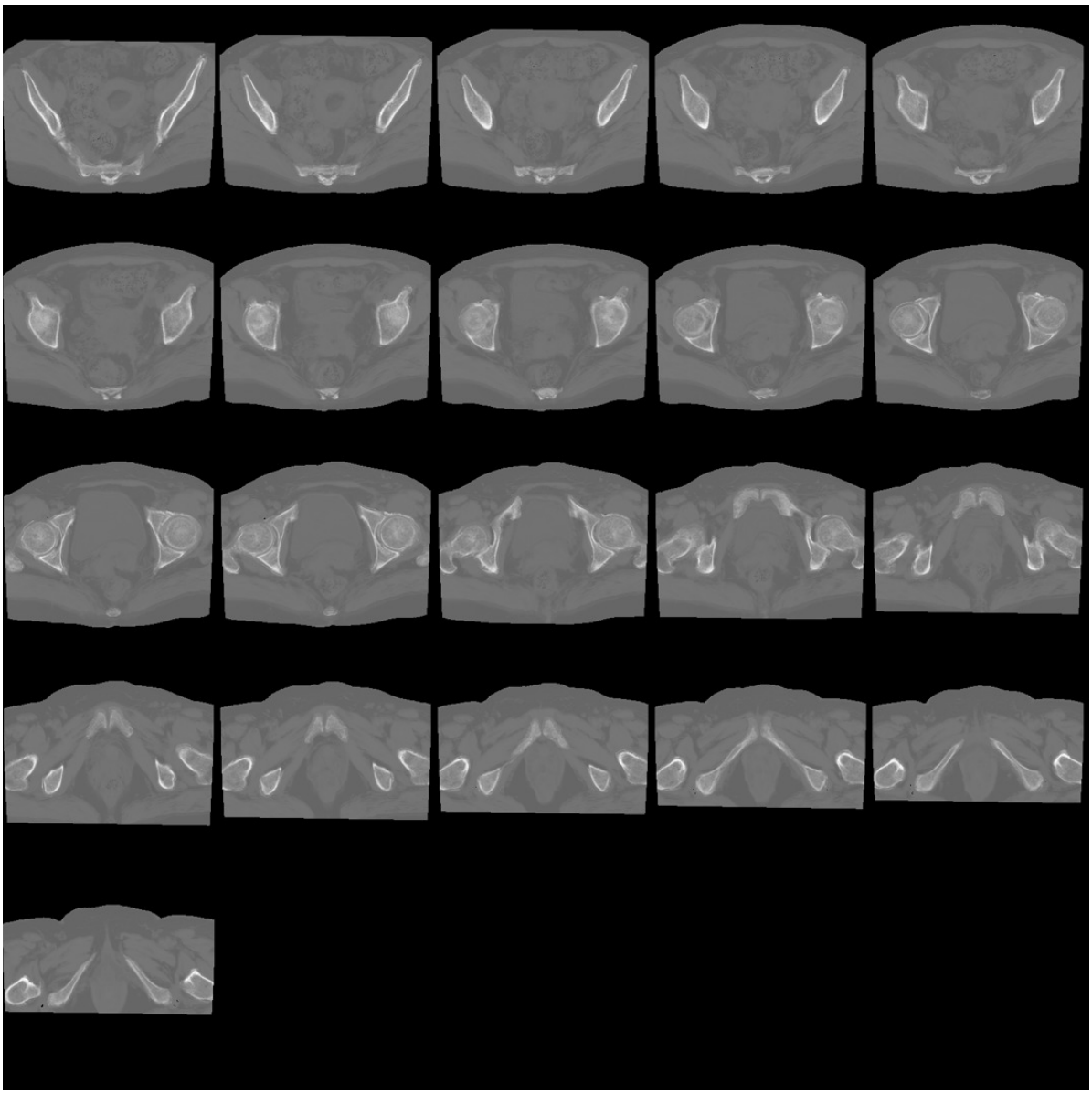

Figure 41: A sequence of pCT axial slice images for Cycle6.

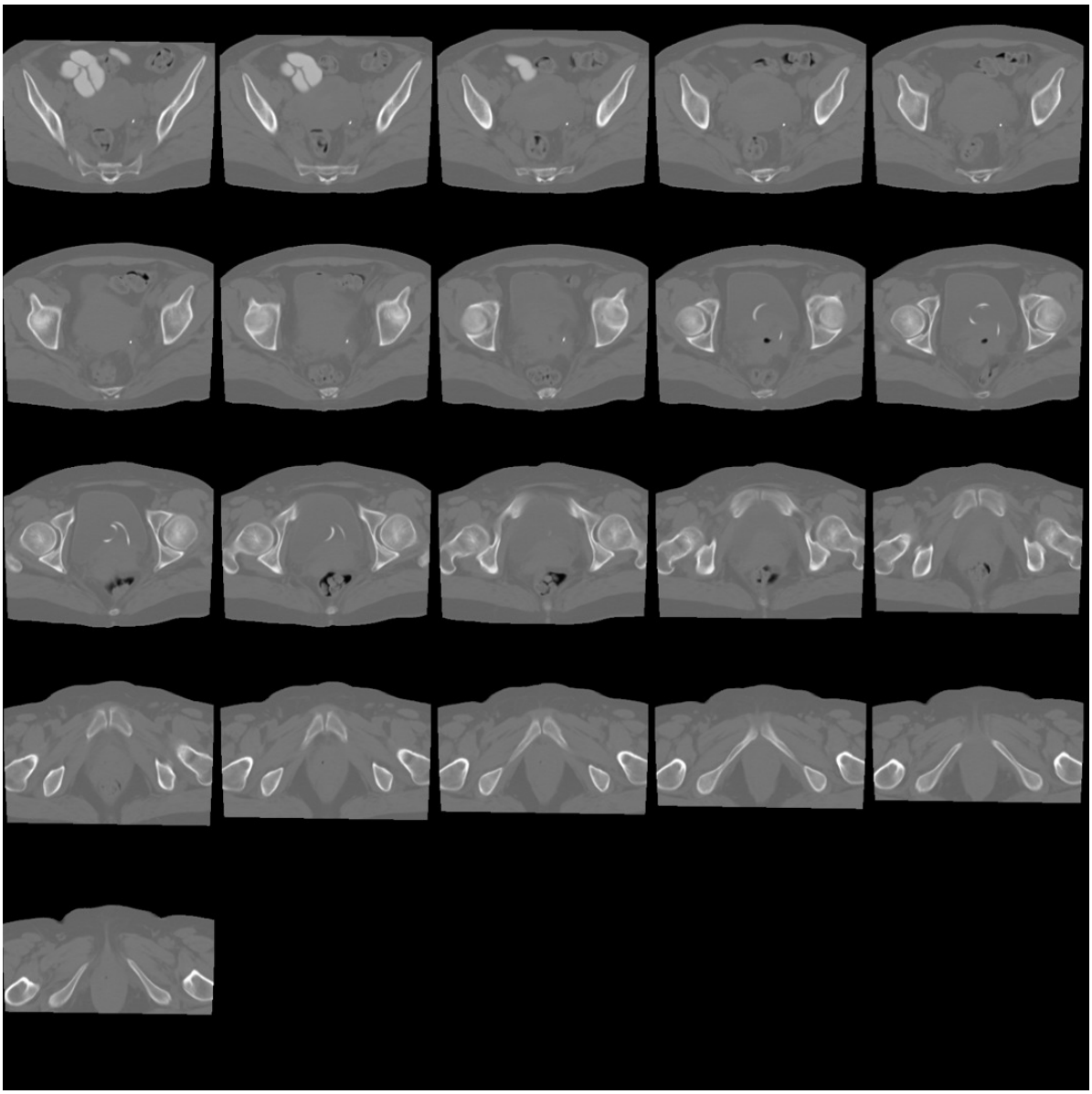

Figure 42: A sequence of rCT axial slice images for Cycle6.

Appendix C Mathematica Code

Creates the polynomial function, specify the independent variables, and set the coefficient of polynomial function as the unknown variable.

```
polyform30 =
  Sum[ToExpression[StringJoin["c", ToString[i], "c", ToString[j]]] *
    x^i * y^j, {i, 0, 30}, {j, 0, 30 - i}];

polyConst30 =
  ToExpression[Table[StringJoin["c", ToString[i], "c", ToString[j]],
     {i, 0, 30}, {j, 0, 30 - i}] // Flatten];

polyConstList30 =
  ToExpression[Table[StringJoin["c", ToString[i], "c", ToString[j]],
    {i, 0, 30}, {j, 0, 30 - i}]];
```

Import MR1, MR2, CT, and count data for the specified region.

```
mr1SoftdataCycle1bn200 =
  Import["mr1SoftdataCycle1bn200"] // Flatten;

mr2SoftdataCycle1bn200 =
  Import["mr2SoftdataCycle1bn200"] // Flatten;

ctSoftdataCycle1bn200 = Import["ctSoftdataCycle1bn200"] // Flatten;

countSoftdataCycle1bn200 =
  Import["countSoftdataCycle1bn200"] // Flatten;

dataSoftCycle1bn200 =
  Transpose[ {(mr1SoftdataCycle1bn200 - 0.5 / 200),
    (mr2SoftdataCycle1bn200 - 0.5 / 200), ctSoftdataCycle1bn200}];
```

Solve for coefficients of polynomial function by using a NonlinearModelFit to fit to the data points given.

```
fitSoftdataCycle1bn200 =
  NonlinearModelFit[dataSoftCycle1bn200, {polyform30},
   polyConst30, {x, y}, Weights → countSoftdataCycle1bn200];
```

Appendix D Matlab Code


```
% Converting MRI MR1 MR2 to pCT With air filtering and pCT limits of 0-3100
%(this corresponds to HU value of -1000 to 2100)
function [pCT] = ...
    dataFitSMB(mriT1,mriT2,maskSMB,fitregion)

% f(x,y) = Sum(i,j,n)*Cij*x^i*y^j
% Coefficient Parameters from my Fit
% Fit parameteres from ixj matrix 'fit'
% Fit N x M x 1 => Soft / Fit N x M x 2 => Mixed / Fit N x M x 3 => Bone

% maskSMB(i,j,k,#)
% Contains mask for the three regions Soft, Mixed, and Bone
% mask 1 => Soft / mask 2 => Mixed / mask 3 => Bone

% Variable Declarations
binN=1;
xBinN=double(1420/binN);
yBinN=double(37100/binN);

matSize=size(mriT1);
tempCT=zeros(matSize(1),matSize(2),matSize(3));

%Redefine mr1 and mr2 values into nbin values.
tempT1=double(mriT1)./xBinN;
tempT2=double(mriT2)./yBinN;

rowEnd=matSize(1); colEnd=matSize(2); slEnd=matSize(3);

tempErrH = zeros(1,1); tempErrL = zeros(1,1);
l = 1; h = 1;

%Look through all voxels of image. First check the body contour and then
%determine which fit to use based on the segmentation mask.
for k=1:slEnd
    if sum(sum(maskSMB(:,:,k)))==0
        continue
    end
    for i = 1:rowEnd
        if sum(maskSMB(i,:,k))==0
            continue
        end
        for j = 1:colEnd
            if maskSMB(i,j,k)==0
                tempCT(i,j,k) = 0;
            else
                fitnum = maskSMB(i,j,k);
                if fitnum == 1
                    %Soft
                    tempMax = max(2);
                    tempMin = min(2);
                elseif fitnum == 2
                    %Mixed
                    tempMax = max(3);
                    tempMin = min(3);
                elseif fitnum == 3
                    %Bone
                    tempMax = max(4);
                    tempMin = min(4);
```

```
                end

                fit = fitregion(:,:,fitnum);
                %Estimate pCT value using coefficients from 'fit'
                fitlengthn = sqrt(numel(fit))-1;
                fitlengthm = sqrt(numel(fit))-1;

                temp=0;
                for n=0:fitlengthn
                    for m=0:fitlengthm
                        if fit((n+1),(m+1)) == 0
                            break
                        else
temp = fit((n+1),(m+1))*(tempT1(i,j,k))^(n)*(tempT2(i,j,k))^(m) + temp;
                        end
                    end
                end

                tempMax = 3000;
                tempMin = 0;
%Estimated pCT check. Since polynomial function is continuous from
%-Infinity to +Infinity a limit is placed so CT value is between the
%reference dataset average max and min of region.
                if temp > tempMax
                    tempErrH(1,h) = temp;
                    h = h+1;
text = ['pCT is greater than ',num2str(tempMax),' in region ', num2str(fitnum),...
                        ', value predicted is ', num2str(temp) ,'.'];
                    temp = tempMax;
                    disp(text)
                elseif temp < tempMin
                    tempErrL(1,l) = temp;
                    l = l+1;
text = ['pCT is less than ',num2str(tempMin),' in region ', num2str(fitnum),...
                        ', value predicted is ', num2str(temp) ,'.'];
                    temp = tempMin;
                    disp(text)
                end

% Determine whether if pixel(i,j,k) is an air pixel, assign air with pixel
% intensity of 0 uses normalizaed mr1 mr2 pixel value as long as its not
% within the Bone-region.
                if (maskSMB(i,j,k)==1)
                    if (mriT1(i,j,k)<90) && (mriT2(i,j,k)<700)
                        temp = 0;
                    end
                end
                tempCT(i,j,k) = temp;
            end
        end
    end
end

%Output final estimated pCT of all voxels
pCT=uint16(ceil(tempCT));

end
```